Advances in Civil Engineering

Advances in Seismic Resilience of Buildings

Lead Guest Editor: Edén Bojórquez
Guest Editors: Jorge Ruiz-García, Antonio Formisano, and Francisco López Almansa

Advances in Seismic Resilience of Buildings

Advances in Seismic Resilience of Buildings

Lead Guest Editor: Edén Bojórquez
Guest Editors: Jorge Ruiz-García, Antonio Formisano, and Francisco López Almansa

Contents

Hindawi
Advances in Civil Engineering
Volume 2019, Article ID 6480384, 19 pages
https://doi.org/10.1155/2019/6480384

Research Article

Seismic Control of Tall Buildings Using Distributed Multiple Tuned Mass Dampers

Hamid Radmard Rahmani and Carsten Könke

Institute of Structural Mechanics, Bauhaus-Universität Weimar, Marienstr. 15, D-99423 Weimar, Germany

Correspondence should be addressed to Hamid Radmard Rahmani; radmard.rahmani@gmail.com

Received 5 March 2019; Revised 16 July 2019; Accepted 29 July 2019; Published 19 September 2019

Guest Editor: Edén Bojórquez

The vibration control of tall buildings during earthquake excitations is a challenging task because of their complex seismic behavior. This paper investigates the optimum placement and properties of the tuned mass dampers (TMDs) in tall buildings, which are employed to control the vibrations during earthquakes. An algorithm was developed to spend a limited mass either in a single TMD or in multiple TMDs and distribute it optimally over the height of the building. The nondominated sorting genetic algorithm II (NSGA-II) method was improved by adding multivariant genetic operators and utilized to simultaneously study the optimum design parameters of the TMDs and the optimum placement. The results showed that, under earthquake excitations with noticeable amplitude in higher modes, distributing TMDs over the height of the building is more effective in mitigating the vibrations compared to the use of a single TMD system. From the optimization, it was observed that the locations of the TMDs were related to the stories corresponding to the maximum modal displacements in the lower modes and the stories corresponding to the maximum modal displacements in the modes which were highly activated by the earthquake excitations. It was also noted that the frequency content of the earthquake has significant influence on the optimum location of the TMDs.

1. Introduction

Given the modern development plans of large cities, which are designed to answer the needs of their fast-growing population, it is anticipated that the buildings in such cities will become taller and more expensive [1]. As result, the area of investigating solutions to provide safety and serviceability of tall buildings in case of natural hazards such as strong winds and earthquakes has gained much attention in the last decade.

The current seismic design codes allow the structures to undergo inelastic deformations during strong earthquakes. Such structures would experience larger deformations but less seismic forces; otherwise, the structure should sustain much larger earthquake loads.

On the contrary, the deformations under wind and earthquake loads are limited because of stability and serviceability provisions. The resultant structures are stiff enough to withstand the wind loads, without forming noticeable deformations, while simultaneously being ductile enough to withstand strong earthquakes by adopting nonlinear behaviors.

However, particularly for controlling the vibrations in tall buildings, the code-based approaches do not necessarily lead to an applicable and affordable solution, as these structures need to withstand much larger wind and earthquake loads even though they have much lower lateral stiffness compared to low- and midrise buildings. Moreover, because of their very high construction costs, they are usually designed to endure for longer time periods, which increase their risk of experiencing strong earthquakes over the course of their service life.

A modern answer to these issues is the idea of structural control systems that include a variety of techniques, which can be classified into four main categories: passive, active, semiactive, and hybrid.

From a historical point of view, passive control systems such as base isolations and tuned mass dampers (TMDs)

were the first of these techniques to be implemented. Considerable research has focused on the passive controller systems, and they are already utilized in many countries [2, 3]. As these systems need no external power supply, they are easier to implement and design, when compared to other advanced controllers. In structural control problems, TMDs have been successfully implemented in different structures such as bridges [4, 5] and buildings [6–11] to reduce earthquake- and wind-induced vibrations. Observations of TMDs show that they can effectively reduce vibrations in structures that are excited by high winds, high-speed trains, and traffic loads and also help decrease the discomfort of the inhabitants during minor earthquakes [5, 12, 13]. Under earthquake excitations, the literature shows that the performance of the TMDs decreases as the duration of excitation shortens. Therefore, the TMDs are more effective for structures subjected to narrowband long-duration far-fault (FF) excitations compared to pulse-like near-fault (NF) ground motions. As single TMD systems can be tuned to a particular frequency, they are very sensitive to mistuning and uncertainties. As a solution, multiple tuned mass dampers (MTMDs) were first introduced by Xu et al. in 1990 [14], after which they have been studied in several research studies [8, 9, 11, 15–19]. Li and Qu [20] considered the structure as a single-degree-of-freedom (SDOF) system, when connected to multiple TMDs, and studied the optimum design parameters for those TMDs. With respect to using MTMD systems in multistory buildings, Chen and Wu [8] studied the efficiency of using multiple TMDs in mitigating the seismic responses in a six-story building. After that, Sakr [15] used partial floor loads as MTMDs. These research studies show that the MTMD systems cover a wider frequency range and are less sensitive to the uncertainties of the system.

In addition to multistory buildings, several tall buildings have benefited from the utilization of TMDs in controlling their vibrations (see Figure 1).

As has been shown, most of them are equipped with a single TMD, which is placed on the top level of the building. The studies also showed that using a single TMD on the top levels of the tall buildings can effectively reduce wind-induced motions [22, 23]. This is because the structures respond to the wind excitation with respect to their first structural mode in which the top levels of the building have maximum modal displacement. Therefore, placing a single TMD on the top level with a tuning frequency closer to the fundamental structural frequency can efficiently reduce the structural responses. In another research, Elias and Matsagar [9] studied the use of distributed MTMD systems in reducing wind-induced vibrations in a tall building. They concluded that the distributed MTMDs are more effective, as compared to a single TMD system and an MTMD system in which all the TMDs are placed on the top level.

The research studies show that TMDs are also effective in mitigating earthquake vibrations in buildings. Arfiadi and Hadi [6] used a hybrid genetic algorithm method to find the optimum properties and the location of a TMD for a 10-story building under earthquake excitation. In another research, Pourzeinali et al. [24] utilized multiobjective optimization to outline the design parameters of a TMD in a 12-story building under earthquake excitation. Li [11] proposed a novel optimum criterion to optimize the properties of double TMDs for structures under ground acceleration. In another research, Elias et al. studied the effectiveness of a distributed TMD system in vibration control of a chimney [25]. The research developments in passive control of structures using TMDs are summarized by Elias and Matsagar [26].

In all the research studies about tall buildings cited here, either the parameters of the TMDs have mainly been studied under wind-induced vibrations or a single TMD has been studied under earthquake excitation; currently, studying the optimum parameters of TMDs under earthquake excitation, without limiting the number and location of TMDs, is still a challenging task because of the stochastic nature of the earthquakes and the complex seismic behavior of such buildings, which mandate extensive and thorough studies.

Additionally, in contrast to the wind loads, during earthquakes, the higher modes may have more noticeable participation in the total response of tall buildings. This is mainly because of the (1) low frequency of the higher modes in these structures, compared to low- and midrise buildings, and (2) wide frequency content of the earthquakes that may activate multiple modes in such buildings. Therefore, only controlling the lower modes by placing TMDs on the top levels would not necessarily lead to the optimum solution for controlling the motions in these buildings during earthquakes.

1.1. Problem Definition. This paper addresses the mentioned issues by studying the optimum placement and properties of TMDs in a 76-story benchmark building as the case study which is subjected to seven scaled earthquake excitations. The variables of the resultant optimization problem include the positions and properties of the TMD. The goal of the optimization is to reduce the controlled-to-uncontrolled ratio of the displacement, velocity, and acceleration seismic responses. In order to solve such multiobjective optimization problem, an improved revision of the *nondominated sorting genetic algorithm II (NSGA-II)* is developed and utilized.

In each loop, the algorithm generates an arrangement and properties of the TMDs using the NSGA-II method and sends them to the *analyzer module* to determine the responses of the building equipped with such a TMD arrangement under different earthquake excitations. Based on the responses, the algorithm assigns a fitness value for such TMD arrangements. The fitness value is an index that shows how good or bad the obtained responses are. The NSGA-II then utilizes a refined history of the TMD arrangements and corresponding fitness values for its next suggestion in the next loop. In this study, the algorithm was allowed to spend an applicable mass in a single TMD or distribute it through multiple TMDs over the height of the building.

1.2. Contributions. This research incorporates several contributions in the field of passive control of tall buildings and

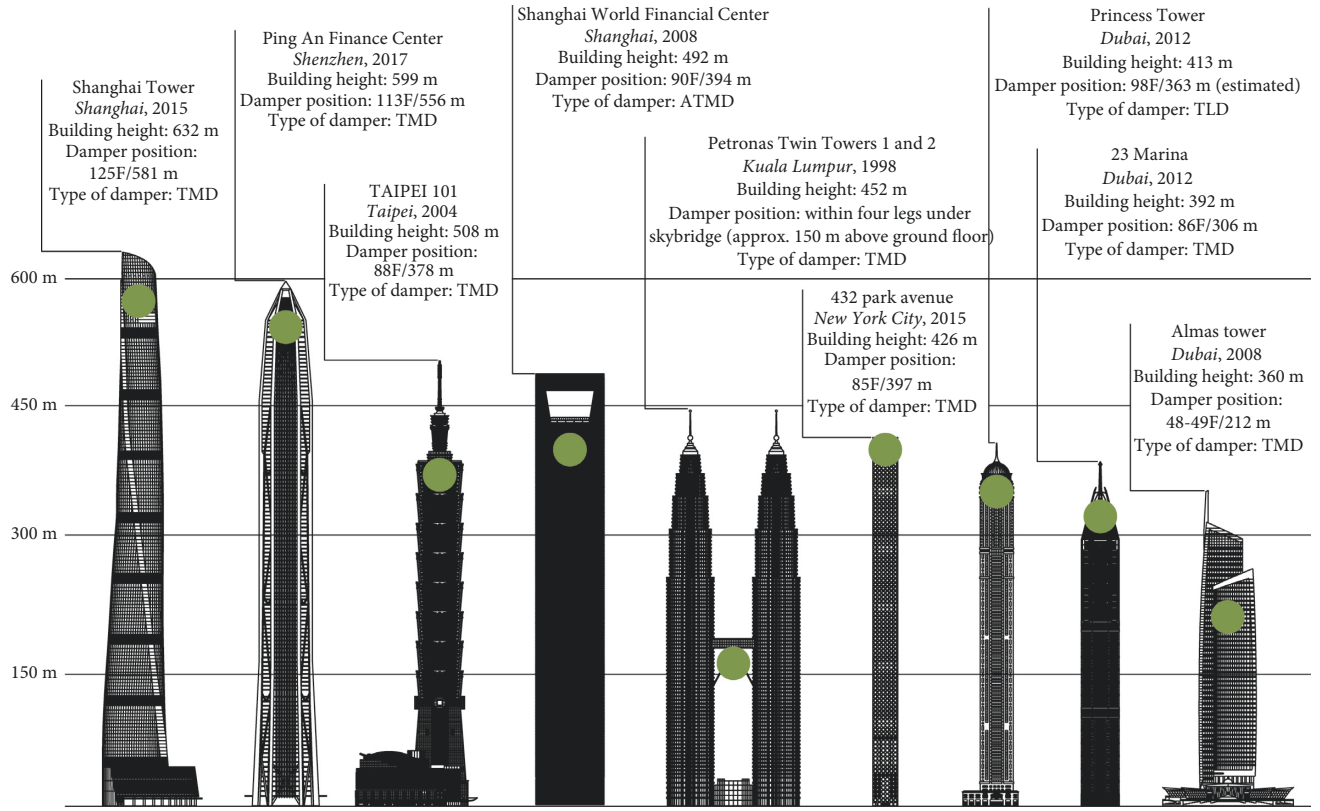

Figure 1: Tallest completed buildings with dampers [21].

optimization problems. First, the issues with a single TMD system in controlling tall buildings are addressed, and improvements are proposed by studying multimode control via distribution of the TMDs over the height of the building. Likewise, it investigates how the frequency content of the earthquake can affect the optimum position and properties of the TMDs. Moreover, the performance of the NSGA-II algorithm is enhanced by adding multivariant genetic operations, and the resulting algorithms are presented. Finally, the optimum hyperparameters of the genetic algorithm for tackling similar problems are proposed by performing sensitivity analysis.

1.3. Outlines. The mathematical settings of a structural dynamic problem are mentioned in Section 2. Then, the NSGA-II method is described in Section 3. After that, the case study is presented in Section 4, and the selection and scaling of the earthquakes are noted. Then, the results of the sensitivity analysis of the GA hyperparameters for optimizing the performance of the GA algorithm are presented, and the optimization process is then detailed in Section 7. Finally, the obtained results are presented and discussed in Sections 8 and 9, and the relevant conclusions are drawn.

2. Mathematical Model of the Building

The governing equation of the motion of a tall building under earthquake excitation is as follows:

$$[M]\{\ddot{U}\} + [C]\{\dot{U}\} + [K]\{U\} = \{P_t\}, \tag{1}$$

where M, K, and C represent the mass, the stiffness, and the damping matrices of the structure and the TMDs:

$$\begin{aligned} [M] &= [M_{st}] + [M_t], \\ [C] &= [C_{st}] + [C_t], \\ [K] &= [K_{st}] + [K_t]. \end{aligned} \tag{2}$$

Indexes *st* and *t* indicate the degree of freedom (DOF) of the building and the TMDs, respectively.

The external load vector, P_t, in Equation (1) comprises inertial forces due to ground accelerations as follows:

$$\{P_t\} = -\ddot{u}_g [M]\{1_t\}, \tag{3}$$

where $\{1_t\}_{(N+n)\times 1} = [1, 1, \ldots, 1]^T$ and the term $\ddot{u}_g$ represents the ground accelerations.

The structural responses, including displacement, velocity, and acceleration matrices, can be expressed as follows:

$$\begin{aligned} \{U\} &= \{u_{st1}, u_{st2}, \ldots, u_{stN}, u_{t1}, u_{t2}, \ldots, u_{tn}\}, \\ \{V\} &= \{v_{st1}, v_{st2}, \ldots, v_{stN}, v_{t1}, v_{t2}, \ldots, v_{tn}\}, \\ \{A\} &= \{a_{st1}, a_{st2}, \ldots, a_{stN}, a_{t1}, a_{t2}, \ldots, a_{tn}\}, \end{aligned} \tag{4}$$

where N and n represent the number of DOFs (DOF) for the building and the TMDs, respectively. Therefore, the dimensions of the M, K, and C matrices are $(N + n) \times (N + n)$.

The design parameters of a TMD include its damping, tuning frequency, and mass. Generally, the ratios of these parameters to the corresponding values of the structures have more importance and are utilized in the design procedures:

$$m_0 = \frac{m_t}{m_{st}},$$
$$\beta = \frac{\nu_t}{\nu_{st}}, \quad (5)$$
$$\psi = \frac{c_t}{c_{st}},$$

where the parameters m_0, β, and ψ refer to mass, frequency, and damping ratios, while the indexes t and st indicate the TMD and the structural properties.

In order to solve the equations of the motion, Newmark's β method is utilized. The average acceleration method is considered by setting $\gamma = 1/2$ and $\beta = 1/4$ in the related formulations [27].

3. The Fast and Elitist Multiobjective Genetic Algorithm NSGA-II

3.1. Introduction. In this paper, the NSGA-II method [28] is utilized to investigate the optimum arrangement and properties of TMDs in a tall building. NSGA-II is a nondomination-based genetic algorithm invented for multiobjective optimization problems. In this method, the initial population is randomly generated, as in a normal GA procedure, and then the algorithm sorts the population with respect to the *nondomination rank* and the *crowding distance*.

In general, X dominates Y if X is no worse than Y in all the objectives and if X is better than Y in at least one objective.

Among the nondominated solutions or a union of the first ranks of nondominated solutions, NSGA-II seeks a broad coverage. This will be achieved by crowding distance, which is the Manhattan distance between the left and right neighboring solutions for two objectives.

3.2. Repair. The repair method makes infeasible solutions feasible. Figure 2 schematically shows the repair approach for a solution space with an infeasible solution and two solutions in the feasible region. In this research, an infeasible solution includes the out-of-limit properties for TMDs. As is shown, the repair function would project each of these infeasible solutions to the closest feasible solution. The developed repair function calculates the shortest distance of the TMD properties (m_0, β, and ψ) in the infeasible solution and corrects the chromosome with respect to the calculated distance (see Algorithm 1).

3.3. Selection. The objective of *selection* is to choose the fitter individuals in the population to create offsprings for the next generation and then place them in a group commonly known as the mating pool. The mating pool is then subjected to further genetic operations that result in advancing the population to the next generation and hopefully closer to the optimal solution. In this research, the roulette wheel selection method was utilized for developing the selector function. As is also shown in Algorithm 2, the algorithm selects the individuals based on a probability proportional to the fitness. As is schematically illustrated in Figure 3, the principle of roulette selection is a linear search through a roulette wheel with the slots in the wheel weighted in proportion to the individual's fitness values. All the chromosomes (individuals) in the population are placed on the roulette wheel according to their fitness value [30]. In this algorithm, a probability value is assigned to each individual in the population. Based on these probabilities, the ranges [0, 1] are divided between the individuals so that each individual obtains a unique range. The winning individual is then selected by generating a random number between zero and one and finding the individual whose range includes this random number.

In this algorithm, the *ADDRANGE* function assigns a range to each individual based on their fitness value and their position on the wheel and the *RND(1)* function generates a random value between zero and one.

3.4. Optimization Variables. In this study, three variables were defined to be optimized by the NSGA. As is schematically shown in Figure 4, the variables are as follows:

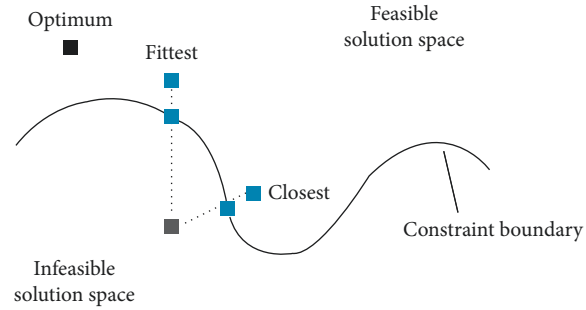

Figure 2: Repair of an infeasible solution [29].

```
procedure Repair(individual)
  st = Decoder(individual)
  for each tmd in st
    for each property in tmd
      if not property in acceptableRange
        property = ClosestInRange(property)
      end if
    tmd = Renew(tmd, property)
    end for
  newIndividual = Coder(st)
  end for
  return newIndividual
end procedure
```

Algorithm 1: Repairing individuals.

```
procedure MAKINGSELECTION(population)
    fitPop = FITNESS(population)
    sumFit = SUM(fitPop)
    percentFit = fitPop/sumFit
    rangeFitAdded = ADDRANGE(fitPop, percentFit)
    randN = RND(1)
    for each individual in population
        r = rangeFitAdded(individual)
        if randN in range r
            selectedIndv = individual
            exit
        end if
    end for
    return selectedIndv
end procedure
```

ALGORITHM 2: Making individual selection.

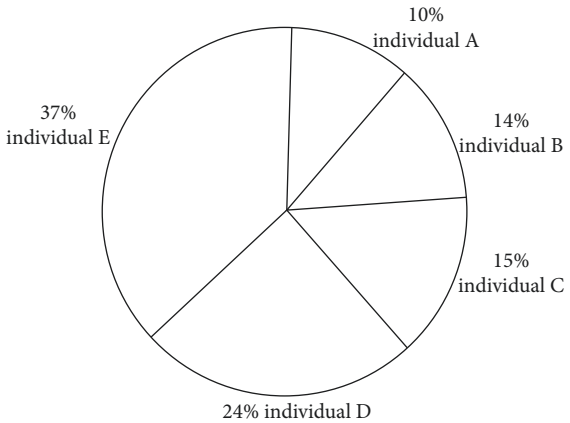

FIGURE 3: Roulette wheel selection.

(1) Number of TMDs

(2) Position of the TMDs $\longrightarrow$ story number

(3) TMDs' properties $\longrightarrow$ m_0, β, and ψ

The variation domain for m_0, β, and ψ is considered to be in an applicable range, as shown in Table 1. The maximum value of the total mass ratio of TMDs, $m_t = \sum_{i=1}^{n} m_{0i}$, is limited to 3%, which is equal to the considered limit for each TMD. This allows the GA algorithm to either spend the allowable mass in a single TMD or divide it among multiple TMDs and distribute them over the height of the building. As is shown, the damping and the frequency ratio of the TMDs are also limited to applicable values.

3.5. Encoding. In this research, binary coding has been considered for creating genes. Therefore, the design variables of each TMD are coded into a binary string with a constant number of genes as shown in Figure 5. Each offspring contains the design parameters for the TMD as follows:

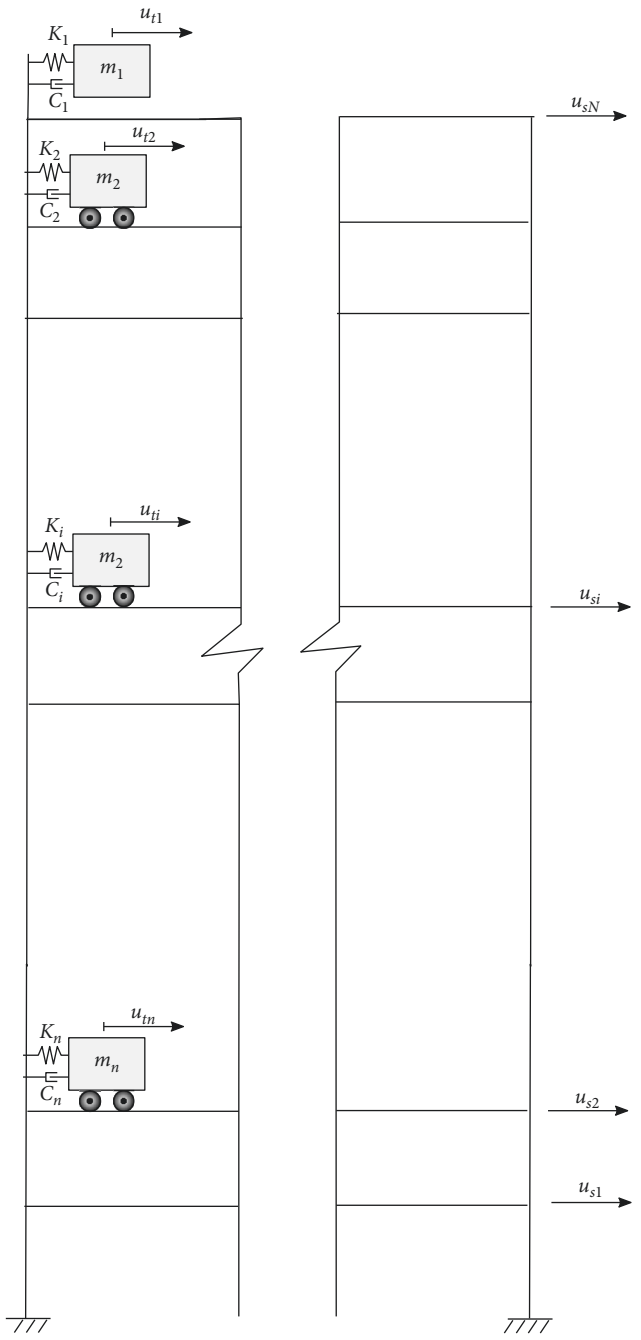

FIGURE 4: Building equipped with TMDs.

$$m_0 = \frac{m_t}{m_{st}},$$

$$\beta = \frac{\nu_t}{\nu_{st}}, \tag{6}$$

$$\xi = \frac{c_t}{c_{st}},$$

where the t and st indexes correspond to the TMD and the structure, respectively.

Table 1: Parameter variation domain for TMDs.

Parameters	Min. value	Max. value
m_t (%)	—	3
m_0 (%)	0.2	3
β	0.8	1.3
ψ	5	40

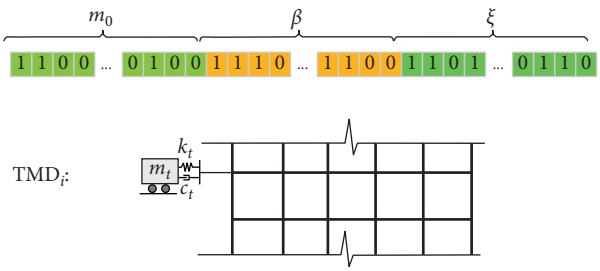

Figure 5: Binary coding the TMD's properties.

After developing the genes for each TMD, the chromosomes are then created by combining all genes for each solution. As a result, each chromosome contains the coded data of all TMDs in the building. Using this definition, the position of each TMD is represented by the position of the related genes in the chromosome.

3.6. Genetic Operators

3.6.1. Crossover Function. In the crossover operation, two selected parents exchange random parts of their chromosome to create new offsprings. An appropriate strategy for selecting locations of the split points and the length of the transferred genes depends on the problem characteristics that highly affect the performance of the algorithm and the quality of the final results.

In this regard, different alternatives have been studied in this research to develop an appropriate crossover function. Examples of crossover operation forms that have been utilized in other research studies but were not appropriate for this research are discussed as follows:

(1) Single/k-Point Crossover: Random Points in Whole Chromosome. In the initial steps, a completely random selection of the genes for crossover has been considered as a commonly used crossover function. In this crossover type, after the parents are nominated by the algorithm, one or k points in the chromosome are randomly selected, and the new offsprings are created by splitting and combining the parents' chromosomes at the selected points. This process has often resulted in producing too many meaningless and low-quality offsprings, consequently reducing the performance of the algorithm dramatically. Examples of meaningless offsprings can include TMDs without one or more properties (e.g., without mass or stiffness).

(2) Single/k-Point Crossover: Random Points in TMD Genes. Preventing the production of meaningless offsprings, the crossover function was improved in this study so that the genes related to the TMDs in each parent could be selected for performing a k-point crossover. Although the chance of creating meaningless offsprings was noticeably reduced, the results showed that the efficiency of the operator in improving the results was not acceptable, as following this process, all the genes within the considered range for a TMD would be subjected to the same operations regardless of the genes' positions.

For example, the genes related to the stiffness of a TMD in a parent were exchanged with those related to the damping properties in another parent, which is not logical. As a result, despite its improvements compared to the first type, the second crossover type leads to a very low convergence rate because of the production of low-quality offsprings. In addition, one possible shortcut for reaching an optimum solution was missed; this step involves attaching the TMD of one parent to a story in another parent.

However, the maximum convergence rate obtained by developing a two-variant crossover function is presented in Algorithm 3. As is shown, in this function, in each call, one of the two developed crossover variants would be selected randomly. These variants are described as follows:

(i) Variant 1: in the first variation, the crossover operator acts on each of the parameters of the TMDs separately using the k-point crossover method, meaning that, in each call, the crossover operator acts on the stiffness, mass, or damping of the parents and exchanges the related properties using the k-point crossover function. The produced offsprings have TMDs in the same locations as their parents, but with different properties. Investigation of the performance of this function showed that this variant improves the parameters of the TMDs regardless of their positions.

(ii) Variant 2: the second crossover variation acts on the location of TMDs in the parents. The resultant offsprings include TMDs with the same properties as their parents but in other stories. These two crossover variations are demonstrated in Figure 6.

3.6.2. Mutation Function. In the genetic algorithm, the mutation operator randomly changes one or multiple genes of a parent to produce new offsprings. Generally, in the binary coded chromosome, the following function is utilized to change the genes:

$$\text{Binary mutation (gen)} = \begin{cases} 1, & \text{if gen value} = 0, \\ 0, & \text{if gen value} = 1. \end{cases} \quad (7)$$

In GA problems, the mutation function helps the algorithm to explore the solution space more broadly and prevents it from sticking to the local minimums. In addition, a proper mutation function improves the convergence speed. In this research, in order to develop an appropriate mutation function, different variants were studied. It is understood that developing the mutation function without considering the characteristics of the problem would result in producing meaningless

```
(1) procedure CROSSOVER(individual1,individual2)
(2)    if rnd(1) < 0.5
(3)       rndTmd1 = RANDOMSELECT TMD in individual1
(4)       rndTmd2 = RANDOMSELECT TMD in individual2
(5)       k = rndint(3)
(6)       tmd1New = K-POINTCROSSOVER(rndTmd1)
(7)       tmd2New = K-POINTCROSSOVER(rndTmd2)
(8)       offspring1 = REBUILD(individual1, tmd1New)
(9)       offspring2 = REBUILD(individual2, tmd2New)
(10)   else
(11)      rndTmd1 = RANDOMSELECT TMD in individual1
(12)      rndTmd2 = RANDOMSELECT TMD in individual2
(13)      tmd1New = rndTmd2
(14)      tmd2New = rndTmd1
(15)      offspring1 = REBUILD(individual1, tmd1New)
(16)      offspring2 = REBUILD(individual2, tmd2New)
(17)   end if
(18)   return (offspring1, offspring2)
(19) end procedure
```

ALGORITHM 3: Crossover operator.

offsprings. Keeping this in mind, a two-variant mutation function was developed, which acted on the (1) genes related to TMD parameters and (2) group of genes related to the location of the TMDs (See Algorithm 4).

3.7. Fitness Function. During the GA procedure, each solution comprised an arrangement of TMDs with different parameters. In order to evaluate an individual solution, three objective functions were defined to shape the fitness function. The objectives of the optimization were taken to be the maximum ratios of displacement, velocity, and acceleration responses in controlled condition to their uncontrolled values as follows:

$$J_1 = \max.\left(\frac{u_i^C}{u_i^{UC}}\right)_{i=1,\ldots,N},$$

$$J_2 = \max.\left(\frac{v_i^C}{v_i^{UC}}\right)_{i=1,\ldots,N}, \quad (8)$$

$$J_3 = \max.\left(\frac{a_i^C}{a_i^{UC}}\right)_{i=1,\ldots,N},$$

where i is the story number and N is the number of stories in the building. The pseudocode of the developed fitness function is presented in Algorithm 5.

4. Benchmark Building

As a case study, a 76-story, 306 m tall official building consisting of the concrete core and concrete frames was considered. The total mass of the building was 153,000 tonnes. The initial mathematical model of the building included 76 transitional and 76 rotational degrees of freedom in which the rotational degrees of freedom were then removed by the static condensation method to create a 76-degree-of-freedom model. The damping matrix of the building was calculated by considering a 1% damping ratio for the first five modes using Rayleigh's approach.

The first five natural frequencies of the building were 0.16, 0.765, 1.992, 3.79, and 6.39 Hz. The first five mode shapes of the building are presented in Figure 7.

5. Ground Motion Selection

In this research, the ground motions were selected and scaled using an intensity-based assessment procedure, considered according to ASCE/SEI 07-10. In this regard, seven earthquakes' real acceleration records were selected from the Pacific Earthquake Engineering Research Center (PEER) NGA strong motion database [31] (see Figure 8) and then scaled using a design response spectrum [32, 33]. The peak ground acceleration (PGA) and other seismic parameters of the considered design response spectrum are shown in Table 2.

The specifications of the nonscaled and scaled selected earthquakes are presented in Tables 3 and 4. The spectra of the nonscaled and scaled excitations are shown in Figure 9.

6. Sensitivity Analysis of Genetic Algorithm Parameters

As the parameters of GAs are highly dependent on the characteristics of each particular problem [34], the sensitivity analysis on the GA parameters was performed and the optimum values were studied. Utilization of the obtained values for the GA parameters resulted in improving the quality of the solutions and the performance of the algorithm. As is shown in Table 5, during the sensitivity analysis, the crossover and mutation probabilities were iterated, and the GA results were compared for the El Centro earthquake excitation.

The results were then sorted using the NSGA function, and the pareto fronts were obtained, as shown in Table 6. Considering the first pareto set in this table, the resultant optimum values for crossover and mutation probabilities were 0.7 and 0.2, respectively.

As a result, the parameters of the NSGA-II were considered as they are shown in Table 7. The sufficiency of 500 generations as the limit for the number of generations was then evaluated, as shown in Figure 10.

7. Optimization Process

In order to study the optimum arrangement and properties of the TMD in the benchmark building, a computer code was developed based on the previously discussed theories and functions. The pseudocode of the program is presented in Algorithm 6. In order to improve the performance of the developed code and reduce the computation time, some advanced computer programming techniques, such as parallel computing, were utilized. As a result, the code utilized multiple CPU cores to produce multiple populations in parallel, and then all the populations were combined and sorted in each generation.

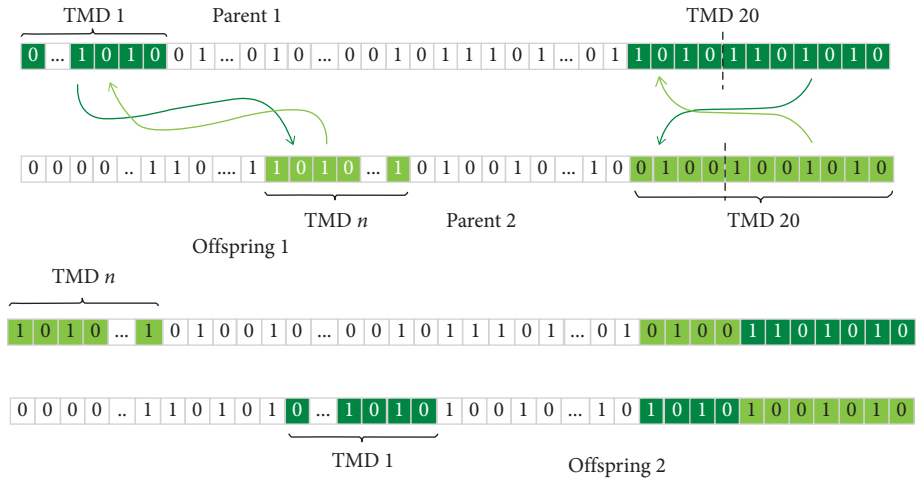

Figure 6: Crossover types.

```
(1) procedure MUTATION(individual)
(2)   if rnd(1) < 0.5
(3)     rndTmd = RANDOMSELECT TMD in individual
(4)     newStory = rndint(76)
(5)     tmdNew = MOVETMD(rndTmd, newStory)
(6)     offspring = REBUILD(individual, tmdNew)
(7)   else
(8)     rndTmd = RANDOMSELECT TMD in individual
(9)     targetGenCount = rndint(10)
(10)    for i = 1 to targetGenCount
(11)      targetGen = RANDOMSELECTGEN(rndTmd)
(12)      mutTmd = BINARYMUTATION(rndTmd, targetGen)
(13)    end for
(14)    offspring = REBUILD(individual, tmdNew)
(15)  end if
(16)  return (offspring)
(17) end procedure
```

Algorithm 4: Mutation operator.

```
(1) procedure FITNESS(benchmarkData, individualTmdAdded, excitation)
(2)   {u_max^controlled, v_max^controlled, a_max^controlled} = MAXRESPONSE(benchmarkData, individualTmdAdded, excitation)
(3)   type {u_max^uncontrolled, v_max^uncontrolled, a_max^uncontrolled} as constant
(4)   j1 = u_max^controlled \ u_max^uncontrolled
(5)   j2 = v_max^controlled \ v_max^uncontrolled
(6)   j3 = a_max^controlled \ a_max^uncontrolled
(7)   indvFitnessAdded = [individualTmdAdded, {j1, j2, j3}]
(8)   return (indvFitnessAdded)
(9) end procedure
```

Algorithm 5: Fitness of individuals.

8. Results

The results of the optimization process, including the optimum arrangement of the TMDs and their properties, are shown in Figures 11–17. The drift and acceleration responses for the top story, as the critical story, are summarized in Table 8. As shown, the optimum number of TMDs is more than one for some of the excitations.

The maximum number of TMDs is three, which corresponds to Bam and Manjil excitations, placed in 76, 75,

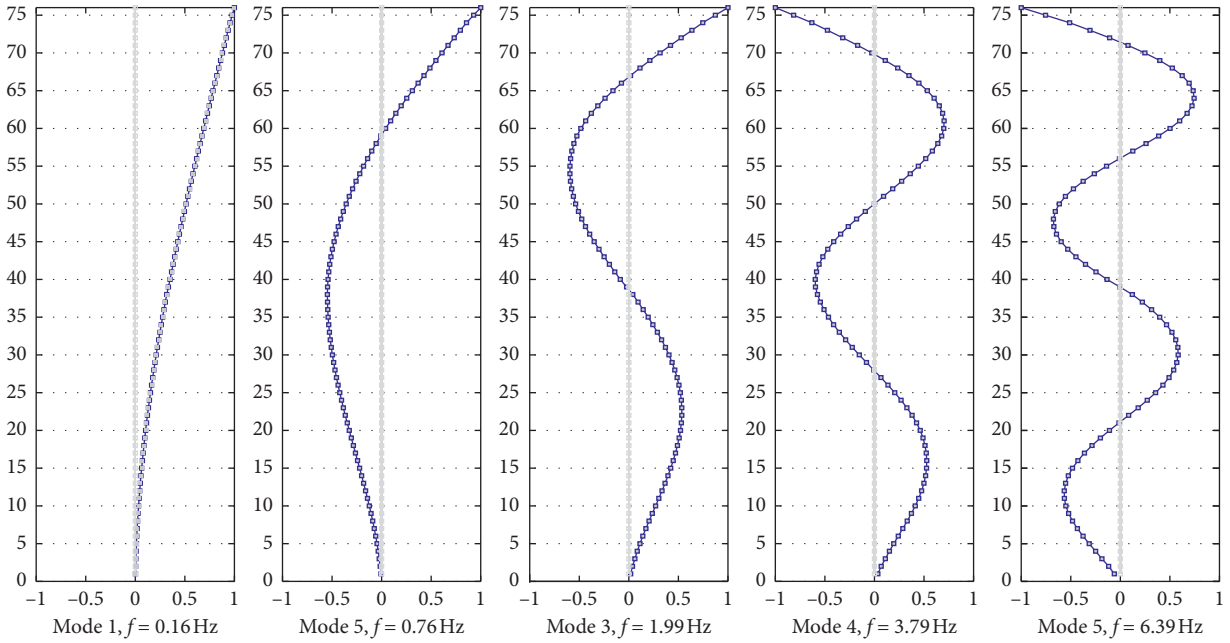

Figure 7: Five mode shapes of the 76-story building.

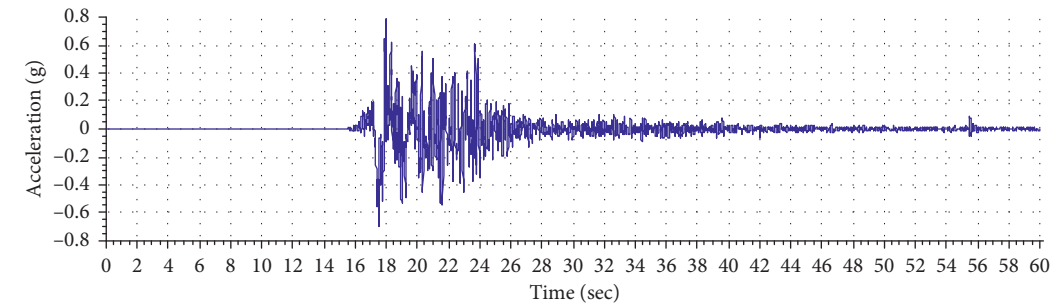

(a)

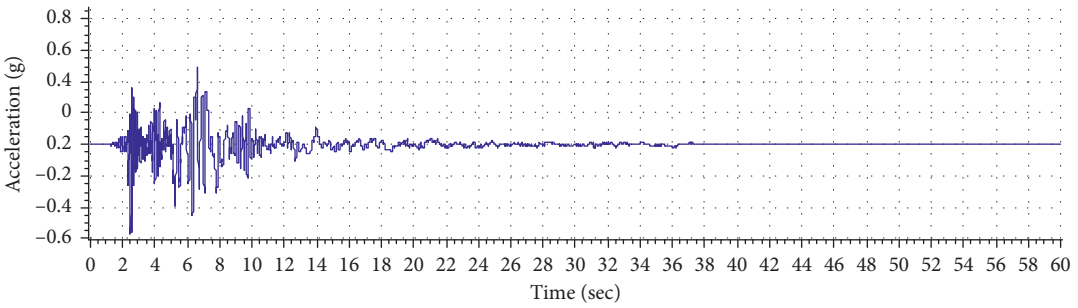

(b)

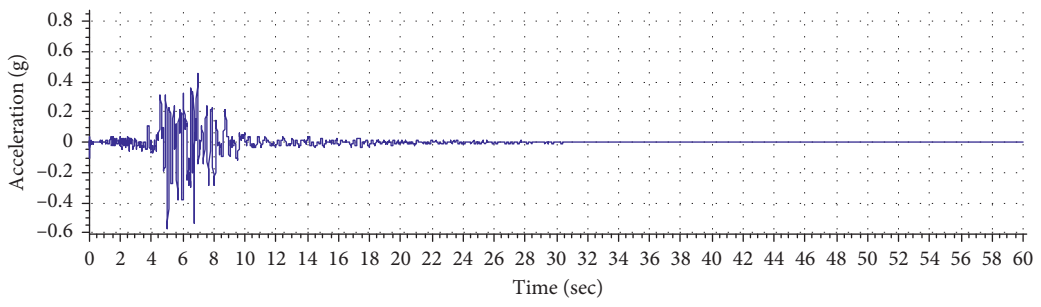

(c)

Figure 8: Continued.

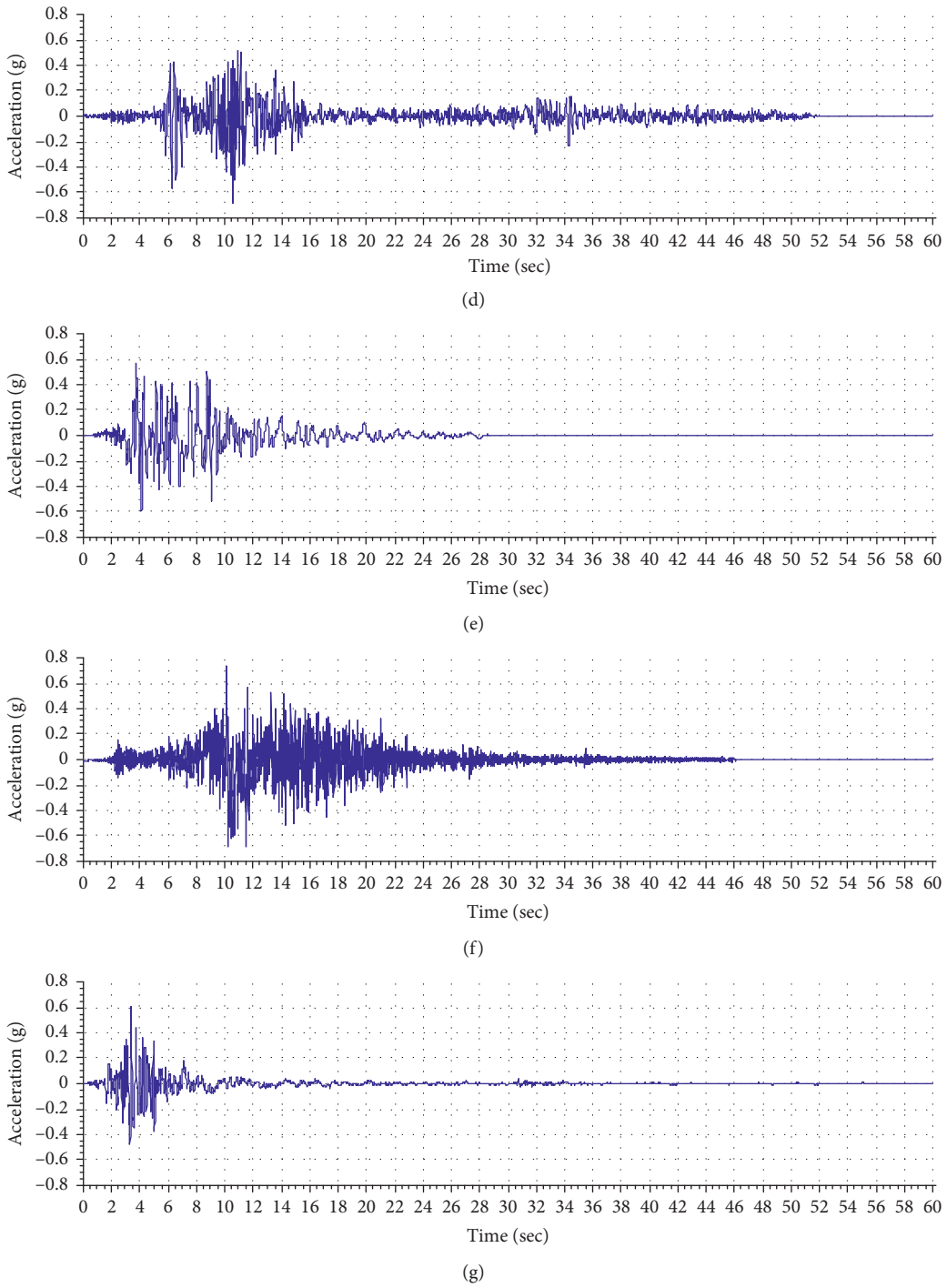

Figure 8: Earthquake acceleration records obtained from Pacific Earthquake Engineering Research Center (PEER) [31]. (a) Bam, Iran, 2003. (b) El Centro, USA, 1940. (c) Kobe, Japan, 1995. (d) Manjil, Iran, 2002. (e) Northridge, USA, 1971. (f) Landers, USA, 1992. (g) San Fernando, USA, 1994.

Table 2: Parameters of the design response spectrum.

Site class	PGA	S_s	S_1	F_a	F_v	S_{MS}	S_{M1}	S_{DS}	S_{D1}
B	0.919	2.431 g	0.852 g	1	1	2.431 g	0.852 g	1.621 g	0.568 g

Table 3: Original earthquakes' specifications.

Accelerogram	Max. acceleration (g)	Max. velocity (cm/sec)	Max. displacement (cm)	Effective design acceleration (g)	Predominant period (sec)	Significant duration (sec)
Bam	0.80	124.12	33.94	0.69	0.20	8.00
El Centro	0.44	67.01	27.89	0.30	0.06	11.46
Kobe	0.31	30.80	7.47	0.28	0.42	6.20
Manjil	0.51	42.45	14.87	0.47	0.16	28.66
Northridge	0.45	60.14	21.89	0.45	0.42	10.62
Landers	0.72	133.40	113.92	0.52	0.08	13.15
San Fernando	0.22	21.71	15.91	0.20	0.00	13.15

Table 4: Scaled earthquakes' specifications.

Accelerogram	Max. acceleration (g)	Max. velocity (cm/sec)	Max. displacement (cm)	Effective design acceleration (g)	Predominant period (sec)	Significant duration (sec)
Bam	0.78	128.55	33.95	0.64	0.20	8.24
El Centro	0.57	75.76	28.36	0.48	0.32	9.16
Kobe	0.56	38.83	15.68	0.56	0.36	4.16
Manjil	0.68	42.06	15.02	0.55	0.08	28.26
Northridge	0.59	64.57	22.16	0.58	0.40	10.40
Landers	0.73	141.02	113.78	0.56	0.08	12.92
San Fernando	0.60	23.71	15.88	0.61	0.10	6.03

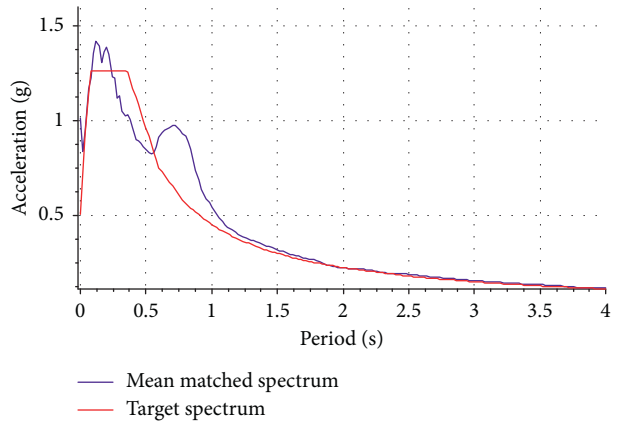

Figure 9: Mean matched spectrum compared to the target spectrum.

Table 5: Crossover and mutation variations.

Variation no.	Crossover	Mutation	J_1	J_2	J_3
1	0.6	0.1	0.845	0.917	0.941
2		0.2	0.860	0.926	0.950
3		0.3	0.855	0.924	0.948
4		0.4	0.839	0.915	0.942
5	**0.7**	0.1	0.862	0.925	0.946
6		**0.2**	**0.835**	**0.913**	**0.939**
7		0.3	0.861	0.925	0.947
8		0.4	0.846	0.919	0.944
9	0.8	0.1	0.869	0.929	0.950
10		0.2	0.876	0.932	0.952
11		0.3	0.842	0.915	0.941
12		0.4	0.852	0.922	0.947
13	0.9	0.1	0.871	0.930	0.951
14		0.2	0.866	0.927	0.947
15		0.3	0.874	0.932	0.953
16		0.4	0.839	0.913	0.939

Table 6: NSGA of crossover and mutation variations.

Pareto front	Crossover variation no.	Mutation variation no.
1	**6**	—
2	16	—
3	4	11
4	1	—
5	8	—
6	5	12
7	3	7
8	2	14
9	9	—
10	13	—
11	10	15

Table 7: Initial parameters of NSGA-II.

Number of generations	Population size	Crossover probability	Mutation probability
500	100	0.7	0.2

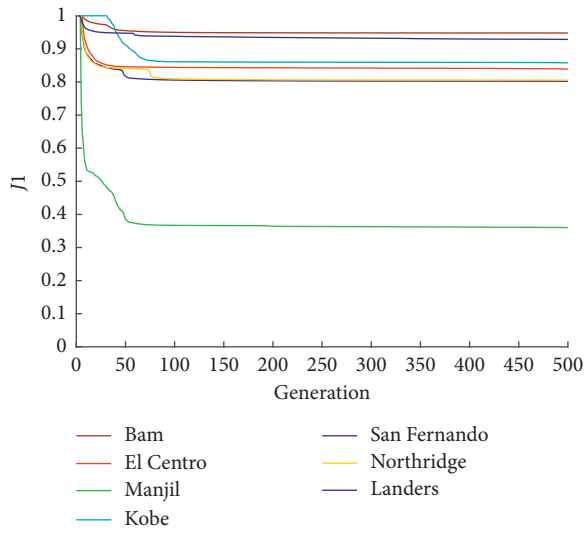

Figure 10: Trend of objectives during the generations.

and 64th floors in both cases. Under both sets of excitations, most of the mass for the TMDs was dedicated to those on the top two floors. The tuned frequency of the TMDs was close to the fundamental frequency of the building for the top two TMDs and about 1.24 times the fundamental frequency for the TMD in the 64th-floor building. The damping ratio of the TMDs placed on the top two stories was close to the maximum allowed value, which was 40, while it was about 14 for the TMD in the 64th-floor building.

It was observed that the controlled displacement responses of the building improved substantially by about 65% under the Manjil earthquake excitation. On the contrary, the objective J_1 for the Bam earthquake had a value of about 0.95, which means to about 5% improvement in reducing maximum displacements, compared to the uncontrolled response. This low objective value was also obtained under the Landers earthquake, with a value of about 0.93 for J_1, implying 7% improvement in reducing the displacement responses. However, the displacement response shows substantial improvements in damping further oscillations compared to uncontrolled buildings.

For Landers, Northridge, and San Fernando earthquakes, the TMDs were placed on stories 76 and 74, and most of the allowed mass was dedicated to the TMD on the roof. The optimum tuning frequency of the TMDs was close to the fundamental frequency of the building. The damping values of the TMDs were between 36.39 and 39.78, which were close to the maximum considered damping ratio.

For the El Centro and Kobe earthquakes, the optimum results were obtained by placing a single TMD system on the roof. In both cases, all the allowed mass was utilized in the TMD. Under these excitations, the frequency ratios of the TMDs were registered as 1.06 and 1.05, which indicated a tuning frequency closer to the fundamental frequency of the building; the damping ratios of the TMDs were 39.53 and 39.78, which were close to the maximum allowed value.

9. Discussion

As mentioned in Results, the optimum target stories for placing the TMDs included the top two stories for all of the earthquake excitations and some other stories such as 74 and 64 for some of the earthquakes. In order to understand the reasons behind this optimum arrangement, the building's mode shapes are again presented in Figure 18, but in each mode, the stories with maximum displacements are also marked. As shown, for the first three modes, the top three stories have the maximum displacements. The roof and the 75th and 61st stories, for the 4th mode, and the roof and the 75th and 64th stories, for the 5th mode, were the stories with maximum modal displacements.

Consequently, it can be concluded that placing a TMD on the top stories would improve the modal displacements in all five modes, an observation which agrees with the optimization results.

On the contrary, for some earthquakes, TMDs were placed in the lower stories, which implies that the optimum placement of the TMDs may also be related to some excitation parameters. For this reason, fast Fourier transformation (FFT) was performed for each earthquake's excitation record, and amplitudes for each building's mode frequency were then specified to investigate the effective properties of the excitations, as shown in Figure 19.

As shown here, unlike other earthquakes, for the Bam and Manjil earthquakes, the amplitude of the excitation in the 4th and 5th modes is more than that in the lower modes. As a result, although these higher modes have lower mass participation factors, their participation in the total response of the earthquake is increased by higher excitation amplitudes. In order to theoretically study these results, the displacement response of the building under the ground motion is presented in equation (9) as sum of the modal nodal displacements:

$$\mathbf{u}(t) = \sum_{n=1}^{N} \mathbf{u}_n(t), \tag{9}$$

```
(1) population = InitializePopulation()
(2) repeat
(3)    repeat
(4)       {parent1, parent2} = MakeSelection (population)
(5)       if rnd(1) ≥ crossoverProbability
(6)          {offspring1, offspring2} = Crossover(parent1, parent2)
(7)          Repair(offsprint1, offspring2)
(8)          ComputeFitness(offsprint1, offspring2)
(9)       end if
(10)      if rnd(1) ≥ mutationProbability
(11)         {offspring1, offspring2} = Mutation(parent1, parent2)
(12)         Repair(offsprint1, offspring2)
(13)         ComputeFitness(offsprint1, offspring2)
(14)   until size(population) ≤ M
(15)   tempPopulation = population
(16)   newPopulation = [ ]
(17)   repeat
(18)      p = ParetoFront(tempPopulation)
(19)      ps = CrowdingDistance(p)
(20)      newPopulation = newPopulation + ps
(21)      tempPopulation = tempPopulation-ps
(22)   until size(tempPopulation) > 2
(23)   population = newPopulation
(24) until generationNumber ≤ N
```

Algorithm 6: NSGA-II.

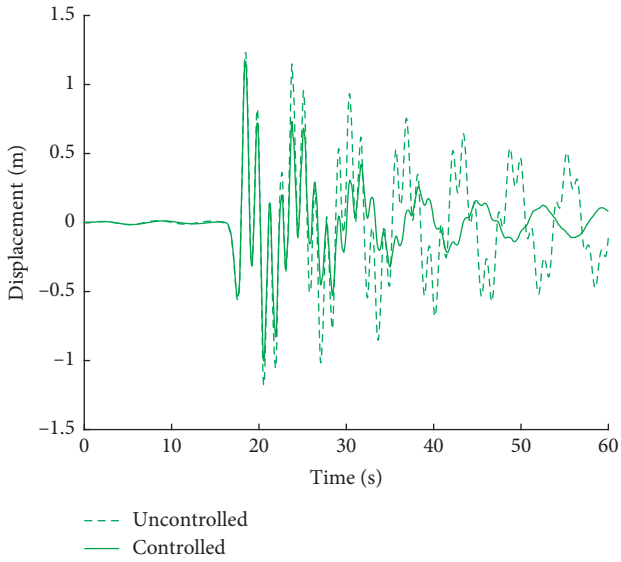

(a)

Story	m_0	β	ψ
76	1.43	0.98	39.53
75	0.93	1.01	39.46
64	0.64	1.24	18.37

(b)

J_1	J_2	J_3
0.95	0.88	0.83

(c)

Figure 11: Uncontrolled/controlled responses under the Bam earthquake. (a) Roof displacement response. (b) TMD specifications. (c) Objective values.

where $\mathbf{u}_n$ represents the nth mode's displacements. The contribution of the nth mode to the nodal displacement $\mathbf{u}(t)$ is

$$\mathbf{u}_n(t) = \phi_n q_n(t), \tag{10}$$

where q_n refers to the modal coordinate which can be calculated from the following equation:

$$\ddot{q}_n + 2\zeta_n \omega_n \dot{q}_n + \omega_n^2 q_n = -\Gamma_n \ddot{u}_g(t), \tag{11}$$

where Γ_n is the modal participation factor of the nth mode and is the degree to which the nth mode participates in the total response. The modal participation factor can be calculated based on the modal displacements and masses as follows:

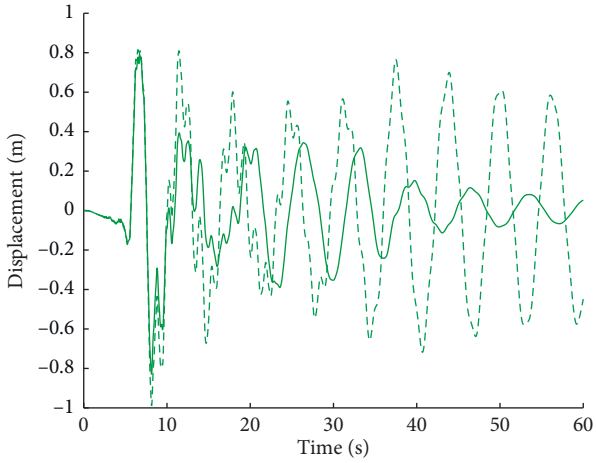

(a)

Story	m_0	β	ψ
76	2.99	1.06	39.53

(b)

J_1	J_2	J_3
0.84	0.91	0.93

(c)

FIGURE 12: Uncontrolled/controlled responses under the El Centro earthquake. (a) Roof displacement response. (b) TMD specifications. (c) Objective values.

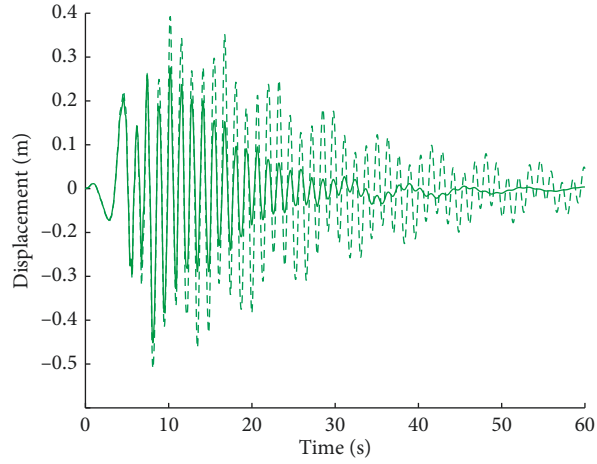

(a)

Story	m_0	β	ψ
76	3.00	1.05	39.78

(b)

J_1	J_2	J_3
0.86	0.90	0.97

(c)

FIGURE 13: Uncontrolled/controlled responses under the Kobe earthquake. (a) Roof displacement response. (b) TMD specifications. (c) Objective values.

$$\Gamma_N = \frac{\{\phi_n\}[M]\{1\}}{\{\phi_n\}^T[M]\{\phi_n\}} = \frac{\sum_{j=1}^{N} m_j \phi_{jn}}{\sum_{j=1}^{N} m_j^n \phi_{jn}^2}. \quad (12)$$

Equation (11) is related to a single-degree-of-freedom (SDOF) system with frequency and damping corresponding to the nth mode.

As shown here, in each mode n, the nodal displacement $\mathbf{u}_n(t)$ has a direct relationship with the modal displacements, ϕ_n, which means that the stories with maximum modal displacements would have greater participation in the building's modal response. In addition, it is obvious that the modal response in the nth mode is also related to the frequency content of the earthquake excitation, $\ddot{u}_g$, which means that a larger acceleration amplitude at that mode's frequency would result in larger modal responses for that mode.

Therefore, the participation of a particular story in the total response of the building would be more than that of the other stories if the following conditions are met:

(1) The story has maximum modal displacement in the modes with a larger modal participation factor

(2) The story has maximum modal displacement in the nth mode with a lower participation factor, but the ground motion has a larger Fourier transformation amplitude in the nth mode's frequency (f_n)

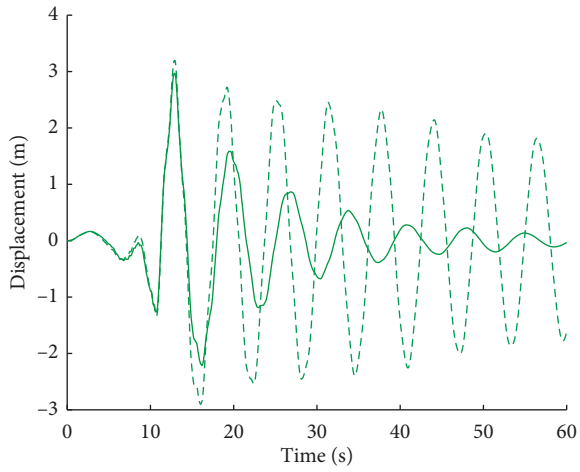

(a)

Story	m_0	β	ψ
76	2.01	1.01	37.07
74	1.00	1.01	37.13

(b)

J_1	J_2	J_3
0.93	0.89	0.98

(c)

Figure 14: Uncontrolled/controlled responses under the Landers earthquake. (a) Roof displacement response. (b) TMD specifications. (c) Objective values.

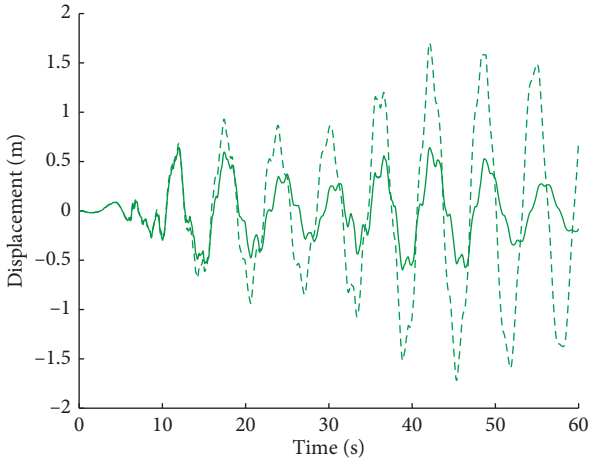

(a)

Story	m_0	β	ψ
76	1.50	1.02	35.12
75	0.95	1.01	31.34
64	0.55	1.21	14.92

(b)

J_1	J_2	J_3
0.36	0.57	0.95

(c)

Figure 15: Uncontrolled/controlled responses under the Manjil earthquake. (a) Roof displacement response. (b) TMD specifications. (c) Objective values.

These derivations validate the possibility of placing the TMDs in stories other than the top stories, a conclusion that agrees with the optimization results.

10. Conclusion

Considering the obtained results and related discussions in previous sections, the following conclusions can be drawn:

(1) Compared to a single TMD on the roof level, a distributed MTMD system is more efficient in improving structural responses with the same amount of masses under excitation for earthquakes that have noticeable amplitude at the structure's frequencies at higher modes, a scenario likely to happen within the lifetime of a tall building.

(2) The optimum stories for placement of the TMDs includes

(a) The stories with maximum modal displacements in the lower structural modes

(b) The stories with maximum modal displacements in modes with frequencies at which the earthquake excitation has noticeable amplitudes

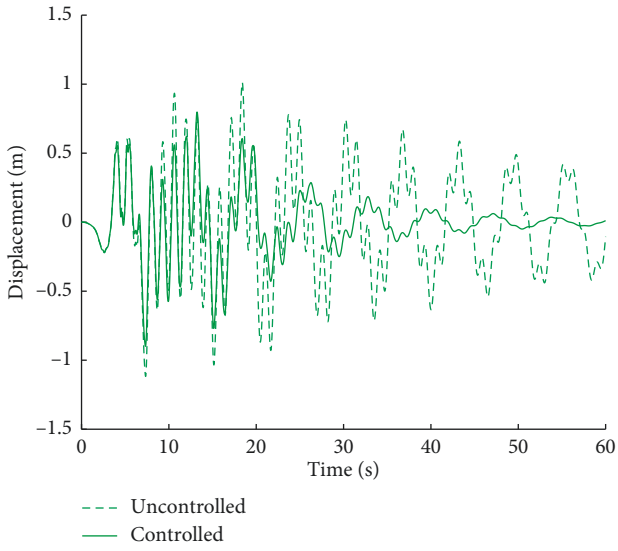

(a)

Story	m_0	β	ψ
76	2.26	1.04	37.05
74	0.75	1.04	36.98

(b)

J_1	J_2	J_3
0.81	0.84	0.95

(c)

Figure 16: Uncontrolled/controlled responses under the Northridge earthquake. (a) Roof displacement response. (b) TMD specifications. (c) Objective values.

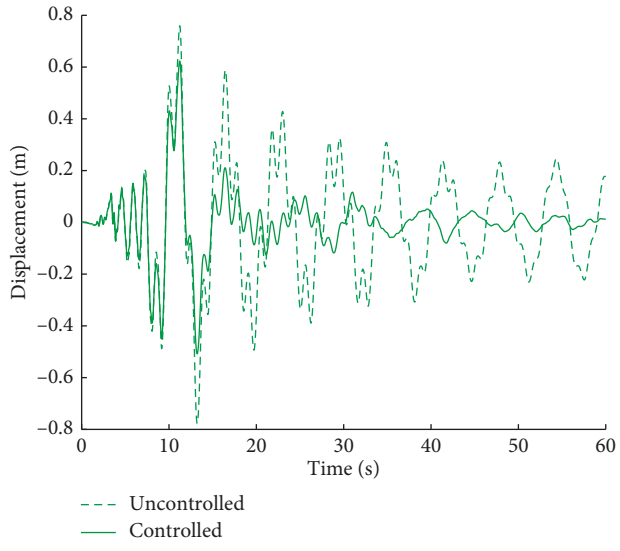

(a)

Story	m_0	β	ψ
76	2.28	1.03	36.27
74	0.72	1.03	36.39

(b)

J_1	J_2	J_3
0.80	0.84	0.97

(c)

Figure 17: Uncontrolled/controlled responses under the San Fernando earthquake. (a) Roof displacement response. (b) TMD specifications. (c) Objective values.

Table 8: Comparison between controlled and uncontrolled drifts and absolute accelerations of the top story for different earthquake excitations.

Earthquake	Max. drift (uncontrolled)	Max. drift (controlled)	Max. absolute acceleration (uncontrolled, m/s^2)	Max. absolute acceleration (controlled, m/s^2)
Bam	0.0184	0.0172	34.94	17.32
El Centro	0.0128	0.0111	20.99	16.11
Kobe	0.0079	0.0066	25.72	21.40
Manjil	0.0159	0.0074	28.51	9.30
Northridge	0.0178	0.0146	23.87	15.55
Landers	0.0282	0.0262	28.94	14.79
San Fernando	0.0092	0.0075	21.61	12.35

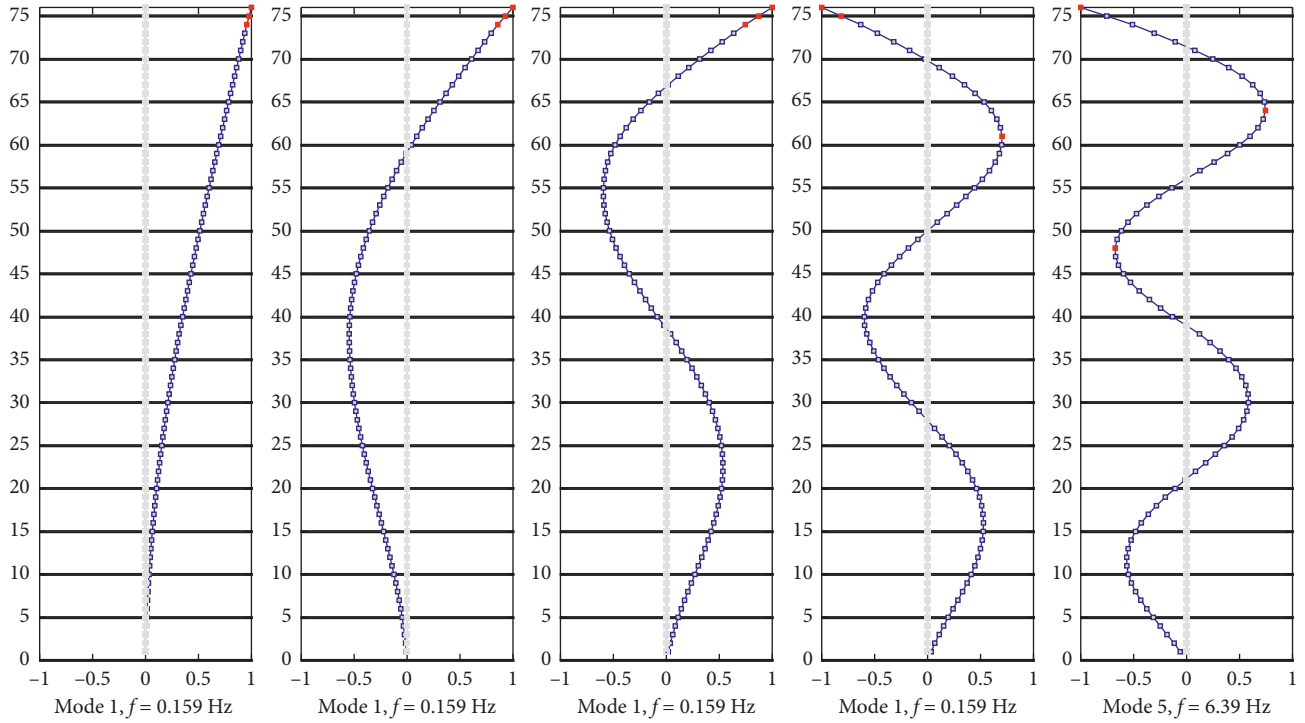

Figure 18: Three stories with maximum modal displacements in the first five natural modes.

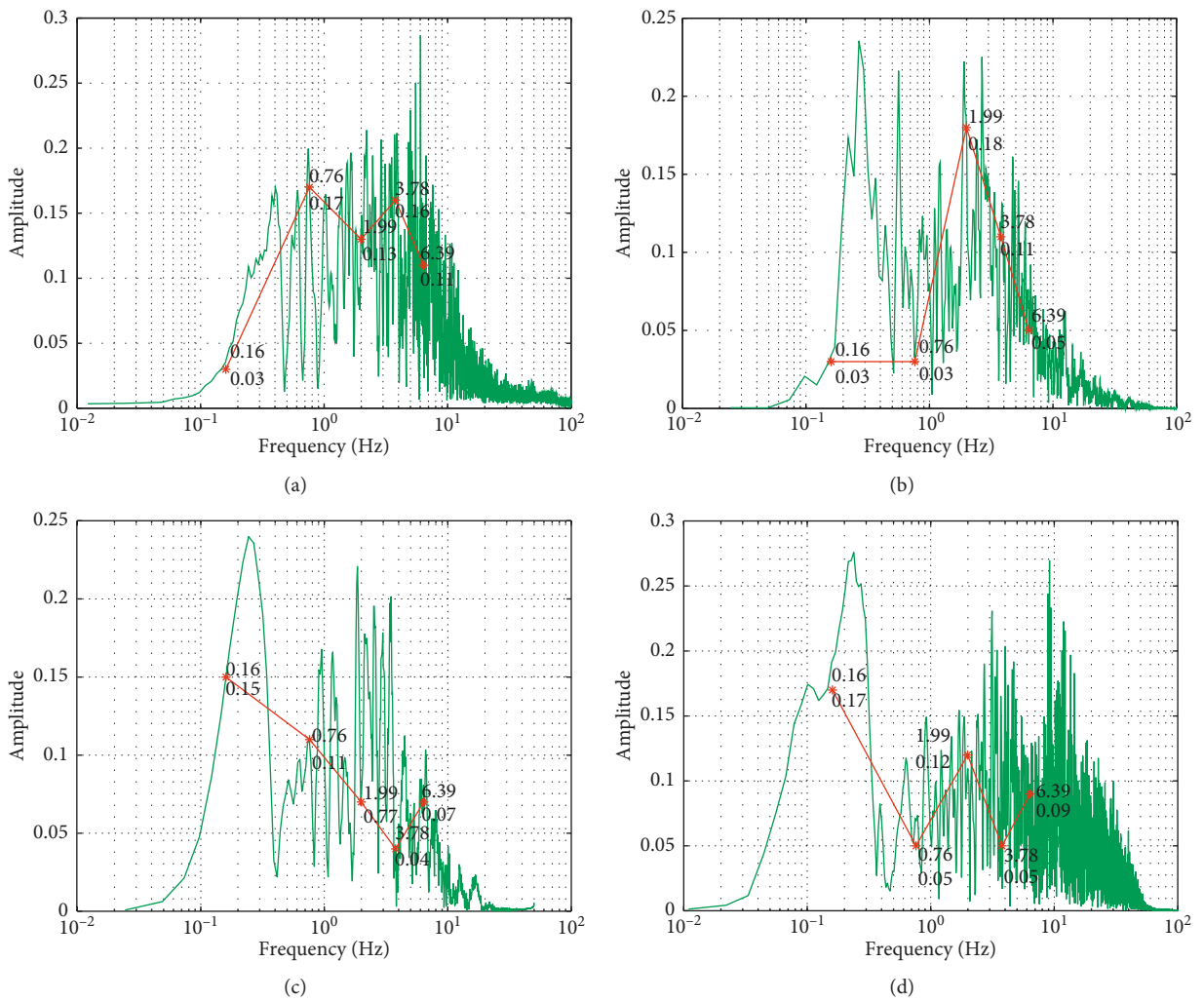

Figure 19: Continued.

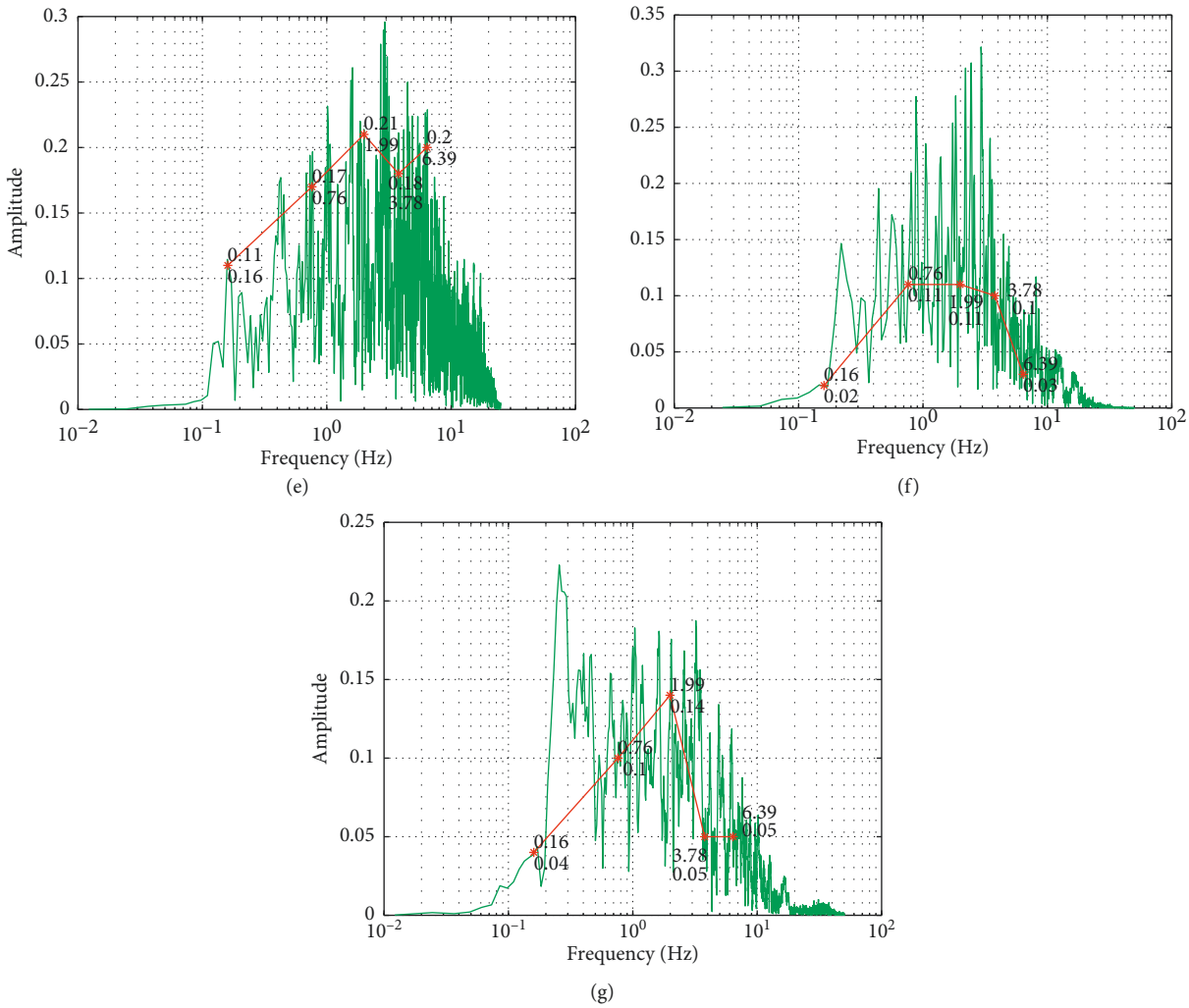

Figure 19: Fourier transform of earthquake excitations. (a) Bam. (b) El Centro. (c) Kobe. (d) Landers. (e) Manjil. (f) Northridge. (g) San Fernando.

(3) The optimum parameters for the TMDs that control the vibrations in the lower modes include the maximum allowed damping ratio. This indicates that increasing the damping ratio would improve the performance of such TMDs.

(4) The results showed that the performance of the TMDs was not good in reducing the initial maximums in displacement responses compared to their reduction of the later maximums that occurred after some initial oscillations.

(5) Even in the cases with immediate maximum displacement responses, the MTMD system significantly improves the damping.

Data Availability

The data used to support the findings of this study are available from the corresponding author upon request.

Conflicts of Interest

The authors declare that they have no conflicts of interest.

References

[1] M. M. Ali and K. S. Moon, "Structural developments in tall buildings: current trends and future prospects," *Architectural Science Review*, vol. 50, no. 3, pp. 205–223, 2007.

[2] B. F. Spencer and M. K. Sain, "Controlling buildings: a new frontier in feedback," *IEEE Control Systems Magazine*, vol. 17, no. 6, pp. 19–35, 1997.

[3] T. T. Soong and B. F. Spencer, "Supplemental energy dissipation: state-of-the-art and state-of-the-practice," *Engineering Structures*, vol. 24, no. 3, pp. 243–259, 2002.

[4] S. J. Moon, L. A. Bergman, and P. G. Voulgaris, "Sliding mode control of cable-stayed bridge subjected to seismic excitation," *Journal of Engineering Mechanics*, vol. 129, no. 1, pp. 71–78, 2003.

[5] J. F. Wang, C. C. Lin, and B. L. Chen, "Vibration suppression for high-speed railway bridges using tuned mass dampers," *International Journal of Solids and Structures*, vol. 40, no. 2, pp. 465–491, 2003.

[6] Y. Arfiadi and M. N. S. Hadi, "Optimum placement and properties of tuned mass dampers using hybrid genetic algorithms," *International Journal of Optimization in Civil Engineering*, vol. 1, no. 1, pp. 167–187, 2011.

[7] A. Y. T. Leung and H. Zhang, "Particle swarm optimization of tuned mass dampers," *Engineering Structures*, vol. 31, no. 3, pp. 715–728, 2009.
[8] G. Chen and J. Wu, "Optimal placement of multiple tune mass dampers for seismic structures," *Journal of Structural Engineering*, vol. 127, no. 9, pp. 1054–1062, 2001.
[9] S. Elias and V. Matsagar, "Distributed multiple tuned mass dampers for wind vibration response control of high-rise building," *Journal of Engineering*, vol. 2014, Article ID 198719, 11 pages, 2014.
[10] C.-L. Lee, Y.-T. Chen, L.-L. Chung, and Y.-P. Wang, "Optimal design theories and applications of tuned mass dampers," *Engineering Structures*, vol. 28, no. 1, pp. 43–53, 2006.
[11] C. Li and B. Zhu, "Estimating double tuned mass dampers for structures under ground acceleration using a novel optimum criterion," *Journal of Sound and Vibration*, vol. 298, no. 1-2, pp. 280–297, 2006.
[12] R. N. Jabary and S. P. G. Madabhushi, "Tuned mass damper effects on the response of multi-storied structures observed in geotechnical centrifuge tests," *Soil Dynamics and Earthquake Engineering*, vol. 77, pp. 373–380, 2015.
[13] H.-C. Tsai and G.-C. Lin, "Optimum tuned-mass dampers for minimizing steady-state response of support-excited and damped systems," *Earthquake Engineering & Structural Dynamics*, vol. 22, no. 11, pp. 957–973, 1993.
[14] Y. L. Xu, J. Chen, C. L. Ng, and W. L. Qu, "Semiactive seismic response control of buildings with podium structure," *Journal of Structural Engineering*, vol. 131, no. 6, pp. 890–899, 2005.
[15] T. A. Sakr, "Vibration control of buildings by using partial floor loads as multiple tuned mass dampers," *HBRC Journal*, vol. 13, no. 2, pp. 133–144, 2017.
[16] L. Zuo and S. A. Nayfeh, "Optimization of the individual stiffness and damping parameters in multiple-tuned-mass-damper systems," *Journal of Vibration and Acoustics*, vol. 127, no. 1, p. 77, 2005.
[17] N. Hoang and P. Warnitchai, "Design of multiple tuned mass dampers by using a numerical optimizer," *Earthquake Engineering & Structural Dynamics*, vol. 34, no. 2, pp. 125–144, 2005.
[18] M. Jokic, M. Stegic, and M. Butkovic, "Reduced-order multiple tuned mass damper optimization: a bounded real lemma for descriptor systems approach," *Journal of Sound and Vibration*, vol. 330, no. 22, pp. 5259–5268, 2011.
[19] A. Y. Pisal and R. S. Jangid, "Seismic response of multi-story structure with multiple tuned mass friction dampers," *International Journal of Advanced Structural Engineering*, vol. 6, no. 1, pp. 1–13, 2014.
[20] C. Li and W. Qu, "Optimum properties of multiple tuned mass dampers for reduction of translational and torsional response of structures subject to ground acceleration," *Engineering Structures*, vol. 28, no. 4, pp. 472–494, 2006.
[21] "Tallest 10 completed buildings with dampers," *CTBUH Journal*, vol. 48, no. 3, 2018, https://www.google.com/url?sa=t&rct=j&q=&esrc=s&source=web&cd=1&cad=rja&uact=8&ved=2ahUKEwiZv-L82JvkAhXKI1AKHbMDBIwQFjAAegQIABAC&url=http%3A%2F%2Fglobal.ctbuh.org%2Fpaper%2F3788&usg=AOvVaw2F_KHUsmgWNYnY_pgGXE1f.
[22] C. C. Chang and W. L. Qu, "Unified dynamic absorber design formulas for wind-induced vibration control of tall buildings," *The Structural Design of Tall Buildings*, vol. 7, no. 2, pp. 147–166, 1998.
[23] S. N. Deshmukh and N. K. Chandiramani, "LQR control of wind excited benchmark building using variable stiffness tuned mass damper," *Shock and Vibration*, vol. 2014, Article ID 156523, 12 pages, 2014.
[24] S. Pourzeynali, S. Salimi, and H. E. Kalesar, "Robust multi-objective optimization design of TMD control device to reduce tall building responses against earthquake excitations using genetic algorithms," *Scientia Iranica*, vol. 20, no. 2, pp. 207–221, 2013.
[25] S. Elias, V. Matsagar, and T. K. Datta, "Effectiveness of distributed tuned mass dampers for multi-mode control of chimney under earthquakes," *Engineering Structures*, vol. 124, pp. 1–16, 2016.
[26] S. Elias and V. Matsagar, "Research developments in vibration control of structures using passive tuned mass dampers," *Annual Reviews in Control*, vol. 44, pp. 129–156, 2017.
[27] N. M. Newmark, "A method of computation for structural dynamics," *Journal of the Engineering Mechanics Division*, vol. 85, no. 3, pp. 67–94, 1959.
[28] K. Deb, A. Pratap, S. Agarwal, and T. Meyarivan, "A fast and elitist multiobjective genetic algorithm: NSGA-II," *IEEE Transactions on Evolutionary Computation*, vol. 6, no. 2, pp. 182–197, 2002.
[29] O. Kramer, *Genetic Algorithm Essentials*, Springer Publishing Company, New York, NY, USA, 1st edition, 2017.
[30] D. E. Goldberg and K. Deb, "A comparative analysis of selection schemes used in genetic algorithms," *Foundations of Genetic Algorithms*, vol. 1, pp. 69–93, 1991.
[31] PEER Center, *PEER Ground Motion Database*, PEER Center, University of California, Berkeley, CA, USA, https://ngawest2.berkeley.edu/.
[32] I. Iervolino, C. Galasso, and E. Cosenza, "REXEL: computer aided record selection for code-based seismic structural analysis," *Bulletin of Earthquake Engineering*, vol. 8, no. 2, pp. 339–362, 2010.
[33] F. Weber, J. Distl, L. Meier, and C. Braun, "Curved surface sliders with friction damping, linear viscous damping, bow tie friction damping, and semiactively controlled properties," *Structural Control and Health Monitoring*, vol. 25, no. 11, p. e2257, 2018.
[34] M. Gen and R. Cheng, *Genetic Algorithms and Engineering Optimization*, John Wiley & Sons, Hoboken, NJ, USA, 2000.

Hindawi
Advances in Civil Engineering
Volume 2019, Article ID 1396019, 16 pages
https://doi.org/10.1155/2019/1396019

Research Article

Accuracy Assessment of Nonlinear Seismic Displacement Demand Predicted by Simplified Methods for the Plateau Range of Design Response Spectra

Pierino Lestuzzi[1] **and Lorenzo Diana**[1,2]

[1]*EPFL-ENAC-IIC-IMAC, Lausanne, Switzerland*
[2]*DICEA, Università degli studi di Napoli Federico II, Naples, Italy*

Correspondence should be addressed to Pierino Lestuzzi; pierino.lestuzzi@epfl.ch

Received 28 February 2019; Accepted 9 August 2019; Published 19 September 2019

Guest Editor: Francisco López Almansa

The nonlinear seismic displacement demand prediction for low-period structures, i.e., with an initial fundamental period situated in the plateau of design response spectra, is studied. In Eurocode 8, the computation of seismic displacement demands is essentially based on a simplified method called the N2 method. Alternative approaches using linear computation with increased damping ratio are common in other parts of the world. The accuracy of three methods for seismic displacement demand prediction is carefully examined for the plateau range of Type-1 soil class response spectra of Eurocode 8. The accuracy is assessed through comparing the displacement demand computed using nonlinear time-history analysis (NLTHA) with predictions using simplified methods. The N2 method, a recently proposed optimization of the N2 method, and the Lin and Miranda method are compared. Nonlinear single-degree-of-freedom systems are subjected to several sets of recorded earthquakes that are modified to match design response spectra prescribed by Eurocode 8. The shape of Eurocode 8 response spectra after the plateau is defined by a constant pseudovelocity range ($1/T$). However, the slope of this declining branch may be specified using precise spectral microzonation investigation. However, the N2 method has been found to be particularly inaccurate with certain microzonation response spectra that are characterized by a gently decreasing branch after the plateau. The present study investigates the impact of the slope of the decreasing branch after the plateau of response spectra on the accuracy of displacement demand predictions. The results show that the accuracy domain of the N2 method is restricted to strength reduction factor values around 3.5. Using the N2 method to predict displacement demands leads to significant overestimations for strength reduction factors smaller than 2.5 and to significant underestimations for strength reduction factors larger than 4. Fortunately, the optimized N2 method leads to accurate results for the whole range of strength reduction factors. For small values of strength reduction factors, up to 2.5, the optimized N2 method and the Lin and Miranda method both provide accurate displacement demand predictions. However, the accuracy of displacement demand prediction strongly depends on the shape of the response spectrum after the plateau. A gently decreasing branch after the plateau affects the accuracy of displacement demand predictions. A threshold value of 0.75 for the exponent of the decreasing branch ($1/T^{\alpha}$) after the plateau is proposed. This issue should be considered for the ongoing developments of Eurocode 8.

1. Introduction

Structures do not remain elastic under extreme ground motions. Nonlinear behavior is therefore crucial in seismic response of structures. However, to avoid the use of more elaborated analyses that are suitable for strategic buildings only, structural-engineering approaches are generally based on simplified methods to determine seismic actions. The prediction of nonlinear seismic demand using linear elastic behavior for the determination of peak nonlinear response is widely used for seismic design as well as for vulnerability assessment. Existing methods involve either a linear

response based on initial period and damping ratio, eventually corrected with factors, or a linear response based on increased equivalent period and damping ratio.

It is well established that for medium-to-high period structures, the displacements of elastic and inelastic systems are approximately the same. This empirical finding known as the equal displacement rule (EDR) is nowadays widely used for seismic design purposes, e.g., in Eurocode 8 [1]. The basic assumption of the EDR is to predict the seismic performance of an inelastic system using the equivalent elastic system with the same initial period and damping coefficient. For low-period structures, the EDR loses its validity, since inelastic displacements are larger than elastic displacements. Other methods are therefore needed for this range of periods. The plateau range of the design spectra is particularly important since it provides the highest spectral acceleration. Furthermore, most buildings in Europe have less than 5 stories and thus have a natural period of less than 1 s. As a consequence, the natural period of a large part of the European building stock is located on the plateau of design spectra, i.e., out of the assumed standard range of application of the EDR. Reliable displacement demand predictions are therefore crucial for seismic vulnerability assessment of existing buildings. This is a key issue in vulnerability assessment at urban scale, where such displacement demand predictions are used for determining building damage using mechanical methods [2]. On the plateau of design spectra, Riddell et al. [3] and later Vidic et al. [4] proposed to compute the displacement demand based on a linear variation of the strength reduction factor as a function of the period. Alternative methods using equivalent damping approaches [5] were also developed and included in the design code in the US [6, 7].

The N2 method developed by Fajfar [8] is based on the equal displacement rule associated to a correction for the plateau range of the response spectrum. A simplified version of the N2 method was proposed in Eurocode 8 [1, 8]. This simplified version of the N2 method is investigated in this study. However, the lack of accuracy of the simplified version of the N2 method especially for low-period structures has already been pointed out by several research studies [9, 10]. In case of high-strength reduction factors, the simplified N2 method leads to unconservative results, since displacement demand predictions are underestimated with respect to nonlinear time-history analysis. By contrast, in case of low-strength reduction factors, displacement demand tends to be overestimated when using the simplified N2 method. Therefore, an optimized version of the simplified N2 method has recently been proposed in order to improve the reliability of displacement demand predictions [11]. The objective of this paper is to investigate the accuracy domain of the simplified N2 method and that of the optimized N2 method for displacement demand prediction in the plateau range of seismic design spectra. For comparison, the Lin and Miranda [5] method using equivalent period and damping ratio approaches is also investigated. The accuracy assessment is based on a comparison of the displacement demand computed using nonlinear time-history analysis (NLTHA) with the ones predicted by the three simplified methods.

2. Seismic Displacement Demand Prediction

The simplified version of the N2 method (according to Eurocode 8 and called "N2 method" in the following for simplicity), an optimized version of the simplified N2 method and the Lin and Miranda method are investigated in this study. These methods are briefly described in the following sections.

2.1. N2 Method. Since Veletsos and Newmark [12], it has been widely acknowledged that the displacements of elastic and inelastic systems are approximatively the same (Equal Displacement Rule, EDR). This empirical rule was confirmed by numerous numerical and experimental investigations (e.g., [13]) except for low-period structures, for which inelastic displacements are higher than elastic displacements. Another method is therefore needed to replace the EDR for the plateau period range, where EDR is no longer valid. The basic assumption of the EDR is to model an inelastic system using the equivalent elastic system with the same period and the same damping ratio. As illustrated in Figure 1(a), the EDR states that inelastic peak displacements (y_p) are approximately equal to elastic peak displacements (y_{el}) whatever the selected yield strength ($F_y = F_{el}/R$ or yield displacement $y_y = y_{el}/R$) of the structure. Note that when assuming the stiffness to be independent of the strength, the EDR leads to a strength reduction factor (R) equal to the global displacement ductility.

On the plateau period range of design spectra, Riddell et al. [3] and later Vidic et al. [4] proposed a linear variation of the strength reduction factor (R) as a function of the period (T) for a constant displacement ductility demand (μ), later used in EC8:

$$R = 1 + (\mu - 1)\frac{T}{T_0}. \tag{1}$$

In this assumption, the strength reduction factor (R) varies between 1 for a zero period and the value of the displacement ductility demand for the period T_0 being close to the end of the plateau, T_C. Based on equation (1), Fajfar has introduced the N2 method [8] by considering two domains, separated by the period T_0. Eurocode 8 includes a simplified version of the N2 method where the displacement demand is determined as follows:

$$\begin{cases} S_d = \dfrac{S_{de}}{R_\mu} \cdot \left[\left(R_\mu - 1 \right) \cdot \dfrac{T_C}{T} + 1 \right], & T < T_C \text{ and } R_\mu > 1, \\ S_d = S_{de}, & T \geq T_C \text{ or } R_\mu \leq 1, \end{cases} \tag{2}$$

where the parameters T_C, S_{de}, and S_{ae} are the corner period limiting the zone of the spectrum of maximum acceleration (i.e., plateau), the spectral displacement of the structure with an unlimited elastic behavior and the elastic spectral acceleration, respectively. These parameters define the seismic displacement demand (S_d). The period T (period of vibration of the structure) and the strength reduction factor R_μ

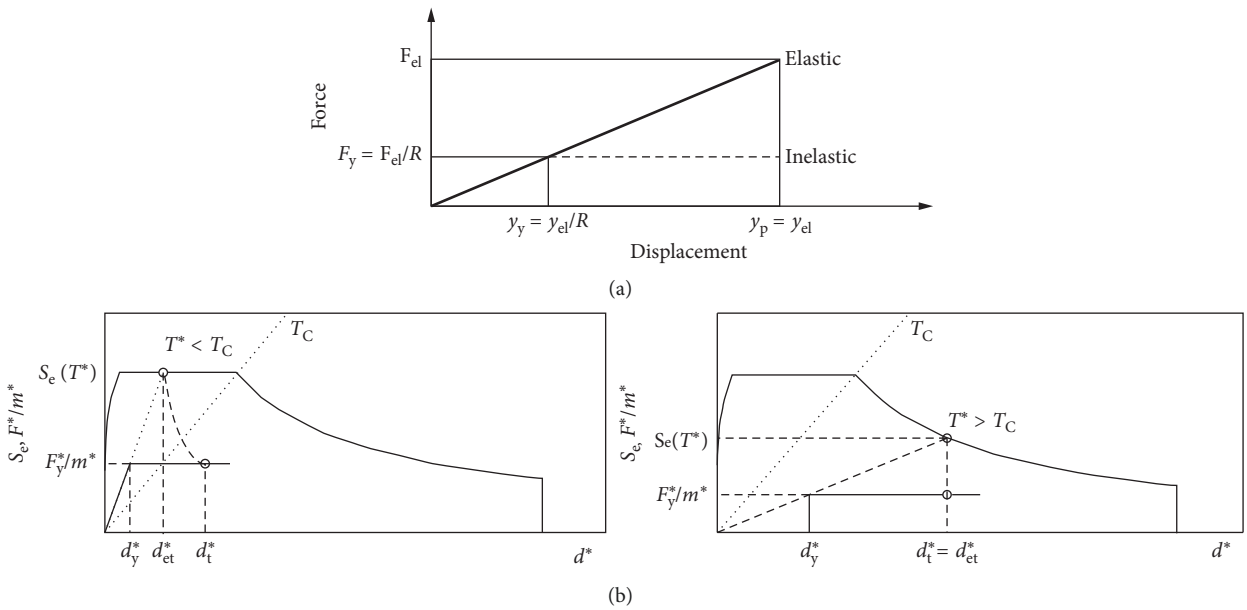

Figure 1: (a) Schematic description of the equal displacement rule (EDR). (b) ADRS representation of the nonlinear displacement demand according to EC8 (adapted from [1]).

($R_\mu = S_{ae}/S_{ay}$) are parameters defining building capacity. The value S_{ay} represents the yield acceleration of the structure.

2.2. Optimized N2 Method. The second method that is evaluated has been proposed by Diana et al. [11] and is based on an optimization of the original N2 method. An exponent correction to the classical N2 formulation has also been proposed by Graziotti et al. in 2014 [14], based on shaking-table tests; however, the correction is valid exclusively for stiff masonry structures. The proposal by Diana et al. [11] enhances the N2 method to include an additional exponent and multiplicative coefficients for correction. The new formula has been obtained by a global optimization meta-heuristic employing a genetic algorithm to minimize differences between the formula and the NLTHA. The approach of the optimized N2 method preserves the mathematical compatibility with the previous N2 method. The formula is defined starting from (2), including three coefficients, as follows:

$$\begin{cases} S_d = \dfrac{S_{de}}{R_\mu/1.48} \cdot \left[\left(\dfrac{R_\mu}{1.45} - 1\right)^{1.35} \cdot \dfrac{T_C}{T} + 1\right], & T < T_C \text{ and } R_\mu > 1, \\ S_d = S_{de}, & T \geq T_C \text{ or } R_\mu \leq 1. \end{cases} \tag{3}$$

At the end of the plateau, for periods close to T_C, the nonlinear displacement demand according to (3) may lead to values that diverge notably from the EDR. The compatibility with EDR in T_C is nevertheless necessary because EDR is valid after the plateau of the design spectrum, according to EC8. This drawback does not appear with the N2 method (see equation (2)). This is due to the introduction of three coefficients in (3). In order to avoid such a discrepancy in the period range at the end of the plateau of the response spectrum (i.e., for periods close to T_C), the displacement demand is limited by an additional condition based on a relationship proposed by Michel et al. [10]. Figure 2 shows the relationship (proposition 2) which corresponds to a linear variation of the displacement demand with respect to the period (T). The prolongation of the EDR for the period range of the plateau corresponds to a linear variation (proposition 1 in Figure 2). Proposition 2 keeps the linear variation but with an initial value of one third of the spectral displacement at the end of the plateau. This linear relationship (proposition 2) was found to lead to adequate upper bound values of the displacement demand for large values of strength reduction factors [10]. According to proposition 2, the displacement demand is computed as follows:

$$S_d = S_d(T_C) \cdot \left[\frac{T}{T_C} \cdot \frac{2}{3} + \frac{1}{3}\right]. \tag{4}$$

With the optimized N2 method, the smaller value of (3) and (4) is considered as the displacement demand prediction for the period range of the plateau of the corresponding design spectrum (between T_B and T_C).

2.3. Lin and Miranda Method. The Lin and Miranda method (2008) is based on equivalent linearization. The displacement demand of a nonlinear single-degree-of-freedom (SDOF) system is calculated considering the displacement demand of an equivalent linear-elastic SDOF system having a period and a damping ratio higher than those of the initial nonlinear system [7]. Therefore, the inelastic displacement demand of the nonlinear SDOF system is determined as

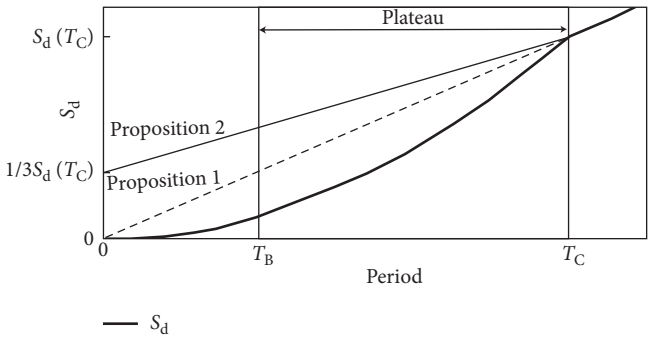

Figure 2: A linear relationship of the displacement demand with respect to the period (proposition 2) is used as a limitation of the displacement demand prediction in the period range close to the end of the plateau (i.e., for periods shorter but close to T_C) [10].

$$S_d = S_d\left(T_{eq}; \xi_{eq}\right) = S_d\left(T_{eq}; \xi_{=5\%}\right) \cdot \eta = S_a\left(T_{eq}; \xi_{=5\%}\right) \cdot \frac{T_{eq}^2}{4\pi^2} \cdot \eta, \tag{5}$$

where $S_d(T_{eq}; \xi_{eq})$ is the spectral displacement demand of the equivalent system, T_{eq} is the equivalent period of vibration of the equivalent system; ξ_{eq} is the equivalent viscous damping ratio, $S_d(T_{eq}; \xi_{=5\%})$ is the displacement demand of the linear system with 5% damping elastic ratio, and η is a reduction factor depending from the damping ratio ξ. The reduction factor η can be determined as (numerical value to be used for ξ_{eq}, not in "%")

$$\eta = \sqrt{\frac{1}{0.5 + 10\,\xi_{eq}}}. \tag{6}$$

The equivalent period T_{eq} and the equivalent damping ratio ξ_{eq} depend on the strength reduction factor R_μ of the nonlinear SDOF system and on the initial period of vibration and damping ratio, respectively. Several equivalent linear methods exist in literature that differ mainly for the functions used to compute T_{eq} and ξ_{eq} (e.g., Iwan [15]; Miranda and Ruiz-García [16]; Sullivan et al. [17]).

In their work (2008), Lin and Miranda give the equivalent period and the equivalent damping ratio as follows:

$$T_{eq} = \left[1 + \frac{m_1}{T^{m2}} \cdot \left(R_\mu^{1.8} - 1\right)\right] \cdot T,$$
$$\xi_{eq} = \xi_{=5\%} + \frac{n_1}{T^{n_2}} \cdot \left(R_\mu - 1\right). \tag{7}$$

Coefficients m_1, m_2, n_1, and n_2 depend on the postyield stiffness ratio α (Table 1), R_μ and T are, respectively, the strength reduction factor and the initial period of vibration of the nonlinear SDOF and $\xi_{=5\%}$ is the 5% damping elastic ratio.

3. NLTHA Methodology

The methodology used in this study for the nonlinear time-history analysis (NLTHA) is similar to the one proposed in previous investigations [2, 10]. Nonlinear responses of SDOF systems exposed to acceleration time-histories are computed and the difference between the obtained peak displacement demands and those predicted by the various simplified methods is calculated. The nonlinear structural behavior is described by the popular modified Takeda hysteretic model. For each design spectrum, a set of 12 recordings is first selected from a database, such as the European Strong Motion Database [19], and slightly modified to match the corresponding response spectrum.

Table 1: Coefficients for calculating equivalent period and damping [18].

α (%)	m_1	m_2	n_1	n_2
0	0.026	0.87	0.016	0.84
5	0.027	0.65	0.027	0.55
10	0.027	0.51	0.031	0.39
20	0.024	0.36	0.030	0.24

3.1. Design Response Spectra. Response spectra according to the soil classes of Eurocode 8 [1] are tested in this study. More specifically, soil classes A, B, C, and D are used. The values of the parameters for the Type 1 defined by EC8 are shown in Figure 3. The values of the corner periods T_B to T_C delimiting the plateau region of response spectra depend on soil classes. The shape after the plateau is defined by a constant pseudovelocity range ($1/T$, from corner period T_C to period T_D) followed by a constant relative displacement range ($1/T^2$ after T_D). Additionally, some response spectra resulting from spectral microzonation studies in Switzerland are also considered in the analysis. Microzone response spectra considered in this study are those of the towns of Yverdon, Sion, and Martigny. In detail, microzone spectra considered are S2, S3, and S4 for Yverdon, A1, A2, and A3 for Sion, and M3 for Martigny. The response spectra specified for the considered microzones in Yverdon [20] are plotted in Figure 3. Figure 4 shows the response spectra specified for the six microzones in Sion and Martigny ([21]).

The plateau acceleration level of the response spectrum for microzone S2 is higher and that for microzone S4 is lower than the ones of EC8. Furthermore, the shapes after the plateau diverge from the ones of EC8 response spectra. The response spectrum for microzone S2 has an exponent of the declining branch after the plateau of $\alpha = 1.6$ and that for microzone S4 has an exponent of $\alpha = 0.74$. The response spectrum for microzones S3 and S3 mod has a shape that is compatible with EC8, which is characterized by a constant pseudovelocity range ($1/T$) after the plateau.

The plateau acceleration level of the response spectra of microzones A1, A2, and A3 corresponds to the one of EC8 soil class A, C, and D respectively. However, plateau corners of the response spectra of microzones A1 and A2 are modified towards higher periods. These modifications are related to increased seismic demands with respect to the ones of corresponding soil classes defined in EC8. Plateau acceleration levels of the response spectra of microzones M1 and M3 of Martigny are higher than those of Sion. The response spectrum of microzone M1 is huge and thus related to a larger seismic demand. Except for the low-period range,

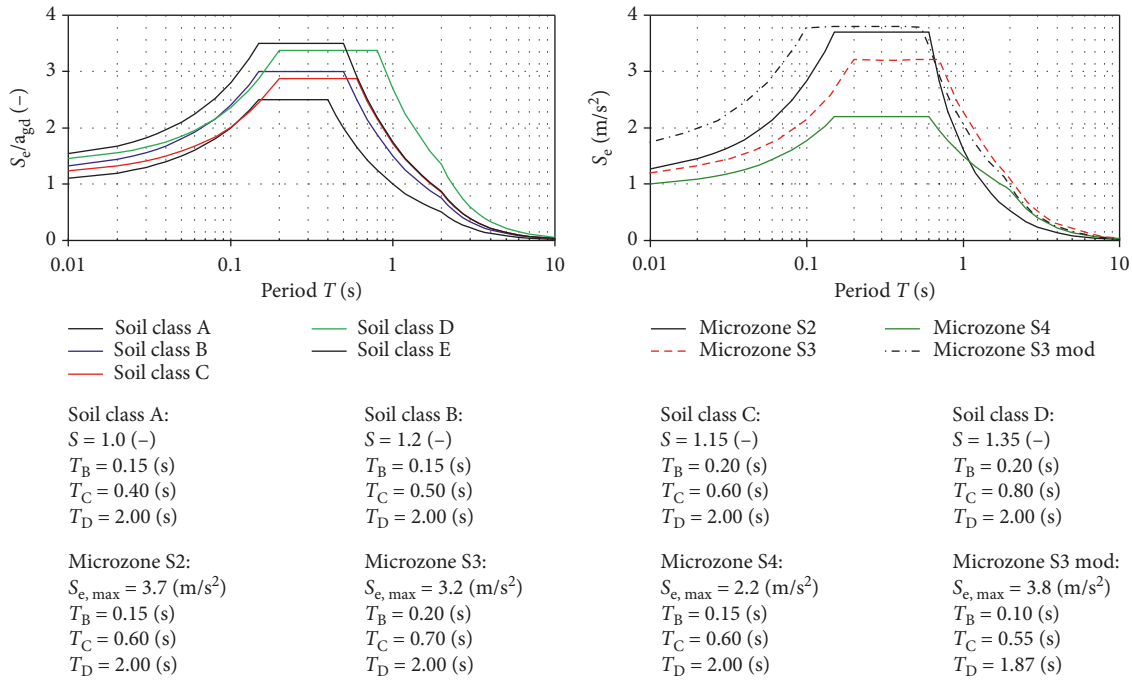

Figure 3: Eurocode 8: elastic response spectra for 5% damping ratio related to the soil classes A to E microzonation of Yverdon: elastic response spectra for a return period of 475 years and 5% damping ratio related to the four microzones S2, S3, S4, and S3 mod, respectively.

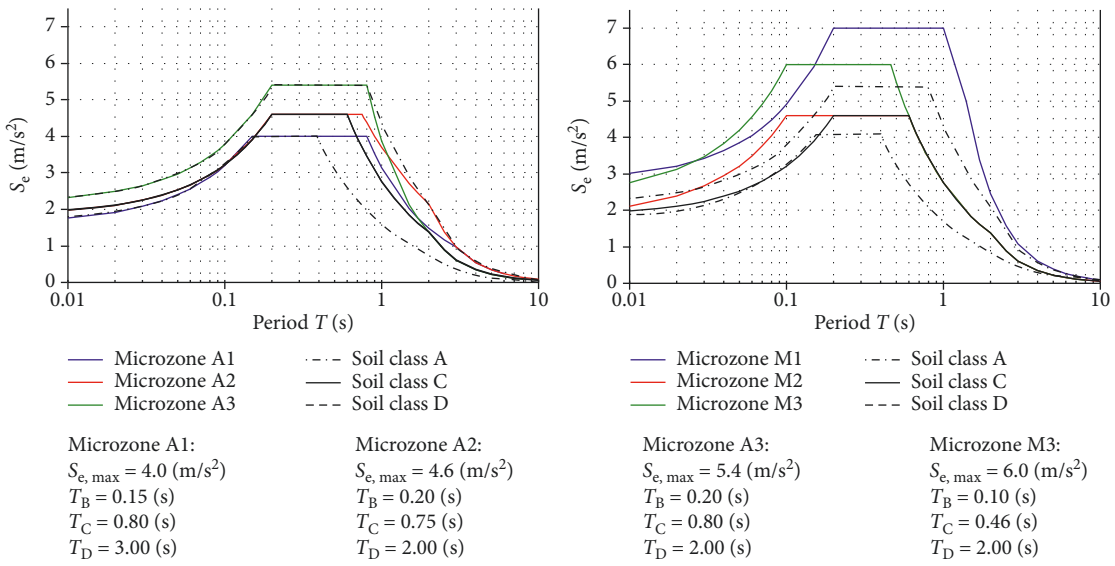

Figure 4: Microzonation of Sion and Martigny: elastic response spectra for a return period of 475 years and 5% damping ratio related the six microzones A1, A2, and A3, respectively, M1, M2, and M3 ([21]).

the response spectrum of microzone M2 is in accordance with the response spectrum of soil class C. The upper corner period of response spectrum of microzone M3 is situated between the ones of EC8 soil class A and B.

3.2. Selection and Modification of Ground-Motion Recordings. Recordings are selected in order to match the considered response spectrum (target spectrum). Through a ranking process of the recordings of the database following the difference between their response spectrum and the target spectrum, recordings are ordered. The twelve highest ranked recordings form the recording set related to the considered target response spectrum. This selection is based on structural-engineering considerations only. As a consequence, earthquakes with different seismological features, such as magnitude or epicentral distance, are incorporated into the dataset. The main objective is to perform a statistical study of the nonlinear response of a structure undergoing any acceleration recording. Therefore, uncertainties related to recordings are not considered.

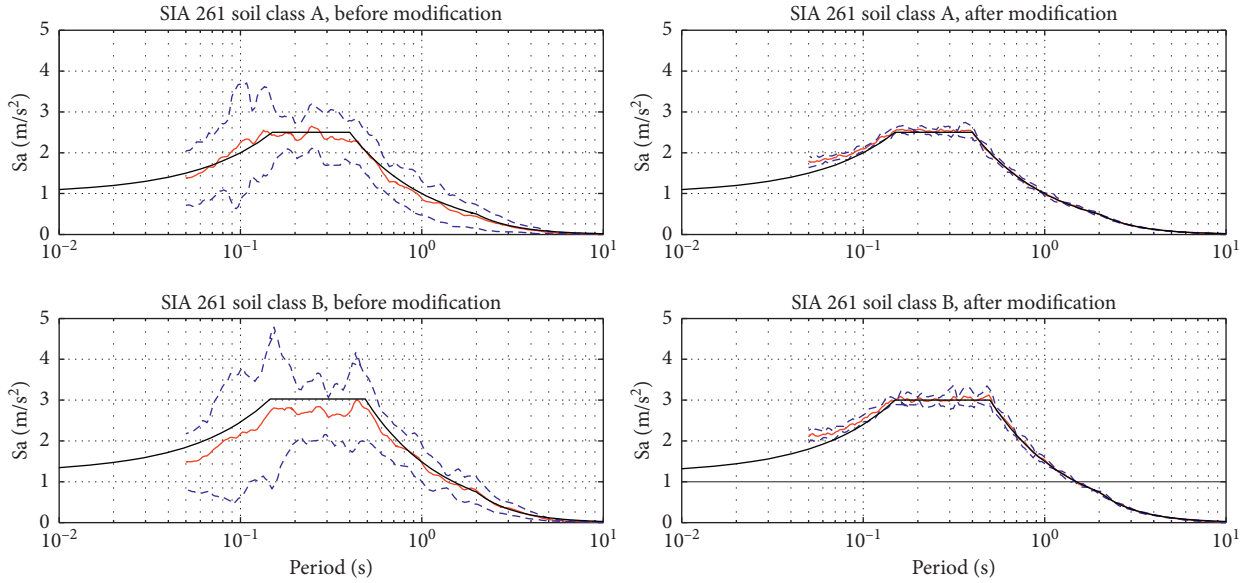

Figure 5: Statistical characteristics of the response spectra for the sets of the twelve recordings selected for the best fit to the response spectrum of the soil classes A and B of Eurocode 8 before (left) and after (right) modification for matching target spectrum.

The selected recordings are modified afterwards with the nonstationary spectral matching method of Abrahamson [22] in order to match the target spectrum individually. This technique has the decisive advantage to involve small modifications of the recordings, and thus, it is ensured that the related structural response in the nonlinear domain is not significantly affected. Therefore, this procedure allows the removal of the variability due to ground motion in order to evaluate exclusively the variability due to the estimation of the structural response. As shown by statistical characteristics of response spectra for the sets of twelve recordings before and after modification, the process repeated over ten iterations is very efficient for matching target spectra. As an example, response spectrum average and mean values plus and minus one standard deviation are plotted in Figure 5 for soil classes A and B of EC8. Figure 5 shows that the selection performed on the twelve recordings for each set leads already to a good match with respect to mean values. The plots after modification using the technique of Abrahamson show improvement in matching the target spectrum, as well as significant reduction in the variability.

3.3. Hysteretic Model. The nonlinear SDOF systems involved in this study are defined by their initial natural period, T (corresponding to the initial stiffness of SDOF), the yield displacement, and the hysteretic model according to which the structure behaves in the nonlinear range. The modified Takeda model is used as a hysteretic model to compute the nonlinear responses because it provides an adequate simulation of the behavior of materials such as reinforced concrete. However, as already reported in other studies (e.g., [23, 24]) the results obtained by using other models, such as the Q-model [25] or the Gamma model [26], would be similar and would not alter the conclusions presented within this work.

The Takeda model has been proposed in an original version by Takeda et al. [27]. The modified Takeda model has been developed independently by Otani [28] and Litton [29] and adapted by many researchers later on. The version of Allahabadi and Powell [30] is used hereafter. The force-displacement relationship, plotted in Figure 6, is specified through five parameters: the initial stiffness, the yield displacement, the postyield stiffness, a parameter governing the stiffness degradation (α), and a parameter (β) specifying the target for the reloading curve. In order to simulate the behavior of conventional structures, appropriate values of the parameters ($\alpha = 0.4$ and $\beta = 0.0$) are used in all analyses. A value of 5% has been selected for the hardening coefficient (postyield stiffness).

3.4. Computation. The methodology applied in this paper is schematically described in Figure 7. Simulations are performed for 18 values of the period, T, taken between 0.15 and 1 s and 12 instances of strength reduction factor, R, between 1.5 and 5. The typical value for the initial damping ratio ξ is set to 5%. Note that performing the computations with the strength reduction factor as a variable has the advantage that the level of the plateau is removed from the parameters. This approach provides a normalization of the results with respect to the plateau level. Furthermore, using a constant value for strength reduction factor (R) instead of a constant ductility (μ) ensures the same level of nonlinearity for each ground motion.

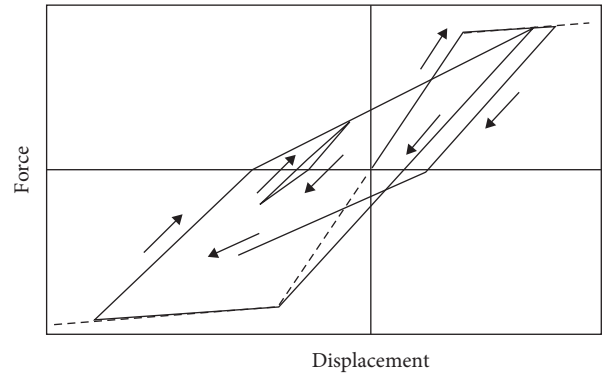

Figure 6: Force-displacement relationship defining the modified Takeda hysteretic model.

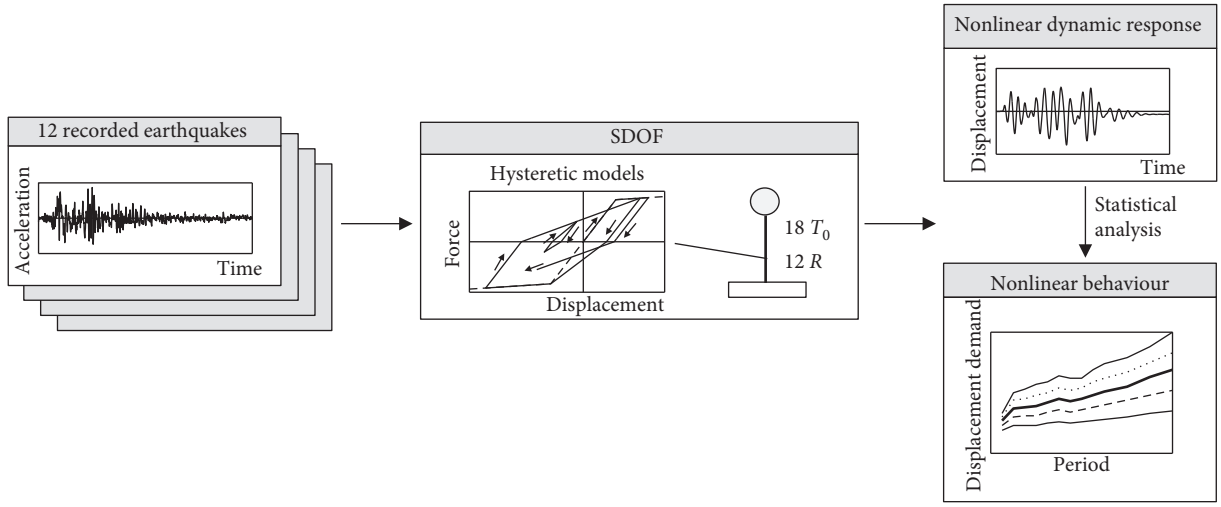

Figure 7: Schematic description of the methodology used for the investigations.

4. Results

The computed nonlinear displacement demands are assessed statistically by considering the average of the peak displacements (NLTHA displacement demand) obtained for the set of twelve ground motions corresponding to the considered response spectrum. The assessment is focused on the plateau of the considered response spectrum, i.e., only the values of the periods between the corner periods T_B and T_C are taken into account. The accuracy of the three methods (the N2 method, the optimized N2 method, and the Lin and Miranda method) is then first qualitatively calculated using the ratio of displacement demand prediction to NLTHA displacement demand for the 12 strength reduction factors. To account for the distribution of the nonlinear responses, threshold limits for a certain range around the value of 1 should be defined. As overestimation of the displacement demand is less problematic than underestimation, the threshold limits are not considered symmetrically. Consequently, underestimation by 10% and overestimation by 15% are defined as acceptable. Therefore, the method may be considered as accurate if the ratios remain within the thresholds of 90% and 115% along the plateau range. Moreover, in order to avoid threshold effects, up to two values outside the defined limits are allowed. As an example, Figures 8–10 show the statistical results for the EC8 response spectrum for soil classes A, B, and D, respectively. The results for four selected values of the strength reduction factor are plotted. The results that are shown are typical of the performed study. For soil class A, the corner periods delimiting the plateau of the response spectrum are $T_B = 0.15$ s and $T_C = 0.4$ s. The plots on Figure 8 for $R = 2$, 3, 4, and 5 show that the N2 method is only accurate for a single value of the strength reduction factor, namely, $R = 3$.

For soil class B, the corner periods delimiting the response spectrum plateau are $T_B = 0.15$ s and $T_C = 0.5$ s. The plots in Figure 9 for $R = 1.5$, 2.5, 3.5, and 4.5 show that the N2 method is only accurate for the single value of the strength reduction factor of $R = 3.5$. Displacement demand is systematically overestimated for small values of R and underestimated for high values of R, especially for the very short period range (beginning of the plateau). By contrast, the optimized N2 method is accurate for all R values. The Lin and Miranda method is accurate for small values of the strength reduction factor up to $R = 2.5$ while displacement demand is systematically overestimated for higher values of R.

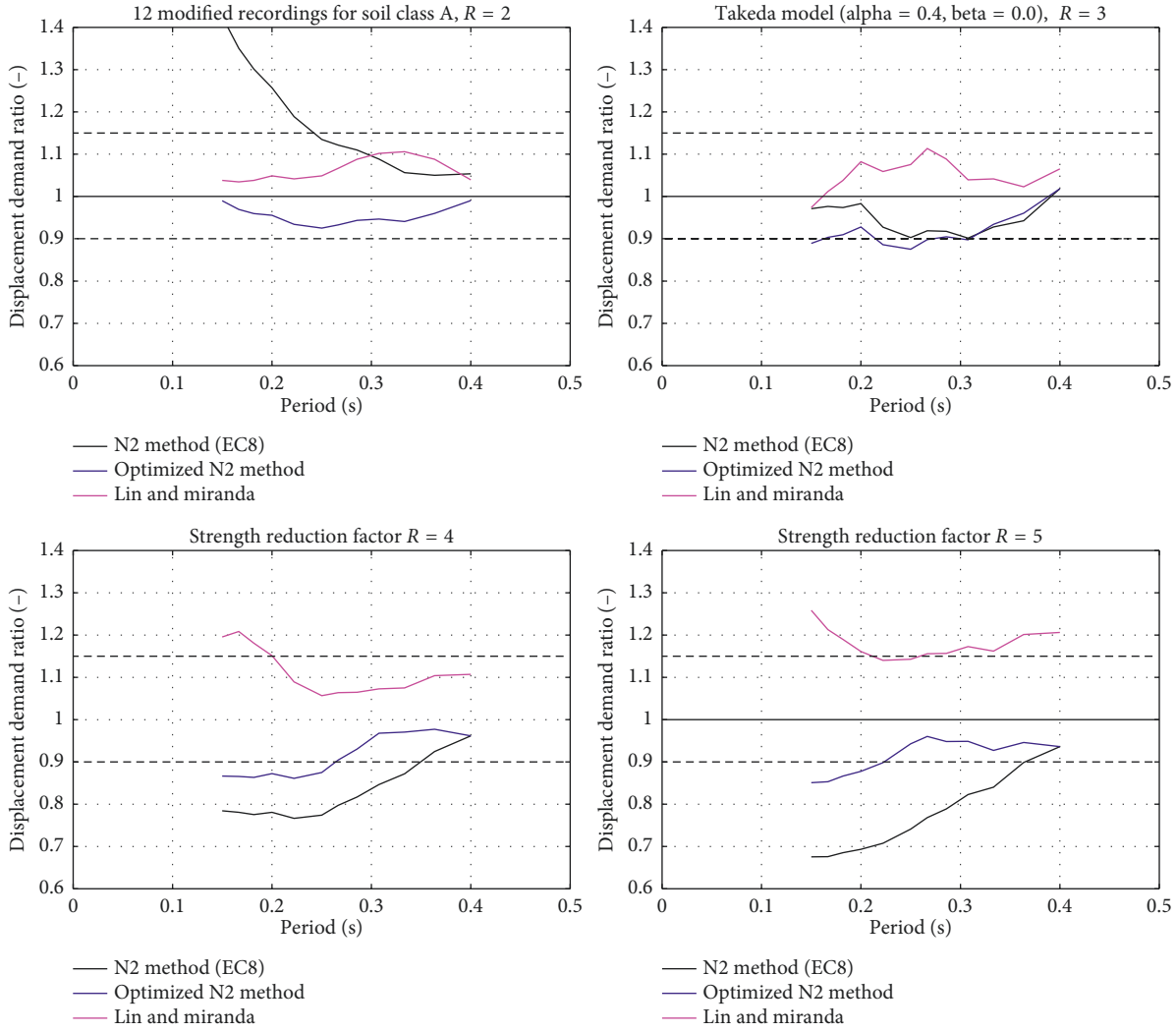

Figure 8: Assessment of the nonlinear displacement demands for soil class A and four values of strength reduction factors, $R = 1$ to $R = 5$. The ratio of predicted to actual (NLTHA) displacement demand is plotted with respect to the period. The plateau period range of the corresponding response spectrum (0.15 s to 0.40 s) is considered for the assessment.

For soil class D, the corner periods delimiting the response spectrum plateau are $T_B = 0.2$ s and $T_C = 0.8$ s. The plots in Figure 10 for $R = 2.25$, 2.75, 3.25, and 3.75 show that the N2 method may be considered as accurate for $R = 3.25$ and relatively accurate for $R = 3.75$. Again, the optimized N2 method is accurate for all R values. By contrast, the Lin and Miranda method may be considered as accurate only for the value of $R = 2.25$. For the other values of R, the inaccuracy of the Lin and Miranda method is essentially due to underestimations of displacement demands for the very beginning of the plateau, i.e., for periods close to T_B, as shown by plots in Figure 10.

4.1. Results for Eurocode 8 and Microzonation Response Spectra. The assessment procedure described above is performed for response spectra-related soil classes of Eurocode 8, from A to D, and for few response spectra of detailed microzonation studies (M3, S3, and S3 modified). The accuracy of the three simplified methods is then quantitatively assessed using the relative ratio of displacement demand prediction to NLTHA displacement demand ($|\Delta|_{Ti}$) for the different strength reduction factors. According to Diana et al. [11], the global average discrepancy value is used to assess the accuracy of the methods for the plateau period range for each analyzed strength reduction factor. The global average discrepancy is defined as follows:

$$\overline{|\Delta|}_R = \frac{1}{t}\sum_{i=1}^{t} |\Delta|_{T_i}\ [\%], \tag{8}$$

where $T = \{T_1, T_2, \ldots, T_t\}$, with $T_1 = T_B$ and $T_t = T_C$.

The overall results for the N2 method are plotted in Figure 11. The 3D surface corresponds to the global average discrepancy values ($\overline{|\Delta|}_R$) in z-axis plotted with respect to the upper corner periods (T_C) of the response spectrum plateau in x-axis and to the values of strength reduction factor (R) in y-axis.

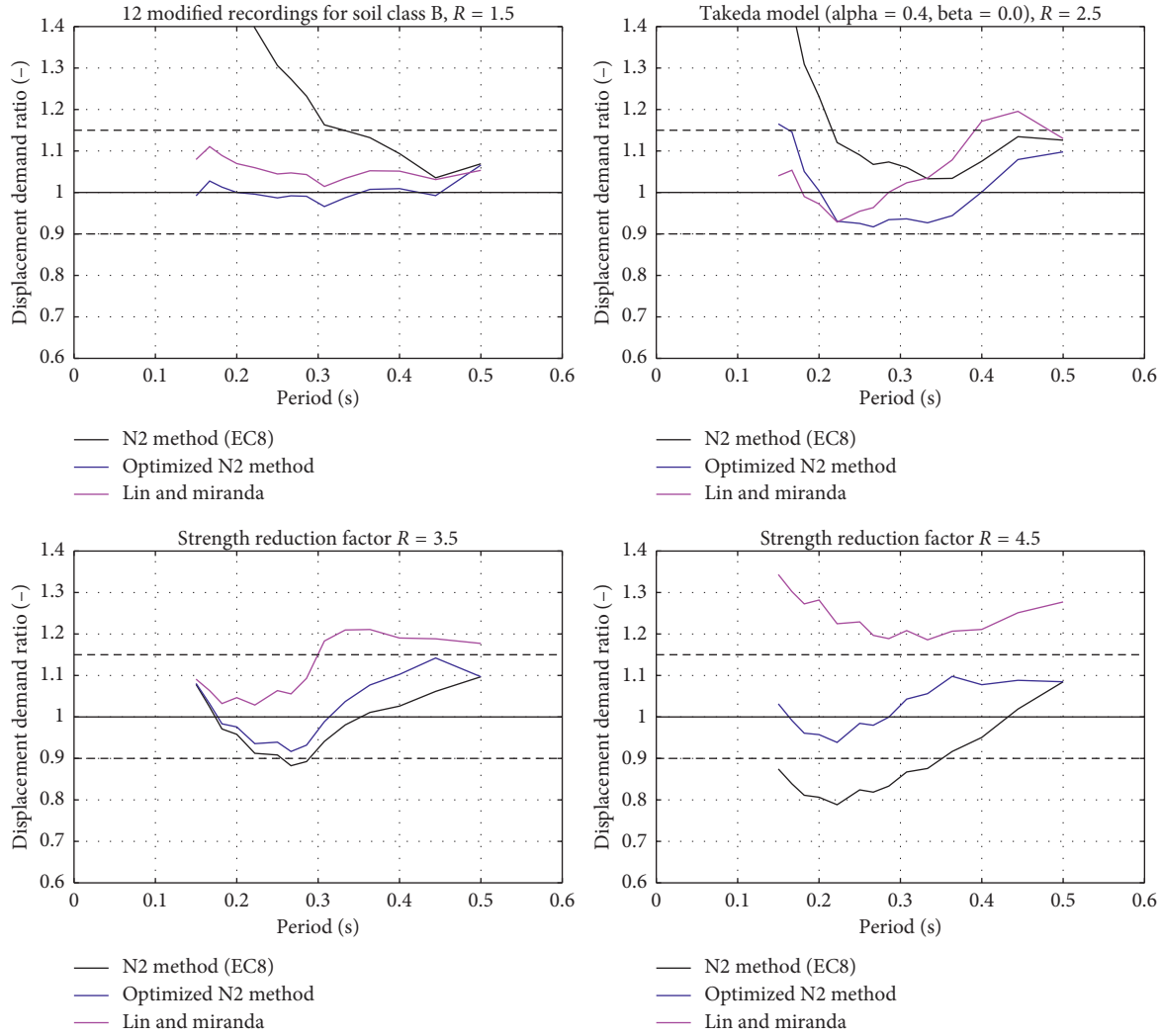

Figure 9: Assessment of the nonlinear displacement demands for soil class B and four values of strength reduction factors, $R = 1.5$ to $R = 4.5$. The ratio of predicted to actual (NLTHA) displacement demand is plotted with respect to the period. The plateau period range of the corresponding response spectrum (0.15 s to 0.50 s) is considered for the assessment.

The values of the global average discrepancy have a significant variation, ranging from about 4% at the minimum up to more than 40% at the maximum. Figure 11 shows that minimum global average discrepancies occur along a "valley" appearing at strength reduction factors (R) values around 3.5. For low values of the upper corner periods ($T_C \leq 0.5$ s) of the response spectrum plateau, the position of the minimum is shifted down towards $R = 3$.

The overall results for the optimized N2 method and the Lin and Miranda method are plotted side by side in Figure 12. The accuracy of the optimized N2 method is evidenced by Figure 12 (left) since the 3D surface of the global average discrepancy values is relatively flat and does not reach 10% at any point, ranging from 2% to 9%. The accuracy of the Lin and Miranda method is inferior to the one of the optimized N2 method. In Figure 12 (right) the 3D plots of the global average discrepancy of the Lin and Miranda method are flat, in a similar way to the optimized N2 method, at low values of strength reduction factors of up to about $R = 2.5$. Thus, both methods are accurate for this range of R. However, the discrepancies of the Lin and Miranda method significantly increase for higher values of R, especially for low values of the upper corner periods (T_C).

Based on the results described above, a value of 8.5% is selected in the following as a threshold for the global average discrepancy to evaluate the accuracy of the methods. Such a value ensures that the displacement demand predictions practically remain within an acceptable range of 90% and 115% of the NLTHA displacement demand along the plateau range.

In addition, the overall accuracy results are plotted in Figure 13 using a pixelized representation. Figure 13 contains a separate plot for each investigated method. In each plot, pixel coordinates correspond to the values of strength reduction factor (R) in y-axis with respect to the upper corner periods (T_C) of the response spectrum plateau in x-axis. As a consequence, the results for EC8 soil class B for instance appear along the vertical lines at $T_C = 0.5$ s. The

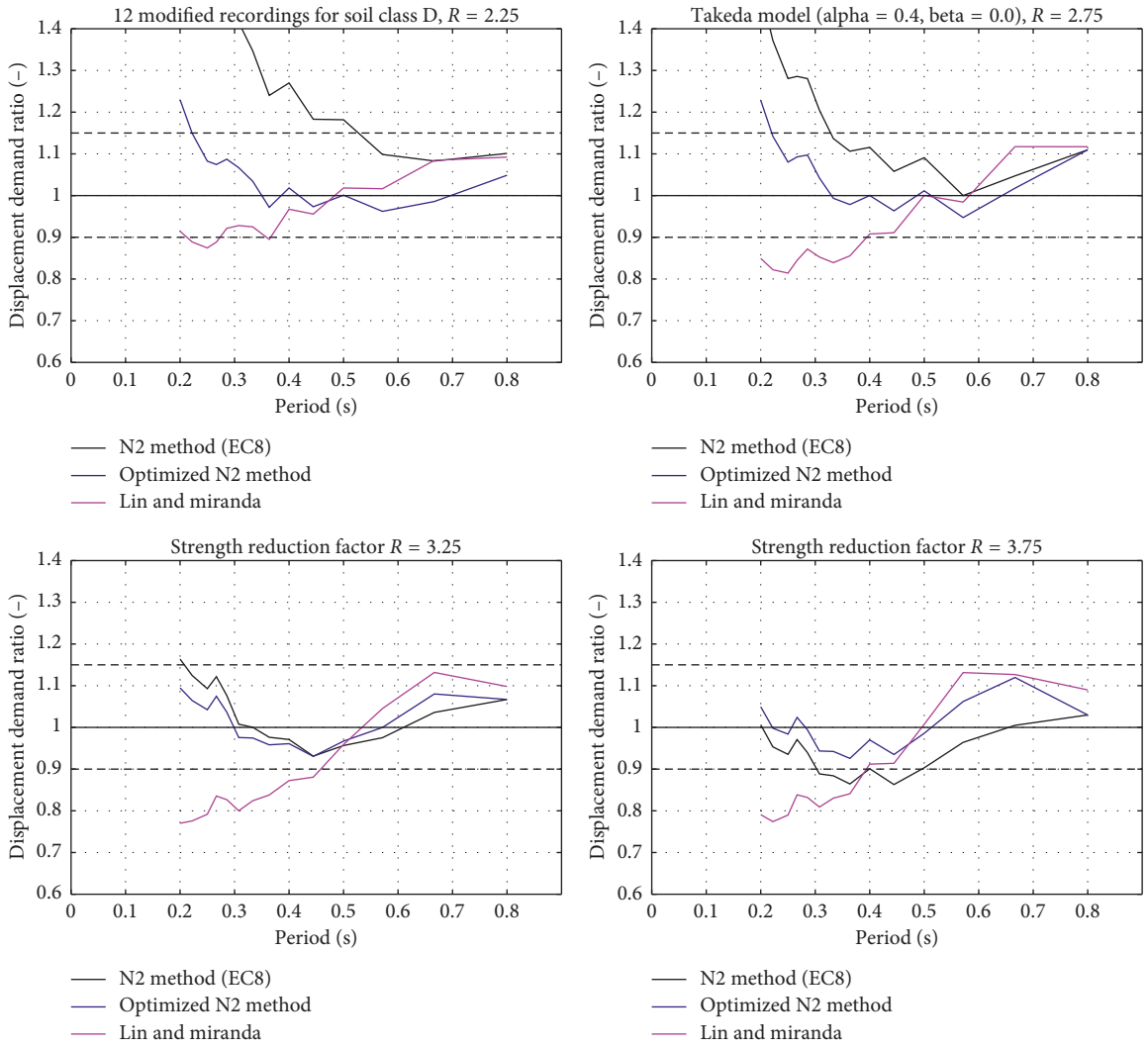

Figure 10: Assessment of the nonlinear displacement demands for soil class D and four values of strength reduction factors, $R = 2.25$ to $R = 3.75$. The ratio of predicted to actual (NLTHA) displacement demand is plotted with respect to the period. The plateau period range of the corresponding response spectrum (0.20 s to 0.80 s) is considered for the assessment.

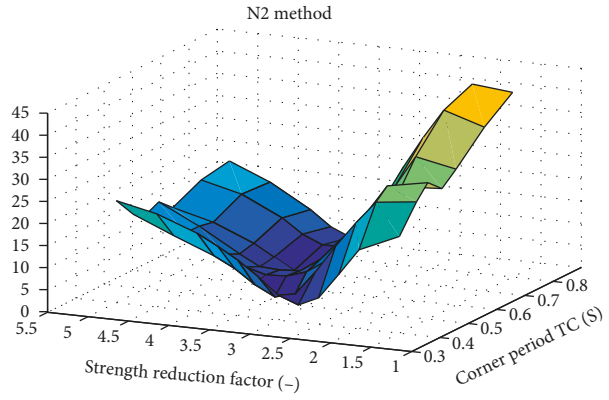

Figure 11: Overall results for the N2 method. The global average discrepancy values are plotted in 3D (z-axis) with respect to the strength reduction factor values (R) in y-axis and upper corner period of the plateau (T_C) in x-axis. A minimum "valley" appears for R values around $R = 3.5$.

pixels are full if the method is accurate for the corresponding couple of values (R and T_C) and empty if the method is not considered as accurate. Additional computations are performed for intermediate values of upper corner period T_C according to specific response spectra of microzonation studies of the cities of Martigny and Yverdon (see Section 3.1). The response spectrum of microzone M3 for Martigny has an upper corner period for the plateau of $T_C = 0.46$ s (Figure 4). The set of 12 recordings selected for microzone S3 of the spectral microzonation study of the city of Yverdon [20] was used one more time but modified to match an EC8 compatible response spectrum with an upper corner period for the plateau of $T_C = 0.7$ s. Another set of 12 recordings selected for the upgrade of microzone S3 of Yverdon was used to develop the EC8 compatible response spectrum with upper corner plateau period of $T_C = 0.55$ s. Consequently, the seven upper corner periods (T_C) of response spectra considered are 0.4 s for EC8 soil class A; 0.46 s for microzone

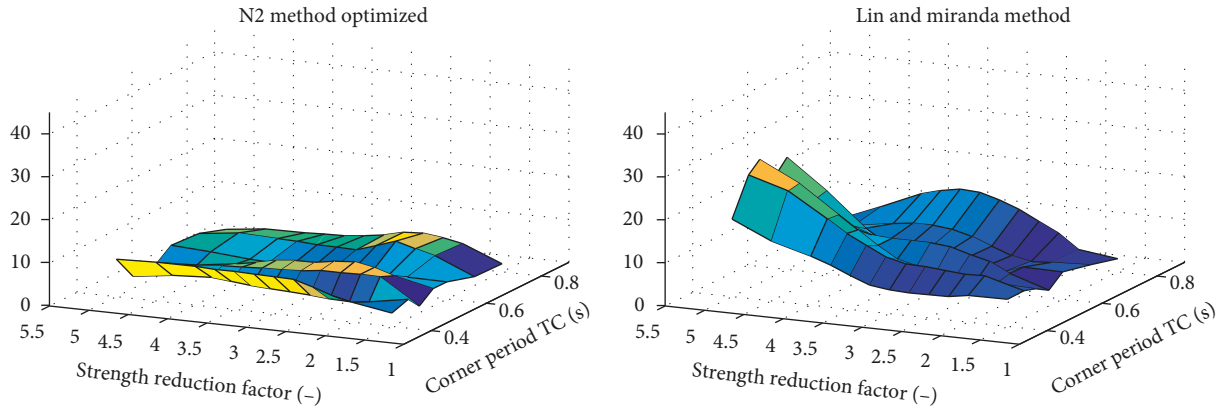

Figure 12: Overall results for the optimized N2 method (left) and Lin and Miranda method (right). The 3D surface plot of the global average discrepancy values is flat and low for the optimized N2 method, meaning that the method is all over accurate. The Lin and Miranda method shows similar trend but for low values of strength reduction factors only.

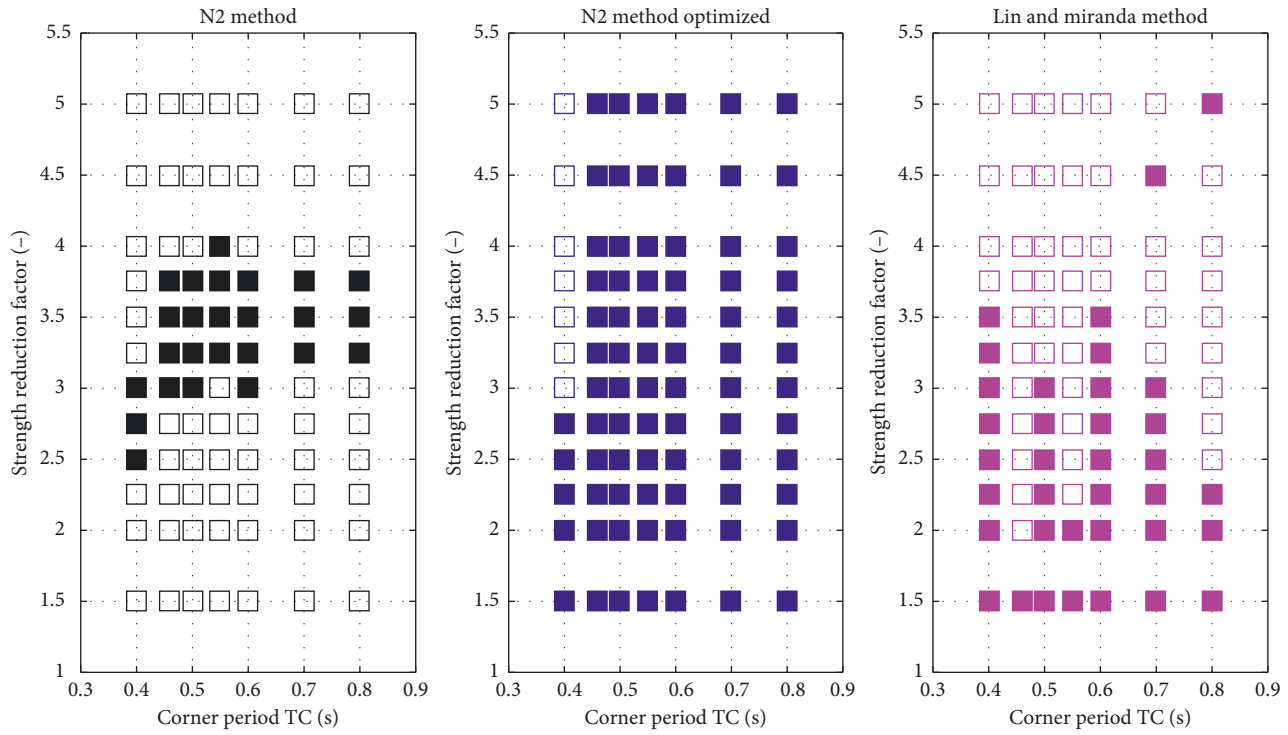

Figure 13: Overall results for the accuracy assessment of the 3 investigated methods. Pixel coordinates correspond to strength reduction factor values (R) and upper corner period of the plateau (T_C). Pixels are full if the method is accurate for the corresponding couple of values (R, T_C).

M3 (Martigny); 0.5 s for EC8 soil class B; 0.55 s for modified microzone S3; 0.6 s for EC8 soil class C; 0.7 s for microzone S3; and 0.8 s for soil class D. The 12 strength reduction factors considered are: 1.50; 2.00; 2.25; 2.50; 2.75; 3.00; 3.25; 3.50; 3.75; 4.00; 4.50; and 5.00.

Figure 13 shows that the accuracy range of the N2 method is essentially restricted to values of strength reduction factors between $R = 3$ and $R = 3.75$. This range even decreases with increasing values of the upper corner period of the plateau (T_C). For EC8 soil class D with $T_C = 0.8$ s, the N2 method is only accurate for strength reduction factors between $R = 3.25$ and $R = 3.75$. The accuracy range is shifted down for short values of T_C. For EC8 soil class A with $T_C = 0.4$ s, the N2 method is accurate for strength reduction factors between $R = 2.5$ and $R = 3$. For smaller values of R, the N2 method overestimates the displacement demand and for higher values of R, displacement demand is underestimated. By contrast, the optimized N2 method is generally

accurate. Except for values of strength reduction factor $R = 3$ and above in case of EC8 soil class A response spectrum, the optimized N2 method is accurate for all soil classes and microzones considered and for all R values. The domain over which the Lin and Miranda method is accurate may not be obviously described. The Lin and Miranda method tends to be accurate for small values of strength reduction factors ($R \leq 3.0$). For EC8 soil class A response spectrum, the Lin and Miranda method performs well up to a value of $R = 3.5$.

4.2. Results for Response Spectra with Different Shapes after the Plateau. For EC8 response spectra, the shape after the plateau is defined by a constant pseudovelocity range ($1/T$ from corner period T_C to period T_D) followed by a constant relative displacement range ($1/T^2$ after T_D). However, different shapes after the plateau, more specifically gentler or steeper decreasing branches, may be specified for instance in case of detailed spectral microzonation studies. The impact of steeper or gentler branches than constant pseudovelocity ($1/T$) decreasing branches on the accuracy of the displacement demand prediction is also preliminarily investigated in this study. The influence of the shape of the decreasing branch of the response spectrum is found to be particularly significant. Figure 14 shows the results obtained for EC8 soil class C and similar response spectra. In these plots, pixel coordinates correspond to the values of strength reduction factor (R) in y-axis with respect to the exponent of the declining branch ($1/T^\alpha$) of the response spectrum plateau in x-axis. As a consequence, the results for EC8 soil class C appear along the vertical lines at $\alpha = 1.0$ in Figure 14. As in previous figures, the pixels are full if the method is accurate for the corresponding couple of values (R, α) and empty if the method is considered inaccurate.

Additional computations are performed for specific response spectra, of the Yverdon spectral microzonation study, that have the same upper corner period T_C as soil class C ($T_C = 0.6$ s) but other values of the exponent of the decreasing branch ($1/T^\alpha$) after the plateau. The response spectrum of microzone S4 for Yverdon has an exponent of the decreasing branch after the plateau of $\alpha = 0.74$ [20]. The response spectrum of microzone S2 for Yverdon has an exponent of the decreasing branch after the plateau of $\alpha = 1.6$ [20]. The set of 12 recordings selected for microzone S3 for Yverdon, that has been used for simulations shown in Figures 11–13 [20], are modified to match a corresponding response spectrum with an exponent of the decreasing branch after the plateau of $\alpha = 0.87$. The set of 12 recordings selected for microzone S4 of Yverdon are modified to match a corresponding response spectrum with an exponent of the decreasing branch after the plateau of $\alpha = 0.66$.

Figure 14 shows that the accuracy domain for the N2 method is strongly affected by the value of the exponent of the decreasing branch after the plateau. The accuracy domain is significantly reduced for $\alpha = 0.66$ and shifted up towards higher values of strength reduction factor for $\alpha = 1.6$. The accuracy domains for the optimized N2 method and the Lin and Miranda method are less affected for values of α smaller than one but they are shifted down for $\alpha = 1.6$. For the Lin and Miranda method, the domain of accuracy even increases for values of α smaller than one.

Figure 15 shows the results obtained for EC8 soil class D and similar response spectra. The results for EC8 soil class D appear along the vertical lines at $\alpha = 1.0$. Additional computations are performed for specific response spectra of the spectral microzonation study of the city of Sion with same (or nearly the same for microzone A2) upper corner period T_C as soil class D ($T_C = 0.8$ s) but with different values of the exponent of the decreasing branch ($1/T^\alpha$) after the plateau. The response spectrum of microzone A2 for Sion has an exponent of the declining branch after the plateau of $\alpha = 0.77$ (Figure 4). The response spectrum of microzone A1 for Sion has an exponent of the declining branch after the plateau of $\alpha = 1.08$ (Figure 4). The response spectrum of microzone A3 for Sion has an exponent of the declining branch after the plateau of $\alpha = 1.49$ (Figure 4). Figure 15 shows a similar yet more pronounced trend than Figure 14 regarding the accuracy domains for the three investigated methods. The N2 method may even be considered as completely inaccurate in case of $\alpha = 0.77$. The accuracy domain for the optimized N2 method is also strongly reduced for $\alpha = 0.77$. The accuracy domain is again shifted towards higher values of strength reduction factor for $\alpha = 1.49$ for the N2 method. By contrast, the accuracy domain of the three methods is not affected for $\alpha = 1.08$. The accuracy domains for the Lin and Miranda method are not significantly affected by the values of α.

5. Summary and Conclusions

The accuracy of three methods for nonlinear seismic displacement demand predictions is carefully evaluated in this study: the simplified version of the N2 method, the optimized N2 method, and the Lin and Miranda method. The investigation is performed for the plateau range of response spectra corresponding to the Eurocode 8 Type-1 soil classes and to response spectra of detailed microzonation studies. Accuracy is assessed through a comparison of the displacement demand computed using nonlinear time-history analysis (NLTHA) with the displacement demand predicted by the three methods.

The accuracy domain significantly depends on the response spectrum plateau extension (value of the upper corner period, T_C). Furthermore, the accuracy of displacement demand predictions is found to be dependent on the shape of the response spectrum after the plateau. A less steeply decreasing branch after the plateau affects the accuracy. The study focuses on SDOF and on hysteretic models featuring ductile structural behavior under seismic actions. These choices reflect the objectives of the study. Even if some slight differences arise when using MDOF representations (e.g., [31]), the essential characteristics of the seismic response are captured by SDOF models.

The results show that the simplified version of the N2 method provides accurate predictions for strength reduction factor values between $R = 3$ and $R = 3.75$. This range decreases further with increasing values of the upper

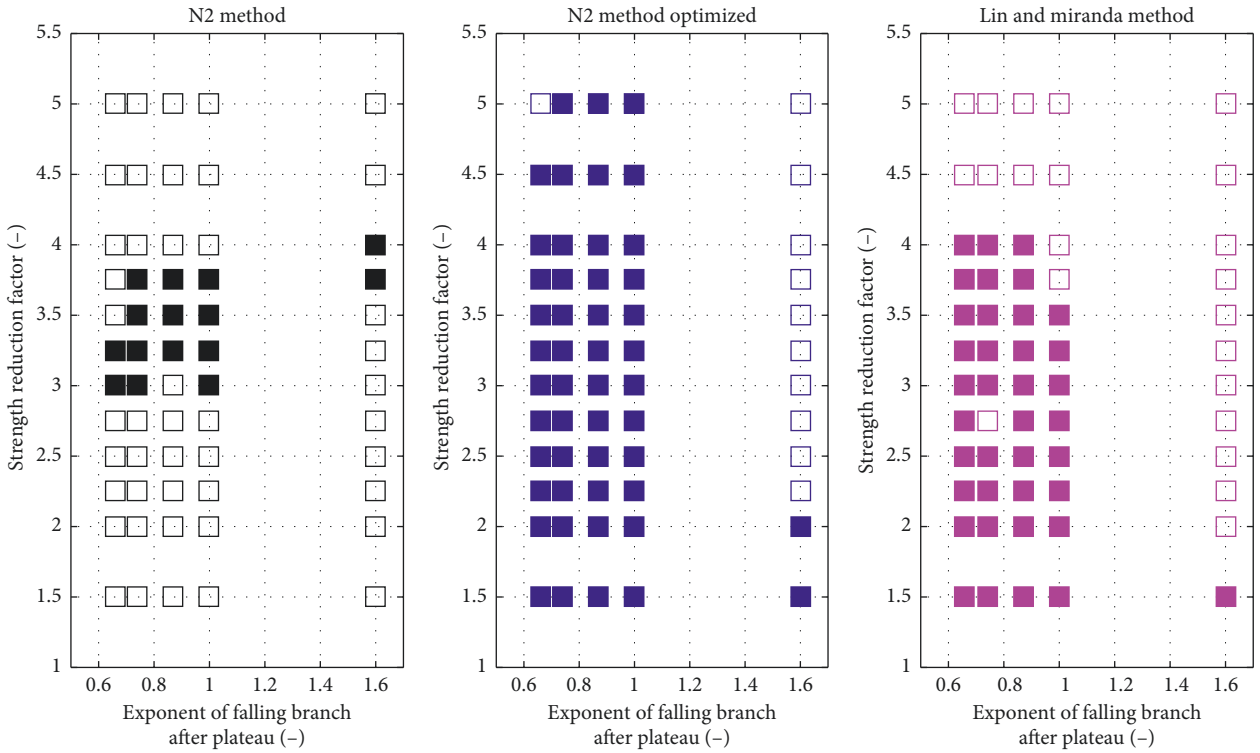

FIGURE 14: Accuracy assessment of the 3 investigated methods for soil class C with respect to the exponent of the decreasing branch after the plateau of the response spectrum. Pixel coordinates correspond to strength reduction factor values (R) and exponent of the decreasing branch (α). Pixels are full if the method is accurate for the corresponding couple of values (R, α).

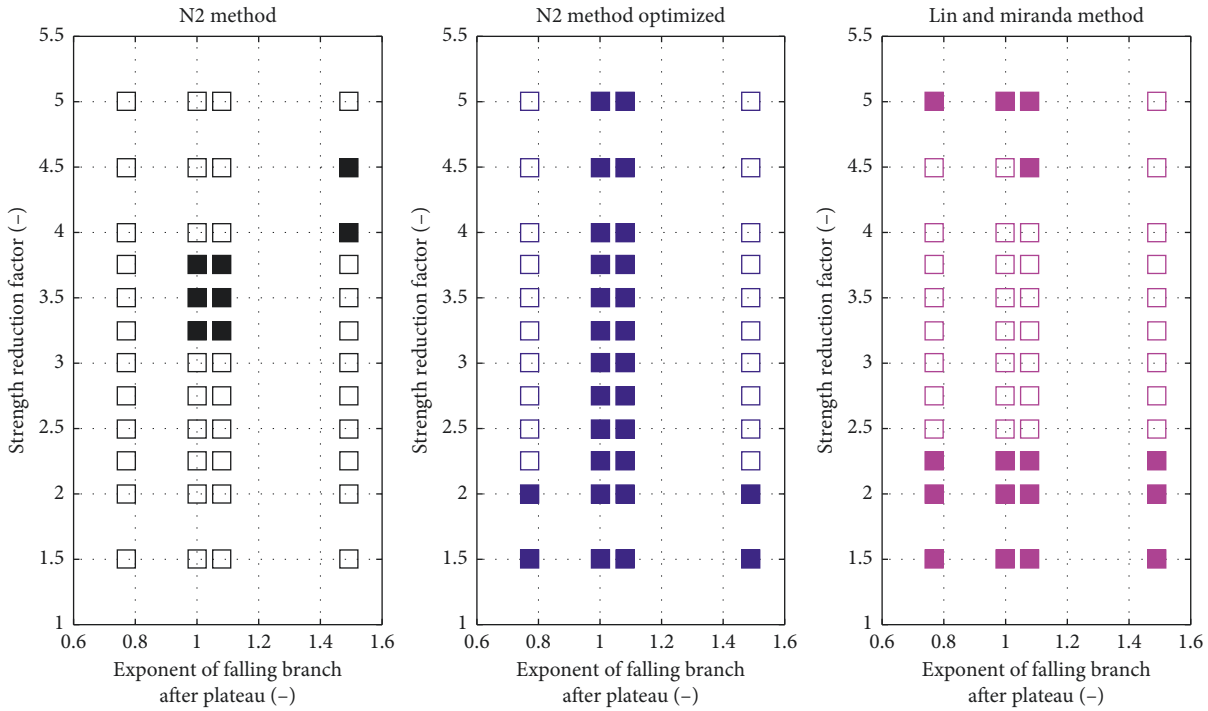

FIGURE 15: Accuracy assessment of the three investigated methods for soil class D with respect to the exponent of the decreasing branch after the plateau of the response spectrum.

Earthquake	Date	Magnitude	Distance (km)	PGA (m/s_2)	Soil A	Soil B	Soil C	Soil D	Sion			Martigny		Yverdon			
									A1	A2	A3	M2	M3	S2	S3	S4	S3mod
Friuli (as)	11.09.1976	5.3 Mw	8	1.931	X												
Friuli (as)	11.09.1976	5.5 Mw	10	2.260								X					
Friuli (as)	16.09.1977	5.4 Mw	14	0.910	X												
Volvi	04.07.1978	5.12 Ms	16	1.125	X												
El Asnam (as)	08.11.1980	5.2 Mw	18	0.946	X												
Friuli (as)	15.09.1976	6 Mw	11	1.069		X	X								X	X	
Friuli (as)	15.09.1976	6 Mw	17	2.319										X			X
Basso Tirreno	15.04.1978	6 Mw	18	1.585			X	X						X	X		X
Valnerina	19.09.1979	5.8 Mw	5	2.012										X			
Friuli	06.05.1976	6.5 Mw	27	3.499							X						
Volvi	20.06.1978	6.2 Mw	29	1.430		X	X							X	X		X
Montenegro	24.05.1979	6.2 Mw	33	2.652								X		X			
Montenegro	24.05.1979	6.2 Mw	8	2.624							X						
Montenegro	24.05.1979	6.2 Mw	30	0.754	X												
Montenegro	24.05.1979	6.2 Mw	17	2.703		X											
Alkion	25.02.1981	6.3 Mw	25	1.176		X	X	X						X	X		X
Aigion	15.06.1995	6.5 Mw	43	0.911			X									X	
Adana	27.06.1998	6.3 Mw	30	2.644						X	X		X				
Montenegro	15.04.1979	6.9 Mw	65	2.509			X	X							X		X
Montenegro	15.04.1979	6.9 Mw	21	2.198					X	X	X	X	X	X			X
Campano	23.11.1980	6.9 Mw	23	1.776				X	X	X							X
Campano	23.11.1980	6.9 Mw	26	0.903			X									X	
Campano	23.11.1980	6.9 Mw	16	1.725				X	X	X		X			X		
Campano	23.11.1980	6.9 Mw	48	1.362													X
Campano	23.11.1980	6.9 Mw	33	0.975	X	X										X	
Campano	23.11.1980	6.9 Mw	32	3.166								X	X				
Alkion	24.02.1981	6.6 Mw	33	3.036					X	X	X	X	X				
Alkion	24.02.1981	6.6 Mw	33	2.256									X				
Alkion	24.02.1981	6.6 Mw	34	2.838					X	X	X	X		X			
Spitak	07.12.1988	6.7 Mw	36	1.796				X	X						X		X
Strofades	18.11.1997	6.6 Mw	144	0.907	X											X	
Strofades	18.11.1997	6.6 Mw	32	1.289		X											X
Tabas	16.09.1978	7.4 Mw	55	1.003	X	X										X	
Tabas	16.09.1978	7.4 Mw	11	3.779									X				
Tabas	16.09.1978	7.4 Mw	100	1.002	X												
Manjil	20.06.1990	7.4 Mw	81	0.951	X	X										X	
Manjil	20.06.1990	7.4 Mw	131	1.341				X	X	X					X		
Gulf of Akaba	22.11.1995	7.1 Mw	93	0.894	X	X										X	
Izmit	17.08.1999	7.6 Mw	113	2.580						X	X	X	X				
Izmit	17.08.1999	7.6 Mw	172	0.974	X											X	
Izmit	17.08.1999	7.6 Mw	110	1.698			X										
Izmit	17.08.1999	7.6 Mw	48	2.334			X	X	X			X		X	X		X
Izmit	17.08.1999	7.6 Mw	48	1.329										X			
Izmit	17.08.1999	7.6 Mw	78	1.040		X	X	X							X	X	
Izmit	17.08.1999	7.6 Mw	101	1.611													X
Izmit	17.08.1999	7.6 Mw	96	1.120		X	X							X	X	X	
Izmit	17.08.1999	7.6 Mw	10	2.192				X	X	X							
Izmit	17.08.1999	7.6 Mw	39	1.266				X	X	X					X		
Izmit	17.08.1999	7.6 Mw	34	3.542				X	X		X	X	X				
Izmit	17.08.1999	7.6 Mw	20	2.903						X	X						
Izmit	17.08.1999	7.6 Mw	20	2.903							X						
Izmit	17.08.1999	7.6 Mw	103	0.871		X	X									X	
Ano Liosia	07.09.1999	6.0 Mw	16	2.601										X			
Duzce 1	12.11.1999	7.2 Mw	22	2.902									X				
Kalamata	13.09.1986	5.9 Mw	10	2.909					X	X	X	X	X				
Umbria Marche	26.09.1997	5.7 Mw	3	3.382									X				
Umbria Marche	26.09.1997	5.7 Mw	3	3.382							X	X	X				

Figure 16: Main characteristics of the selected records and their distribution in the different sets of the twelve recordings each (as = aftershock).

corner period for the plateau (T_C). For EC8 soil class D with $T_C = 0.8$ s, the N2 method provides accurate results for values between $R = 3.25$ and $R = 3.75$. Moreover, the accuracy range is shifted down for short values of T_C. For EC8 soil class A with $T_C = 0.4$ s, the N2 method is accurate for strength reduction factors between $R = 2.5$ and $R = 3$. Fortunately, the optimized N2 method is generally accurate, regardless of the values of strength reduction factor and upper corner period for the plateau (T_C). The accuracy domain of the Lin and Miranda method is not easily determined; this method tends to be accurate for small values of strength reduction factors up to $R = 2.5$. As a

consequence, the simplified version of the N2 method leads to significant overestimations of the displacement demand for strength reduction factors smaller than 2.5 and to significant underestimations for strength reduction factors exceeding 4. For small values of the strength reduction factor ($R \leq 2.5$), the optimized N2 method and the Lin and Miranda method result in accurate displacement demand predictions.

Accuracy of displacement demand predictions also depends on the shape of the response spectrum after the plateau. A gently decreasing branch after the plateau considerably reduces accuracy. Although this finding needs to be investigated in more detail in future studies, preliminary results suggest a threshold value of the exponent of the decreasing branch after the plateau. In order to ensure a similar extent of the accuracy domain rather than for EC8 response spectrum, a threshold value of 0.75 for the exponent of the decreasing branch ($1/T^{\alpha}$) after the plateau is proposed. A value slightly larger than one for the exponent of the declining branch after the plateau is not problematic since it does not significantly affect the accuracy domain of the methods. This issue should be considered for the ongoing developments of EC8.

Appendix

The main characteristics of the selected earthquakes and their distribution in the different sets of 12 recorded earthquakes each involved in the study are summarized in the table of Figure 16.

Data Availability

The data used to support the findings of this study are available from ResearchGate (DOI: 10.13140/RG.2.2.23337.54883) and from the corresponding author upon request.

Disclosure

This research is based on a collaborative research project achieved with the specialized engineering company Résonance Ingénieurs-Conseils SA, Carouge, Switzerland. The investigations were achieved within the framework of an internal research project and were performed as part of the employment of both authors.

Conflicts of Interest

The authors declare that they have no conflicts of interest.

References

[1] CEN (Comité Européen de Normalisation), *Eurocode 8: Design Provisions for Earthquake Resistance of Structures—Part 1: General Rules, Seismic Actions and Rules for Buildings, EN 1998-1:2004*, CEN, Brussels, Belgium, 2004.

[2] L. Diana, A. Manno, P. Lestuzzi, S. Podestà, and C. Luchini, "Impact of displacement demand reliability for seismic vulnerability assessment at an urban scale," *Soil Dynamics and Earthquake Engineering*, vol. 112, pp. 35–52, 2018.

[3] R. Riddell, P. Hidalgo, and E. Cruz, "Response modification factors for earthquake resistant design of short period buildings," *Earthquake Spectra*, vol. 5, no. 3, pp. 571–590, 1989.

[4] T. Vidic, P. Fajfar, and M. Fischinger, "Consistent inelastic design spectra: strength and displacement," *Earthquake Engineering & Structural Dynamics*, vol. 23, no. 5, pp. 507–521, 1994.

[5] Y.-Y. Lin and E. Miranda, "Evaluation of equivalent linear methods for estimating target displacements of existing structures," *Engineering Structures*, vol. 31, no. 12, pp. 3080–3089, 2009.

[6] M. J. Kowalsky, "Displacement-based design-a methodology for seismic design applied to RC bridge columns," Master's thesis, University of California at San Diego, La Jolla, CA, USA, 1994.

[7] Applied Technology Council (ATC), *Improvement of Nonlinear Static Seismic Analysis Procedures: FEMA-440*, ATC, Redwood City, CA, USA, 2005.

[8] P. Fajfar, "A nonlinear analysis method for performance-based seismic design," *Earthquake Spectra*, vol. 16, no. 3, pp. 573–592, 2000.

[9] H. Norda and C. Butenweg, "Möglichkeiten und grenzen der anwendbarkeit statisch nichtlinearer verfahren nach DIN EN 1998-1," *Bauingenieur*, vol. 86, pp. 13–21, 2011, in German.

[10] C. Michel, P. Lestuzzi, and C. Lacave, "Simplified non-linear seismic displacement demand prediction for low period structures," *Bulletin of Earthquake Engineering*, vol. 12, no. 4, pp. 1563–1581, 2014.

[11] L. Diana, A. Manno, and P. Lestuzzi, "Seismic displacement demand prediction in non-linear domain: optimization of the N2 method," *Earthquake Engineering and Engineering Vibration*, vol. 18, no. 1, pp. 141–158, 2019.

[12] A. Veletsos and N. Newmark, "Effect of inelastic behavior on the response of simple systems to earthquake motion," in *Proceedings of the 2nd World Conference on Earthquake Engineering*, vol. 2, pp. 895–912, Tokyo, Japan, July 1960.

[13] P. Lestuzzi and M. Badoux, "An experimental confirmation of the equal displacement rule for RC structural walls," in *Proceedings of the Fib-Symposium: Concrete Structures in Seismic Regions, Paper n° 127*, Athens, Greece, May 2003.

[14] F. Graziotti, A. Penna, E. Bossi, and G. Magenes, "Evaluation of displacement demand for unreinforced masonry buildings by equivalent SDOF systems," in *Proceedings of the 9th International Conference on Structural Dynamics, EURODYN 2014*, A. Cunha, E. Caetano, and G. Muller, Eds., , Porto, Portugal, June 2014.

[15] W. D. Iwan, "Estimating inelastic response spectra from elastic spectra," *Earthquake Engineering & Structural Dynamics*, vol. 8, no. 4, pp. 375–388, 1980.

[16] E. Miranda and J. Ruiz-García, "Evaluation of approximate methods to estimate maximum inelastic displacement demands," *Earthquake Engineering & Structural Dynamics*, vol. 31, no. 3, pp. 539–560, 2002.

[17] T. J. Sullivan, G. M. Calvi, and N. Priestley, "Initial stiffness versus secant stiffness in displacement-based design," in *Proceedings of the 13th World Conference of Earthquake Engineering (WCEE)*, vol. 2888, Vancouver, Canada, August 2004.

[18] Y.-Y. Lin and E. Miranda, "Noniterative equivalent linear method for evaluation of existing structures," *Journal of Structural Engineering*, vol. 134, no. 11, pp. 1685–1695, 2008.

[19] N. Ambraseys, P. Smit, R. Sigbjornsson, P. Suhadolc, and B. Margaris, *Internet Site for European Strong-Motion Data*,

European Commission, Research Directorate General, Environment and Climate Program, Brussels, Belgium, 2002.
[20] P. Lestuzzi and M. Badoux, *Evaluation Parasismique des Constructions Existantes*, Presses Polytechniques et Universitaires Romandes, Lausanne, Switzerland, in French, 2013.
[21] CREALP, Centre de Recherche sur l'Environnement Alpin, 2019, http://www.crealp.ch.
[22] N. A. Abrahamson, "Non-stationary spectral matching," *Seismological Research Letters*, vol. 63, no. 1, p. 30, 1992.
[23] P. Schwab and P. Lestuzzi, "Assessment of the seismic nonlinear behavior of ductile wall structures due to synthetic earthquakes," *Bulletin of Earthquake Engineering*, vol. 5, no. 1, pp. 67–84, 2007.
[24] P. Lestuzzi, H. Charif, S. Rossier, M. Ferrière and, and J.-P. Person, "Nonlinear time-history analysis for validation of the displacement-based seismic assessment of the RC upper bridge of a dam," *Advances in Civil Engineering*, vol. 2018, Article ID 9879101, 13 pages, 2018.
[25] M. Saiidi and M. A. Sozen, "Simple nonlinear seismic analysis of R/C structures," *Journal of the Structural Division*, vol. 107, no. 5, pp. 937–953, 1981.
[26] P. Lestuzzi and M. Badoux, "The gamma model: a simple hysteretic model for RC walls," in *Proceedings of the Fib-Symposium: Concrete Structures in Seismic Regions, Paper n° 126*, Athens, Greece, May 2003.
[27] T. Takeda, M. A. Sozen, and N. N. Nielsen, "Reinforced concrete response to simulated earthquakes," *Journal of the Structural Division ASCE*, vol. 96, pp. 2557–2573, 1970.
[28] S. Otani, "Inelastic analysis of R/C frame structures," *Journal of the Structural Division*, vol. 100, no. 7, pp. 1433–1449, 1974.
[29] R. W. Litton, *A contribution to the analysis of concrete structures under cyclic loading*, Ph.D. thesis, Civil Engineering Department, University of California, Berkeley, CA, USA, 1975.
[30] R. Allahabadi and G. H. Powell, "Drain-2DX user guide," Report No. UCB/EERC-88/06, College of Engineering, University of California, Berkeley, CA, USA, 1988.
[31] P. Lestuzzi, Y. Belmouden, and M. Trueb, "Non-linear seismic behavior of structures with limited hysteretic energy dissipation capacity," *Bulletin of Earthquake Engineering*, vol. 5, no. 4, pp. 549–569, 2007.

Hindawi
Advances in Civil Engineering
Volume 2019, Article ID 8385342, 10 pages
https://doi.org/10.1155/2019/8385342

Research Article

A Method to Improve the Seismic Performance of Steel Moment Resisting Frames Based on Eigenfrequency Optimization

Orlando Arroyo,[1] **Angie V. Osorio**,[2] **and María Catalina Vargas**[2]

[1]*Assistant Professor, Universidad de La Sabana, Chía, Colombia*
[2]*Research Assistant, Universidad de La Sabana, Chía, Colombia*

Correspondence should be addressed to Orlando Arroyo; orlando.arroyo@unisabana.edu.co

Received 21 March 2019; Revised 9 June 2019; Accepted 23 June 2019; Published 18 July 2019

Guest Editor: Edén Bojórquez

Steel moment resisting frames are a structural system used throughout the world, mainly for their ductility and the speed and ease of their construction. These buildings are usually designed per procedures based on seismic design codes, seeking to minimize the total cost of the building. To aid in better building designs, researchers have proposed different methodologies, which have been proven to be effective. However, their practical use has been limited by their low computational efficiency and their difficulty to implement by practicing engineers. This article proposes a method to improve the seismic performance of steel moment resisting frame buildings based on eigenfrequency optimization. The main advantage of the proposed method is its computational efficiency and that it is simple to implement. The method is demonstrated for a four-story and an eight-story building, whose seismic performance is compared to traditional building designs using nonlinear analyses and seismic fragility functions. The results show that the seismic performance improves significantly with the proposed method with respect to that of traditionally designed buildings, reducing their seismic fragility and increasing their overstrength. These findings and the computational efficiency of the method suggest that it is a viable alternative for use within engineering practice.

1. Introduction

Steel moment resisting frames (SMRF) are a structural system used throughout the world. This structural system is used in many countries mainly for the speed and ease of its construction and because of the satisfactory performance demonstrated in recent earthquakes. Traditionally, these buildings are designed by structural engineers according to the ductility, strength, and drift provisions of seismic design codes. These provisions change from code to code; for instance, if the North American and other international provisions are compared with the Eurocode 8 in terms of drift requirements, it is found that the latter is more stringent, and it can be evidenced in case of the stability coefficient, which often controls the design of SMRF and allows buildings to achieve a considerable overstrength [1].

Accounting for the need to produce designs within reasonable times, current design codes provide guidelines for designing SMRF based on elastic analyses, using factors to account for the nonlinear nature of the seismic response (q-factor for Eurocode 8 and R factor for American codes). This practice has remained mainstream through many decades although it does not always lead to a conservative design [2]. Acknowledging these facts, current design codes are continuously under revision and they are updated as findings from research programs and experience gained from earthquake over the years become available [3].

The result of the application of the seismic codes is that most design offices use elastic models to design most SMRF buildings, which are analyzed using the equivalent lateral force or response spectrum analysis. The mainstream practice is to first calculate the section profiles that satisfy the drift requirement, then proceed to check the strength and ductility requirements, and finally design the member connections. In this design process, the experience acquired in previous projects plays an important role, as it serves as a

guidance for the engineer, who often uses it to check the design outcome. Frequently, most engineers aim to minimize the total cost of the building because of the increasing market competition. Because of this approach, the performance of most SMRF buildings is close to the minimum objective of the design code.

Reflecting on its ubiquity and to aid in better building designs for SMRF buildings, researchers have proposed different methodologies, which are based on two approaches: structural optimization and performance-based design (PBD). In structural optimization, several methods have been proposed [4] based on different optimization frameworks [5] with objectives such as weight minimization and performance optimization [6], for which they have used several evolutionary optimization algorithms. Among them, there are methods based on teaching-learning [7], ant colony [8], harmony search [9], bee colony [10], colliding body [11], dolphin echolocation [12], firefly algorithms with neural networks [13], and cuckoo search [14]. In performance-based design [15], SMRF are designed to meet certain seismic performance goals, requiring successive iterations that need a seismic performance evaluation. This approach has been applied to buckling-restrained frames [16, 17] and self-centering SMF with braces [18] and for designing SMRF with uncertainty quantification [19, 20].

Both approaches have demonstrated effectiveness in improving the seismic design of SMRF, and PBD has earned a recommendation per the ASCE as a pathway to impact structural engineering [21]. However, despite these benefits of structural optimization and PBD, their usage in engineering practice has been limited. Many reasons can explain this though there is a strong possibility that it is because these approaches use nonlinear models for the buildings. According to a survey in the US, nonlinear models are considered by 60% of engineers as time consuming/not practical [22] and have been identified as a factor that limits the practical application of a design approach [23].

Contributing to the need of efficient and practical methods which can attract the attention of practicing engineers, this article proposes a method to improve the seismic performance of SMRF, whose novelty is a problem formulation that uses the natural frequencies as an objective function to optimize the seismic design, and the constraints to ensure the strength, capacity, and ductility requirements of design codes. This formulation brings two advantages to the proposed method: (1) it is easy to implement since it uses elastic models of the building and (2) it is computationally efficient and easy to integrate within engineering practice. The application of the method is demonstrated for two buildings, a four-story and an eight-story building. Both buildings are first designed per the traditional approach of engineering practice and then by the proposed method with the aid of the Borg-MOEA algorithm [24]. The method's improvements in seismic performance are demonstrated using OpenSees [25] to compare the behaviour of this building against the same building designed in a traditional fashion. Further comparisons of the seismic performance are conducted based on seismic fragility functions that were developed based on the OpenSees results.

2. Eigenfrequency Optimization Method for the Design of Steel Moment Resisting Frames

Eigenfrequency optimization describes a problem where one or more natural frequencies, ω_n, of a structure or mechanism are optimized [26, 27]. This approach makes sense when the structures are subjected to dynamic loads whose response depends on one or more of its natural frequencies. Several problems involving dynamic loads in structural engineering have been solved using eigenfrequency optimization, such as maximizing the strength of RC column joints [28] and vibration reduction in trusses [29]. Additionally, this approach was used to optimize column dimensions using a surrogate membrane model of reinforced concrete moment frames, increasing the structure overstrength and ductility [30].

The performance of a building during an earthquake seems to be greatly affected by the smallest natural frequencies of the structure. The reliance of the seismic response on the natural frequencies has been leveraged to develop efficient structural analysis procedures for calculating the seismic response of buildings, such as the modal pushover analysis [31, 32]. Moreover, several standards use the dominating nature of the smallest natural frequencies to recommend seismic response methods such as the equivalent lateral force (ELF) and the modal response spectrum analysis, both using elastic models of the buildings [33, 34].

The natural frequencies of a structure are properties that can be optimized using eigenfrequency optimization, suggesting that it is a suitable approach to design buildings with improved seismic performance. Furthermore, the optimization of the natural frequencies of a structure has low computational costs since the objective function uses the elastic model of the building to make the calculation, which is significantly less complex than the nonlinear analyses required by existing methods for optimizing the design of SMRF.

2.1. Formulation of Eigenfrequency Optimization for Steel Moment Resisting Frames. Developing an efficient formulation of eigenfrequency optimization for SMRF has three challenges. The first one is that the elements sections in a SMRF are represented by discrete variables, given by the typical steel section profiles used in construction practice. Handling this problem requires expressing the element sections of the SMRF as a vector $\mathbf{p}$ of integer indexes, each one corresponding to a section profile, which has associated the corresponding section properties (area, moment of inertia, etc.). A second challenge stems from the fact that the problem optimizes natural frequencies; therefore, it is necessary to introduce a constraint to the problem that limits the cost of the building, ensuring a competitive design. This is addressed by imposing a limit W_0 to the total weight of the building $W(\mathbf{p})$, which is a function of the profiles $\mathbf{p}$ of the structural elements. A third challenge is ensuring that the resulting design satisfies design code requirements for resistance (e.g., strong column-weak beam) and functionality (e.g., deflexion control). To overcome this challenge, each element of the building (i.e., columns and beams) must be

limited between a minimum profile $p_{i,\min}$ and a maximum profile $p_{i,\max}$. In addition to fulfilling design code requirements, this scheme also contributes to limit the search space, avoiding the possibility of generating unviable solutions that would be discarded by the design code constraints.

With those considerations into account, equation (1) shows the formulation of the eigenfrequency optimization problem for SMRF, based on the stiffness (K) and mass matrixes (M) of a given structure. Here, ω_n is defined as the n-th natural frequency of the building and $\mathbf{p}$ is an integer vector with the section profiles, which has associated the corresponding section properties:

$$\begin{aligned} &\max && \{\omega_n\}_{n=1,\ldots,N,} \\ &\text{subject to} && p_{i,\min} \le p_i \le p_{i,\max} \\ &&& W(\mathbf{p}) \le W_0 \\ &&& [K - \omega_n^2 M]\varphi_n = 0. \end{aligned} \tag{1}$$

This formulation seeks to maximize the set of N first natural frequencies of the structure, subjected to three constraints. In the first constraint, $p_{i,\min}$ and $p_{i,\max}$ are the minimum and maximum index values of each element represented in $\mathbf{p}$. The second constraint accounts for the volume limit previously discussed. The third constraint comes from the structural dynamic theory, and it means that ω_n is a natural frequency of the structure.

2.2. Integration of Eigenfrequency Optimization in the Structural Design Workflow. Feasibility, understood as the degree to which the optimization procedure is easy or convenient to implement, is one critical aspect of an optimization method to succeed in engineering practice [23]. As demonstrated in equation (1), the proposed method uses the elastic properties of the building, so it is feasible for implementation in engineering practice. This section discusses the details for its integration.

Figure 1 shows the typical design process of SMRF. It starts with the evaluation of the gravity and seismic loads. After that, designers propose a set of initial dimensions for columns and beams, which are then used to check for the drift limit of the building. If the drift limit is not satisfied, a new set of dimensions is proposed until this condition is met. After that, designers proceed to check the strength and deflection requirements of design codes, and once these are met, the design is considered complete.

To assist engineers in designing SMRF with better seismic performance, the authors suggest applying the method herein proposed after all code requirements are satisfied, as illustrated by the dotted box in Figure 1. To achieve this goal, designers need to solve the problem from the previous section, considering the natural frequencies of the building as the objective function. In this regard, the authors recommend using the fundamental frequency as objective function for low-rise (i.e., less than 5 stories) buildings and adding more frequencies as the height increases. In addition, it is a good idea to consider W_0 as the weight of the design they have already completed and setting $p_{\min,i}$ as the index of the smallest section that satisfies the strength and deflection requirements.

This approach has several advantages. First, the design that results from the optimization satisfies not only the strength requirements but also the drift limit, as the method is maximizing the fundamental frequency (i.e., minimizing the fundamental period) and the drift limit is checked in the elastic range. Consequently, optimized building will have a smaller one than the traditionally designed building. The second advantage is that unlike existing methods, the proposed method does not need to perform any nonlinear analyses, significantly improving the computational performance. A third advantage of the proposed method is that the proposed formulation works for any type of buildings, regardless of their irregularity and whether they are two-dimensional and three-dimensional problems. In the latter case, the stiffness matrix must be formulated using the frame-type element which has 6 degrees of freedom on each element end. Similarly, the mass matrix must account for the additional degrees of freedom. In all cases, the method requires that the strength and ductility requirements must be met by the proper selection of the $p_{i,\min}$ and the $p_{i,\max}$ for the members profiles. The examples section provides strategies to achieve these requirements, ensuring that capacity design criteria such as strong column-weak beam are satisfied.

In this article, the software MATLAB® is used for creating functions with the implementation of this formulation. An example function for a two-dimensional 8-story building is available to download from this link. The function receives the indexes for columns and beams as inputs and returns the first two periods (associated to the eigenfrequencies) as outputs. In this study, the solver used is the Borg-MOEA [24], a state-of-the-art multiobjective optimization algorithm. The periods are selected as outputs because most algorithms are developed to minimize objective functions and not for maximization, like in eigenfrequency. Since the periods are inversely proportional to the frequencies, they are a suitable variable that is physically significant for the problem. That said, the eigenfrequency optimization can be solved using any multiobjective optimization algorithm.

3. Example Applications

Two structures are used to demonstrate the application of the proposed method (Figure 2). The first one is a four-story building with three identical beam spans of 6 m. The second one is an eight-story building with five spans, all of which are 6 m length. All floors in both buildings have a story height of 3 m.

These buildings were designed per the LRFD in the AISC 360-16 following the customary engineering practice and then by the proposed method. Two section profile databases were used for this purpose. Tables 1 and 2 show the profiles used for beams and columns, which range from the IPE100 to the IPE600 and from HEA100 to HEA600, respectively. In both cases, the profiles were sorted in the ascending order of the moment of inertia about the sections' strong axis, assigning the ID = 1 to the profiles IPE100 and HEA100, which have the smallest value of each group. The profiles

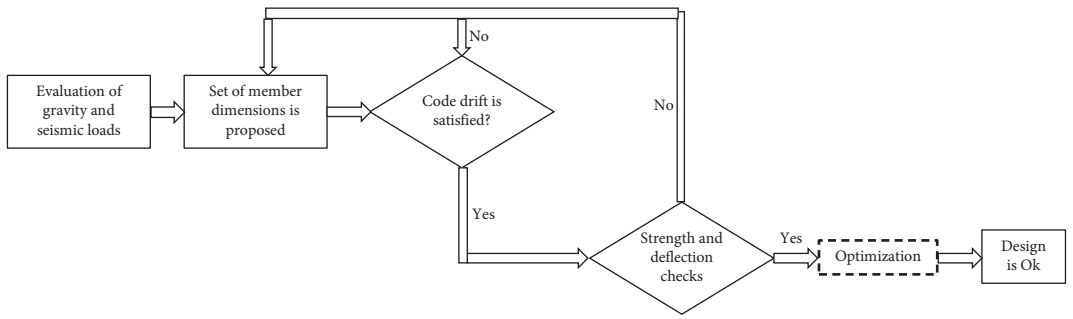

Figure 1: Typical design process of steel moment resisting frames. The dotted box represents the eigenfrequency optimization step proposed in this article.

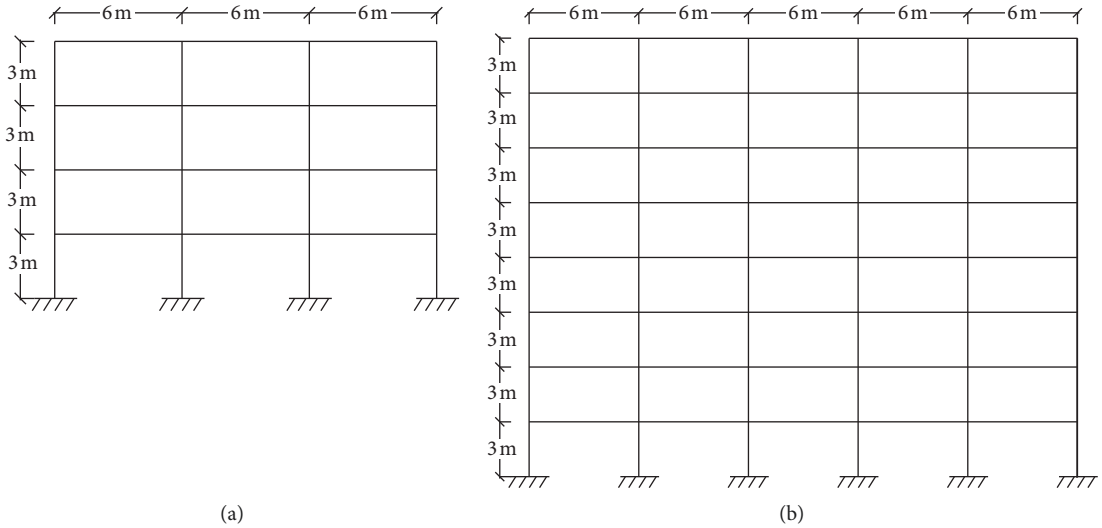

Figure 2: Structures to be optimized. (a) 4-story SMRF. (b) 8-story SMRF.

Table 1: Sections for beams.

Profile	ID	Area (cm^2)	Inertia (strong axis) (cm^4)
IPE100	1	10.3	171.1
IPE120	2	13.2	318.0
IPE140	3	16.4	541.1
IPE160	4	20.1	869.5
IPE180	5	23.9	1317.0
IPE200	6	28.5	1943.0
IPE220	7	33.4	2772.1
IPE240	8	39.1	3892.2
IPE270	9	45.9	5790.2
IPE300	10	53.8	8355.8
IPE330	11	62.6	11770.2
IPE360	12	72.7	16270.1
IPE400	13	84.5	23130.0
IPE450	14	98.8	33740.1
IPE500	15	116.0	48200.0
IPE550	16	134.0	67119.8
IPE600	17	156.0	92080.0

with the largest moment of inertia (IPE600 for beams and HEA600 for columns) had ID = 17 and ID = 19 assigned. This sorting is conducted to use the ID profiles of columns and beams that constitute the **p** vector described in the previous section, which is the optimization variable for the problem.

For both buildings, the objective function and constraints were coded in MATLAB® and the multiobjective evolutionary algorithm, Borg-MOEA [24] was used to solve the problem.

3.1. Results for the 4-Story Building. The proposed method (Figure 1) is applied to a four-story building (Figure 2(a)). This building is first designed according to the customary engineering practice for a base shear of 161.5 kN. The design results show that using profiles ID = 11 (HEA300) and ID = 10 (IPE100) for columns and beams satisfy all the drift, strength, and deflexion requirements. This design has a mass of 7.28 ton, which is used as the W_0 limit for the problem formulation. Since this is a low-rise building, the fundamental frequency was considered as the only objective function.

A key step to formulate the optimization problem is defining the first constraint and choosing suitable values for $p_{i,\min}$ and $p_{i,\max}$. As discussed in the previous section, these must be chosen such that the resulting optimized design complies with the resistance and functionality requirements

Table 2: Sections for columns.

Profile	ID	Area (cm^2)	Inertia (strong axis) (cm^2)
HEA100	1	21.2	349.2
HEA120	2	25.3	606.0
HEA140	3	31.4	1033.1
HEA160	4	38.8	1672.8
HEA180	5	45.3	2509.9
HEA200	6	53.8	3692.0
HEA220	7	64.3	5410.2
HEA240	8	76.8	7763.1
HEA260	9	86.8	10449.9
HEA280	10	97.3	13669.9
HEA300	11	112.5	18260.1
HEA320	12	124.4	22930.2
HEA340	13	133.5	27689.8
HEA360	14	142.8	33090.0
HEA400	15	159.0	45070.0
HEA450	16	178.0	63720.0
HEA500	17	197.5	86969.9
HEA550	18	211.8	111900.1
HEA600	19	226.5	141199.9

of the design code. For $p_{i,\min}$, a good strategy for beams is selecting the smallest profile that satisfies the serviceability (deflexion) requirements of the design code. One way to conduct this task is analyzing the floor system for the gravity loads and finding the profile for which the deflexions are closest to the code limit for the building. In this example, beam ID = 9 (IPE270) satisfies the strength and deflexion requirements; hence, they are used as the $p_{i,\min}$.

For columns, $p_{i,\min}$ must be selected simultaneously with the beams $p_{i,\max}$, ensuring that the strong column-weak beam requirement is met. In this example, column ID = 10 (HEA280) and beam ID = 11 (IPE330) are selected for the columns $p_{i,\min}$ and beams $p_{i,\max}$. Based on engineering experience and to avoid having an unnecessary large space, ID = 12 (HEA320) and is set as the upper bounds for columns (i.e., $p_{i,\max}$).

Table 3 shows the results of the building design per the traditional method and the one proposed in this article. This result was achieved using the Borg algorithm configured to perform 1000000 function evaluations, which required 21 minutes of computing time running on a single core of a Ryzen 7 1700 processor at 3.4 GHz. To ascertain the convergence of the Borg algorithm, this process was repeated five times with different seed values, obtaining the same results.

The results (Table 3) show that the proposed method did not change the building's beam configuration, leaving all floors with the initial ID = 10 (IPE300) profile. This result may stem from the additional constraint imposed to the objective function that beams within a same floor must use the same section profile. This constraint was included to accommodate construction practices, where it is common for all beams within a same floor to use the same section. Regarding columns, the method assigns ID = 12 (HEA320) sections to columns of the first two stories and ID = 10 (HEA280) to columns in the top half of the building. The material consumption for this building is 7.22 ton, a 0.8% reduction compared to the traditional alternative. In terms

Table 3: Design results for the 4-story building.

Story	Traditional design		Optimized design	
	Column ID	Beam ID	Column ID	Beam ID
1	11	10	12	10
2	11	10	12	10
3	11	10	10	10
4	11	10	10	10

of ratio of the column inertia to beam inertia, column ID = 12 to beam ID = 10 in the first two floors of the optimized design is 2.74, a 25% increase compared to the 2.18 in the traditional design. On the other hand, for floors 3 and 4, this ratio decreases to 1.63. In all cases, these ratios satisfy the code constraints.

3.2. Results for the 8-Story Building. The application of the proposed method to the 8-story building (Figure 2(b)) has one important difference compared to the 4-story building. Being a midrise building that has twice the stories and two additional beam spans compared to the four-story building, selecting only one frequency as objective function may not be the most appropriate option, as it could neglect the potential impacts of higher frequencies on the building seismic performance. Consequently, the first two frequencies are selected as objective functions, turning this into a multiobjective optimization problem.

Like the four-story building, the first step is to design the building according to the customary engineering practice. This building was designed for a base shear of 755 kN. The section profiles that satisfy all design code requirements for this building are ID = 17 (HEA500) for columns and ID = 11 (IPE330) for beams. This initial design has a mass of 34.1 ton that is used to calculate W_0 for the optimization formulation (equation (1)).

To define the section constraints of the optimization problem, the smallest profile that satisfies the deflexion requirement for beams is ID = 100 (IPE300); hence, it is used to define the beams' $p_{i,\min}$. For the upper limit for beams, ($p_{i,\max}$) ID = 13 (IPE400) is selected, together with ID = 15 (HEA400) as $p_{i,\min}$ for columns. These profiles ensure that the column-to-beam inertia ratio of the building is at least 1.95. Lastly, profile ID = 19 (HEA600) is selected as the upper bound for the column size.

The optimization results obtained using the Borg-MOEA [24] algorithm after 1000000 function evaluations are shown in Table 4. Since the problem has two objectives, it does not have a single solution. Instead, the optimization provides a set of designs which are the nondominant solutions of the problem. This means that each solution has one frequency smaller when individually compared to the others. For instance, solution 1 has a smaller w_1 than solution 3, but w_2 is smaller for the solution 3 compared to solution 1.

The analysis of the designs allows identification of a heightwise pattern for the structural elements. In terms of the columns configuration, all designs start with section ID = 19 (HEA600) at the bottom two stories of the building, which is the section profile with the largest moment of

Table 4: Design results for the 8-story building.

Story	Traditional		Solution 1		Solution 2		Solution 3		Solution 4	
	Col. ID	Beam ID	Col. ID	Beam ID	Col. ID	Beam ID	Col. ID	Beam ID	Col. ID	Beam ID
1	17	11	19	12	19	12	19	12	19	12
2	17	11	19	11	19	10	19	10	19	10
3	17	11	17	10	18	10	17	10	17	10
4	17	11	17	10	17	10	17	10	17	10
5	17	11	17	10	17	10	17	11	17	10
6	17	11	17	13	17	13	17	13	17	13
7	17	11	17	10	17	10	17	10	17	11
8	17	11	15	10	15	10	15	10	15	10

inertia. After that, the section is reduced to ID = 17 (HEA500) in solutions 1, 3, and 4 between the third and seventh story and further reduced to ID = 15 (HE400) at the eighth story. Solution 2 has a slight difference, using ID = 18 instead of ID = 17 at the third story. Regarding beams configuration, the four designs have beam ID = 12 (IPE360) at the bottom and ID = 13 (IPE400) at the sixth story, with one story with ID = 11 (IPE300) and the remaining stories with ID = 10 (IPE300).

3.3. Computational Performance. As stated in the Introduction section, the novelty of the method lies on the problem formulation based on eigenfrequency optimization, which offers important benefits in terms of computational performance. These are achieved without incorporating improvements and/or innovations in the solution technique. For the two buildings used as example, the results were obtained using the Borg-MOEA [24] algorithm, which is a state-of-the-art method to solve multiobjective optimization problems. Nevertheless, the formulation lends itself to other solution techniques based on evolutionary algorithms.

For the 5-story building, 21 minutes of computational time using one core of a Ryzen 7 1700 processor were necessary to obtain a solution. For the 8-story building, it took 42 minutes with the same conditions, with a total of 1000000 function evaluations. These computational times compare favorably to others reported in literature, where for two-dimensional problems, it may take between 12 hours and 1.5 weeks depending on the problem formulation [35].

In terms of convergence, the proposed method in combination with the Borg-MOEA algorithm showed a good performance. This was measured for the four-story and the eight-story buildings by selecting five different sets of initial population to start the searching process. In all cases, the same result was obtained, regardless of the starting point. Since the novelty of the proposed method relies on its formulation, the computational efficiency, and ease of formulation which it confers to the optimization problem, no further tests were conducted as the Borg-MOEA is an algorithm that has been used to solve more complex problems [36, 37].

3.4. Application of the Method for Three-Dimensional Buildings. As discussed previously, the formulation of the proposed method also works for three-dimensional buildings. However, there are two important considerations. The first one is that three-dimensional problems require the use of an appropriate stiffness matrix, where each element end must have 6 degrees of freedom. In this regard, the authors recommend using the Timoshenko stiffness matrix. Correspondingly, the mass matrix must account for the additional degrees of freedom. The strength, ductility, and capacity requirements of design codes can be met by proper selection of the $p_{i,\min}$ and the $p_{i,\max}$, as demonstrated in the examples above.

The second consideration is the selection of the number of frequencies. Due to the almost unlimited number of possible three-dimensional buildings, it is not easy to provide a thumb-rule to select the number of frequencies. Nonetheless, the authors recommend a similar approach to the one used by design codes to select the number of modes in a response spectrum analysis, ensuring that number of modes achieves a minimum percentage of the building mass.

4. Seismic Performance Evaluation

In order to have a comprehensive view of the implications of the proposed method in the seismic performance, OpenSees [25] was used to create fiber models for the traditionally designed buildings design and the ones designed with the proposed method. Beam and columns are modeled using force-based elements with fibers of steel. The model uses five integration points, with the steel modeled considering $E_s = 200$ GPa, $F_y = 350$ MPa, $F_u = 450$ MPa, and a rupture deformation $\varepsilon_{rup} = 14\%$. The foundation is modeled as rigid, and the gravity loads for the model are calculated based on the expected loads and using the combination $1.05D + 0.25L$. Corotational effects are included to account for contribution of the geometric stiffness matrix at large deformations. The seismic performance is evaluated using pushover analysis through displacement control, with a load pattern proportional to the first mode of vibration of the building. The buildings are pushed to a 10% roof drift ratio (i.e., the ratio between roof displacement and the buildings height) in 1 mm increments.

4.1. Evaluation of the 4-Story Building. The pushover results for the traditionally designed building and the building designed per the proposed method are shown in Figure 3. The X-axis shows the roof drift ratio (RDR) of the buildings

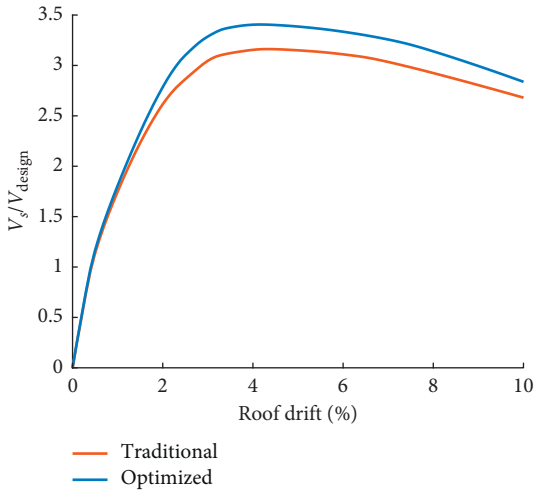

Figure 3: Pushover results for the four-story buildings.

as percent, and the Y-axis shows the ratio (V_s/V_{design}) between the base shear V_s in the pushover and the design base shear V_{design} of the building.

The results from this analysis show that the buildings have almost identical performance up to 1.5% roof drift, suggesting that the seismic performance for small earthquakes will be similar. After this point, the building designed per the proposed method shows better performance, exhibiting a higher overstrength (maximum V_s/V_{design}). On the other hand, both buildings have similar values for the postpeak slope. To further investigate the seismic performance improvements of the proposed method, the SPO2-FRAG software [38] is used to generate fragility functions at the life safety (3% RDR) and the collapse fragility (4.5% RDR) levels.

Compared to the traditionally designed building, the seismic performance at the life safety and collapse levels for the building designed following the procedure presented is improved. An acceleration Sa = 0.625 g is required for a 10% of probability of exceedance for the traditionally designed building at the collapse prevention level. For the building designed according to the method herein proposed, Sa = 0.70 g ($T1$ = 0.94 s) is needed to reach this probability, representing a 12% increase. The results for the life safety level (Figure 4) show similar improvements in the building designed following the proposed method. Considering again, a 10% of exceedance probability and an acceleration Sa = 0.50 g is needed for this building, which is 10.2% higher than in its traditionally designed counterpart (0.454 g).

Summing up the results for this case, the building designed according to the proposed method has improved performance over the traditional one at the life safety and the collapse prevention levels. These benefits come without any additional costs in materials and were achieved after less than 30 minutes of computational time.

4.2. Evaluation of the 8-Story Building. The pushover results for the 8-story traditionally designed building and the four designs obtained using the proposed method are shown in Figure 5.

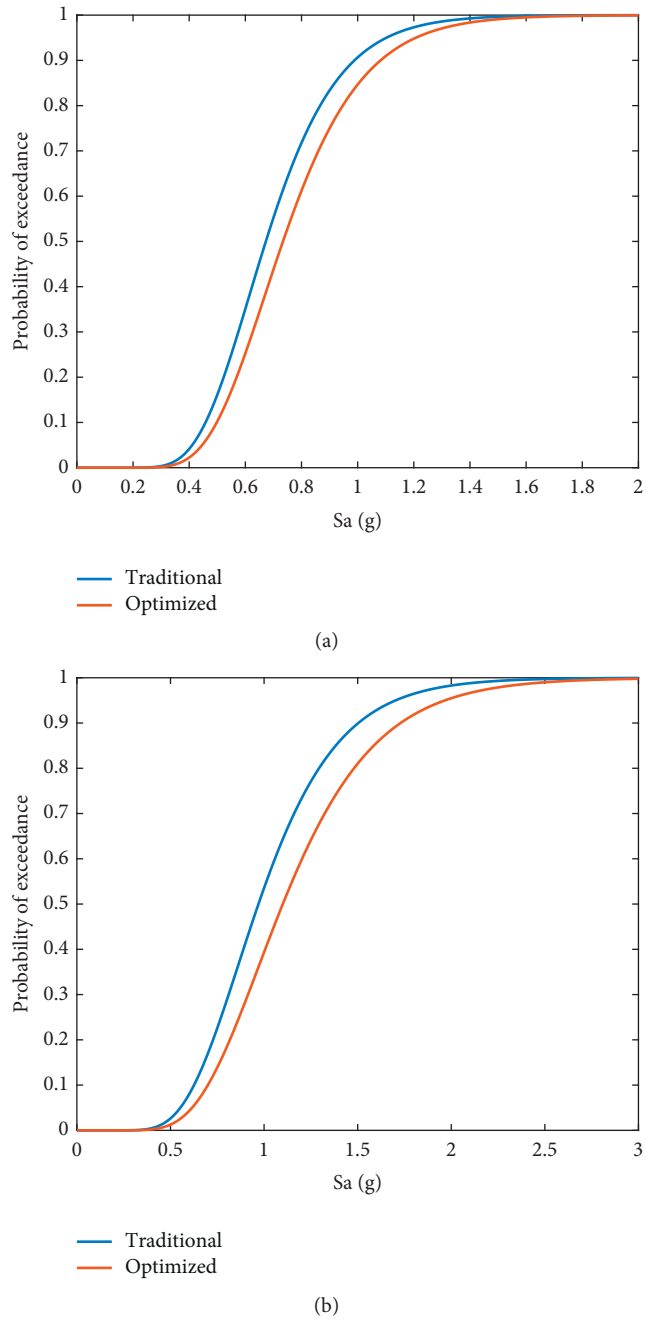

Figure 4: Results for the (a) life safety and (b) collapse fragility functions.

Several observations can be drawn from these results. To start, all the buildings designed per the proposed method have a higher overstrength ratio (largest V_s/V_{design} value) than the traditional design. In addition, these four buildings reach this value close to a 3.5% RDR, which is also higher than the 3.1% RDR at which it occurs for the traditional building. Comparing the four designs obtained per the proposed method, solutions 1, 2, and 4 show similar performance levels, as demonstrated by their almost overlapping pushover curves. On the other hand, the

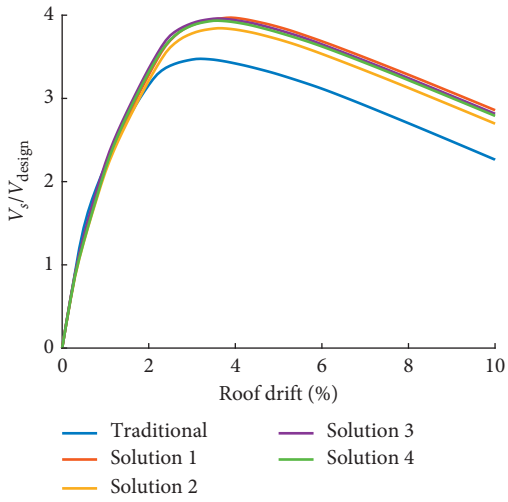

Figure 5: Pushover results for the eight-story buildings.

performance observed for solution 2 is slightly worse, albeit by small margin. When RDR smaller than 1.5% is considered, the behaviour observed for all buildings is similar, suggesting that they will exhibit similar performance when subjected to small earthquakes.

Overall, the pushover results for the eight-story building show similar benefits to those observed for the 4-story building. Moreover, the improvements for the overstrength ratio and its associated RDR are slightly higher than the ones in the four-story building, suggesting that the use of two frequencies as objective functions instead of one has brought better solutions. These findings support the argument that the designs obtained for the eight-story building will have similar or better improvements compared with the traditional design in the life safety and collapse fragility.

5. Conclusions and Future Work

A method to design steel moment resisting frames has been proposed based on eigenfrequency optimization. Compared to existing alternatives, the proposed method has the advantages of being computationally efficient and feasible to implement. These benefits stem from the fact that the method uses the information of elastic models of the buildings. The application of the method is demonstrated for a four-story and an eight-story building, whose seismic performance is evaluated using nonlinear fiber models which are used to develop seismic fragility functions. The findings of this study support the following conclusions:

(1) The proposed method produces designs of steel moment frames that have superior seismic performance than buildings designed following the customary engineering practice. The results from the seismic performance for a four-story building show that the building designed using the proposed method is 12% less susceptible to collapse than its traditionally designed counterpart.

(2) The method is computationally efficient, as it allowed us to obtain a design in less than half hour of computing time for the four-story building and in less than one hour for the eight-story building. In addition, since the method uses elastic models, it is feasible to implement by practicing engineers without major efforts, suggesting that it can be integrated in the design workflow of engineering offices.

(3) Eigenfrequency optimization is a viable framework to optimize the design of steel moment frames, which lends itself to be implemented and solved using evolutionary approaches like genetic algorithms.

(4) The method can be used for buildings with more complex dynamic responses as it allows incorporation of more than one natural frequency as objective function. The application for an eight-story building suggests that this practice may bring additional benefits in the seismic performance compared to when only one frequency is considered. For this building, the pushover results show that the designs that result from the method application have higher overstrength than the traditional design. In addition, they also showed that the postpeak range starts at a larger roof drift ratio than in the traditional design.

The buildings used to demonstrate the application of the method in this study were regular buildings, whose elevation can be represented by two-dimensional frames. However, the proposed method can also be used to optimize the seismic design of three-dimensional buildings with minimal changes compared to two-dimensional buildings. The implementation details and recommendations are also provided in this work.

Future research on this topic can be pursued in several topics. One interesting area is evaluating the benefits of the proposed method for other building configurations, particularly for high-rise buildings where several frequencies are needed to capture the dynamic response and which would be required as objective functions. Considering the potential to be a computationally efficient method, it is a worthy topic to investigate the method application to optimize three-dimensional buildings with different types of irregularities. Finally, it is worth exploring the potential benefits of using other solution techniques such as simulated annealing, ant colony, and a wide family of evolutionary algorithms instead of the genetic algorithms used in this work.

Data Availability

No data from third party sources were used to support this study. The results obtained come from numerical simulations conducted by the authors.

Conflicts of Interest

The authors declare that there are no conflicts of interest regarding the publication of this paper.

Acknowledgments

The authors appreciate the support of the "División de Investigación" at Universidad de La Sabana for providing the financial support for this manuscript.

References

[1] A. Y. Elghazouli, "Assessment of European seismic design procedures for steel framed structures," *Bulletin of Earthquake Engineering*, vol. 8, no. 1, pp. 65–89, 2010.

[2] M. Ferraioli, A. Lavino, and A. Mandara, "Behaviour factor of code-designed steel moment-resisting frames," *International Journal of Steel Structures*, vol. 14, no. 2, pp. 243–254, 2014.

[3] R. Landolfo, "Seismic design of steel structures: new trends of research and updates of eurocode 8," in *Recent Advances in Earthquake Engineering in Europe*, vol. 46, pp. 413–438, Springer, Cham, Switerzland, 2018.

[4] M. P. Saka and Z. W. Geem, "Mathematical and metaheuristic applications in design optimization of steel frame structures: an extensive review," *Mathematical Problems in Engineering*, vol. 2013, Article ID 271031, 33 pages, 2013.

[5] M. Fragiadakis and N. D. Lagaros, "An overview to structural seismic design optimisation frameworks," *Computers & Structures*, vol. 89, no. 11-12, pp. 1155–1165, 2011.

[6] M. Liu, S. A. Burns, and Y. K. Wen, "Multiobjective optimization for performance-based seismic design of steel moment frame structures," *Earthquake Engineering & Structural Dynamics*, vol. 34, no. 3, pp. 289–306, 2005.

[7] V. Toğan, "Design of planar steel frames using teaching–learning based optimization," *Engineering Structures*, vol. 34, pp. 225–232, 2012.

[8] A. Kaveh and S. Talatahari, "An improved ant colony optimization for the design of planar steel frames," *Engineering Structures*, vol. 32, no. 3, pp. 864–873, 2010.

[9] S. O. Degertekin, "Harmony search algorithm for optimum design of steel frame structures: a comparative study with other optimization methods," *Structural Engineering and Mechanics*, vol. 29, no. 4, pp. 391–410, 2008.

[10] İ. Aydoğdu, A. Akın, and M. P. Saka, "Design optimization of real world steel space frames using artificial bee colony algorithm with Levy flight distribution," *Advances in Engineering Software*, vol. 92, pp. 1–14, 2016.

[11] A. Kaveh and A. BolandGerami, "Optimal design of large-scale space steel frames using cascade enhanced colliding body optimization," *Structural and Multidisciplinary Optimization*, vol. 55, no. 1, pp. 237–256, 2017.

[12] S. Gholizadeh and H. Poorhoseini, "Seismic layout optimization of steel braced frames by an improved dolphin echolocation algorithm," *Structural and Multidisciplinary Optimization*, vol. 54, no. 4, pp. 1011–1029, 2016.

[13] S. Gholizadeh, "Performance-based optimum seismic design of steel structures by a modified firefly algorithm and a new neural network," *Advances in Engineering Software*, vol. 81, pp. 50–65, 2015.

[14] A. Kaveh, T. Bakhshpoori, and M. Azimi, "Seismic optimal design of 3D steel frames using cuckoo search algorithm," *Structural Design of Tall and Special Buildings*, vol. 24, no. 3, pp. 210–227, 2015.

[15] S. Günay and K. M. Mosalam, "PEER performance-based earthquake engineering methodology, revisited," *Journal of Earthquake Engineering*, vol. 17, no. 6, pp. 829–858, 2013.

[16] D. R. Sahoo and S.-H. Chao, "Performance-based plastic design method for buckling-restrained braced frames," *Engineering Structures*, vol. 32, no. 9, pp. 2950–2958, 2010.

[17] N. Wongpakdee, S. Leelataviwat, S. C. Goel, and W.-C. Liao, "Performance-based design and collapse evaluation of buckling restrained knee braced truss moment frames," *Engineering Structures*, vol. 60, pp. 23–31, 2014.

[18] C.-X. Qiu and S. Zhu, "Performance-based seismic design of self-centering steel frames with SMA-based braces," *Engineering Structures*, vol. 130, pp. 67–82, 2017.

[19] Z. Liu, S. Atamturktur, and C. H. Juang, "Performance based robust design optimization of steel moment resisting frames," *Journal of Constructional Steel Research*, vol. 89, pp. 165–174, 2013.

[20] Z. Liu, S. Atamturktur, and C. H. Juang, "Reliability based multi-objective robust design optimization of steel moment resisting frame considering spatial variability of connection parameters," *Engineering Structures*, vol. 76, pp. 393–403, 2014.

[21] ASCE Task Committee on Performance Based Design, *Advocating for Performance Based Design*, Structural Engineering Institute, St. Louis, MO, USA, 2018, https://www.asce.org/uploadedFiles/Technical_Areas/Structural_Engineering/Content_Pieces/2018-sei-advocating-for-performance-based-design-report.pdf.

[22] M. Head, S. Dennins, S. Muthukumar, B. Nielson, and K. Mackie, "Structure magazine | nonlinear analysis in modern earthquake engineering practice," 2014, http://www.structuremag.org/?p=1666.

[23] O. Arroyo and A. B. Liel, "A call to refocus research goals for the development of seismic optimization methods," *Earthquake Spectra*, vol. 33, no. 3, pp. 1029–1031, 2017.

[24] D. Hadka and P. Reed, "Borg: an auto-adaptive many-objective evolutionary computing framework," *Evolutionary Computation*, vol. 21, no. 2, pp. 231–259, 2013.

[25] F. McKenna, "OpenSees: a framework for earthquake engineering simulation," *Computing in Science & Engineering*, vol. 13, no. 4, pp. 58–66, 2011.

[26] G. Allaire, S. Aubry, and F. Jouve, "Eigenfrequency optimization in optimal design," *Computer Methods in Applied Mechanics and Engineering*, vol. 190, no. 28, pp. 3565–3579, 2001.

[27] T. D. Tsai and C. C. Cheng, "Structural design for desired eigenfrequencies and mode shapes using topology optimization," *Structural and Multidisciplinary Optimization*, vol. 47, no. 5, pp. 673–686, 2013.

[28] D.-K. Lee, C.-J. Yang, and U. Starossek, "Topology design of optimizing material arrangements of beam-to-column connection frames with maximal stiffness," *Scientia Iranica*, vol. 19, no. 4, pp. 1025–1032, 2012.

[29] A. Senba, K. Oka, M. Takahama, and H. Furuya, "Vibration reduction by natural frequency optimization for manipulation of a variable geometry truss," *Structural and Multidisciplinary Optimization*, vol. 48, no. 5, pp. 939–954, 2013.

[30] O. Arroyo, V. Prieto, and S. Gutiérrez, "Method to improve seismic performance of RC moment-resisting frames using geometric optimization," *Journal of Computing in Civil Engineering*, vol. 30, no. 3, article 04015046, 2016.

[31] A. K. Chopra and R. K. Goel, "A modal pushover analysis procedure for estimating seismic demands for buildings," *Earthquake Engineering & Structural Dynamics*, vol. 31, no. 3, pp. 561–582, 2002.

[32] A. K. Chopra, R. K. Goel, and C. Chintanapakdee, "Evaluation of a modified MPA procedure assuming higher modes as

elastic to estimate seismic demands," *Earthquake Spectra*, vol. 20, no. 3, pp. 757–778, 2004.

[33] American Society of Civil Engineers, *Minimum Design Loads for Buildings and Other Structures*, American Society of Civil Engineers, Reston, VA, USA, 2013.

[34] American Society of Civil Engineers, *Seismic Rehabilitation of Existing Buildings (ASCE/SEI 41-06)*, American Society of Civil Engineers, Reston, VA, USA, 2006.

[35] A. E. Zacharenaki, M. Fragiadakis, and M. Papadrakakis, "Reliability-based optimum seismic design of structures using simplified performance estimation methods," *Engineering Structures*, vol. 52, pp. 707–717, 2013.

[36] P. M. Reed and D. Hadka, "Evolving many-objective water management to exploit exascale computing," *Water Resources Research*, vol. 50, no. 10, pp. 8367–8373, 2014.

[37] D. Hadka and P. Reed, "Large-scale parallelization of the Borg multiobjective evolutionary algorithm to enhance the management of complex environmental systems," *Environmental Modelling & Software*, vol. 69, pp. 353–369, 2015.

[38] G. Baltzopoulos, R. Baraschino, I. Iervolino, and D. Vamvatsikos, "SPO2FRAG: software for seismic fragility assessment based on static pushover," *Bulletin of Earthquake Engineering*, vol. 15, no. 10, pp. 4399–4425, 2017.

Hindawi
Advances in Civil Engineering
Volume 2019, Article ID 8912390, 10 pages
https://doi.org/10.1155/2019/8912390

Research Article

Improving the Structural Reliability of Steel Frames Using Posttensioned Connections

Edén Bojórquez,[1] **Arturo López-Barraza**,[1] **Alfredo Reyes-Salazar**,[1] **Sonia E. Ruiz**,[2] **Jorge Ruiz-García**,[3] **Antonio Formisano**,[4] **Francisco López-Almansa**,[5] **Julián Carrillo**,[6] **and Juan Bojórquez**[1]

[1]*Facultad de Ingeniería, Universidad Autónoma de Sinaloa, Culiacán 80040, Mexico*
[2]*Instituto de Ingeniería, Universidad Nacional Autónoma de México, México City 04510, Mexico*
[3]*Facultad de Ingeniería Civil, Universidad Michoacana de San Nicolás de Hidalgo, Morelia 58040, Mexico*
[4]*Department of Structures for Engineering and Architecture (DiSt), University of Naples "Federico II", Naples 80125, Italy*
[5]*Architecture Technology Department, Technical University of Catalonia, Barcelona 08028, Spain*
[6]*Ingeniería Civil, Universidad Militar Nueva Granada, Bogotá, Colombia*

Correspondence should be addressed to Edén Bojórquez; eden@uas.edu.mx

Received 23 March 2019; Accepted 2 June 2019; Published 26 June 2019

Academic Editor: Rosario Montuori

In this paper, various moment-resisting steel frames (MRSFs) are subjected to 30 narrow-band motions scaled at different ground motion intensity levels in terms of spectral acceleration at first mode of vibration $S_a(T_1)$ in order to perform incremental dynamic analysis for peak and residual interstory drift demands. The results are used to compute the structural reliability of the steel frames by means of hazard curves for peak and residual drifts. It is observed that the structures exceed the threshold residual drift of 0.5%, which is perceptible to human occupants, and it could lead to human discomfort according to recent investigations. For this reason, posttensioned connections (PTCs) are incorporated into the steel frames in order to improve the structural reliability. The results suggest that the annual rate of exceedance of peak and residual interstory drift demands are reduced with the use of PTC. Thus, the structural reliability of the steel frames with PTC is superior to that of the MRSFs. In particular, the residual drift demands tend to be smaller when PTCs are incorporated in the steel structures.

1. Introduction

Currently, most of the seismic design regulations recommend the use of maximum interstory drift as the main engineering demand parameter. Nevertheless, earthquake field reconnaissance has evidenced that residual drift demands after an earthquake play an important role in the seismic performance of a structure. For example, several dozen damaged reinforced concrete structures in Mexico City had to be demolished after the 1985 Michoacan earthquake because of the technical difficulties to straighten and to repair buildings with large permanent drifts [1]. Okada et al. [2] reported that several low-rise RC buildings suffered light structural damage but experienced relatively large residual deformations as a consequence of the 1995 Hyogo-Ken Nambu earthquake even though they had sufficient deformation capacity. After examining 12 low-to-mid-rise steel office buildings (particularly 10 with structural system based on steel moment-resisting frames) structurally damaged and leaned after the same earthquake, Iwata et al. [3] highlighted that the cost of repair of leaned steel buildings linearly increased as the maximum and roof residual drift increased. Based on their study, the authors suggested that steel buildings should be limited to maximum and roof residual drift about 1.4% and 0.9%, respectively, to satisfy a repairability limit state that meets both technical and economical constraints. More recently, a field investigation in Japan indicated that a residual interstory drift of about 0.5% is perceptible for building occupants [4]. Bojórquez and Ruiz-García [5] by comparing peak and residual drift demand hazard curves have observed that if steel

frames exhibit peak drift demands about 3%, they could experience residual drifts larger than 0.5%, which is the threshold residual drift that could be tolerable to human occupants, and it could lead to human discomfort [4] when subjected to narrow-band earthquake ground motions of high intensity. Therefore, several researchers have demonstrated that the estimation of residual drift demands should also play an important role during the design of new buildings [6–8] and the evaluation of the seismic structural performance of existing buildings [9–13].

In the present study, motivated by the need to reduce peak and residual interstory drift demands, PTCs are incorporated into various MRSFs. Posttensioned steel moment-resisting frames are structural systems proposed in recent years as an appropriate alternative to welded connections of moment-resisting frames in seismic zones [14–27]. They are designed to prevent brittle fractures in the area of the nodes of steel frames, which can cause severe reduction in their ductility capacity, as occurred in many cases during the 1994 Northridge and the 1995 Kobe earthquakes. The philosophy of structures with PTC is that under an intense earthquake motion, beams and columns remain essentially elastic concentrating the damage on the energy dissipating elements, which can be easily replaced at low cost. Moreover, they provide capacity of energy dissipation and self-centering which can significantly reduce the residual demands. The structural performance of the selected MRSFs is compared with the structures with PTC through incremental dynamic analysis and the estimation of the structural reliability of the frames in terms of peak and residual interstory drift demands. With this aim, four MRSFs and the same structures with PTC (here named FPTC frames with posttensioned connections) are subjected to 30 long-duration ground motions recorded at the lake zone of Mexico City where most of the damages were found in buildings as a consequence of the 1985 Michoacan earthquake. In general, it is observed that the structural reliability of the steel frames with PTC is superior to that of the MRSFs. In particular, the residual drift demands tend to be smaller than 0.5% (which is perceptible for building occupants) when PTCs are incorporated into the steel structures.

2. Methodology

2.1. Structural Steel Frame Models. Two groups of four structural steel frame models are selected for the study. The first group of structures corresponding to moment-resisting steel frames was designed according to the Mexico City Building Design Provisions (MCSDPs) [28]. The buildings are assumed to be for office occupancy. They have 4, 6, 8, and 10 stories, and 3 bays, hereafter indicated as F4, F6, F8, and F10, respectively. The dimensions of the frames are shown in Figure 1. The beams and columns are A36 steel W sections. A bilinear hysteretic model for accounting the nonlinear material behavior with 3% of postyielding stiffness was considered for the analyses, and the damping used was 3% of critical. The fundamental periods of vibration (T_1) are 0.9, 1.07, 1.20, and 1.37 s, respectively. On the other hand, the FPTCs were designed in accordance with the recommendations proposed by Garlock et al. [21], which basically start

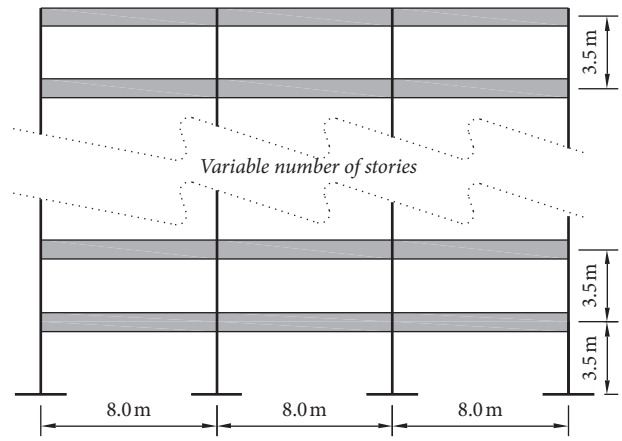

Figure 1: Geometrical characteristics of the MRSFs.

with the design of the steel frames as usually done (considering rigid connections), and then, the semirigid posttensioned connections are designed to satisfy the requirements of the serviceability and resistance conditions. The beam-column connections consist of two angles bolted to the flanges of the beam and to the column flange (top and seat). For the design of posttensioned connections, steel grade 50 was used for the angles. The length of the angles was taken equal to the width of the flange of the beams (b_f). Different angle sizes were tested, but at the end, $152 \times 152 \times 13$ mm angles were used in all the cases. Posttensioned cables consist of seven wires with an area of 150 mm^2, withstanding a load of 279 kN; they are parallel to the axis of the beam passing through the interior columns and fixed to the outer face of the columns at the ends of the frame. An initial tension of the cables less than 0.33 times their maximum capacity was used according with the suggestions given by Garlock et al. [21]. The four FPTC models are identified here as F4PTC, F6PTC, F8PTC, and F10PTC, for the frames with 4, 6, 8, and 10 stories, respectively. The FPTC models have fundamental periods of vibration of 0.89, 1.03, 1.25, and 1.37 s, respectively. The columns of the ground floor are fixed at the base without being posttensioned. The beam and column members used for all the frames are illustrated in Table 1. Note that the mechanical characteristics and dimensions of beams and columns are the same for both the MRSFs and FPTC. Figure 2 shows a typical assembly of a posttensioned steel frame.

2.2. Connection Model: Nonlinear Hysteretic Behavior. The hysteretic rules that represent the cyclic behavior of the semirigid connections of the posttensioned frames are characterized by moment-rotation curves (M-θ_r), with shapes similar to a flag. This representation characterizes the nonlinearity, self-centering capability, and energy dissipation capacity of the connection. Experimental tests with isolated angles, subjected to cyclic and monotonic loads, conducted by Shen and Astaneh-Asl [29] showed a stable cyclic response and good capability of hysteretic energy dissipation. In general, ultimate strength exceeded 3 times the yield strength, and ductility reached values between 8 and 10. The strength and stiffness in bending of the posttensioned connections is

Table 1: Relevant characteristics of the steel frames.

Frame	F4	F6	F8	F10
Number of stories	4	6	8	10
Internal columns				
Story 1	W21 × 122	W30 × 173	W36 × 210	W36 × 280
Story 2	W21 × 122	W30 × 173	W36 × 210	W36 × 280
Story 3	W21 × 111	W30 × 148	W36 × 194	W36 × 245
Story 4	W21 × 111	W30 × 148	W36 × 194	W36 × 245
Story 5		W30 × 124	W36 × 170	W36 × 210
Story 6		W30 × 124	W36 × 170	W36 × 210
Story 7			W36 × 160	W36 × 182
Story 8			W36 × 160	W36 × 182
Story 9				W36 × 150
Story 10				W36 × 150
External columns				
Story 1	W18 × 97	W27 × 146	W36 × 194	W36 × 280
Story 2	W18 × 97	W27 × 146	W36 × 194	W36 × 280
Story 3	W18 × 86	W27 × 129	W36 × 182	W36 × 245
Story 4	W18 × 86	W27 × 129	W36 × 182	W36 × 245
Story 5		W27 × 114	W36 × 160	W36 × 210
Story 6		W27 × 114	W36 × 160	W36 × 210
Story 7			W36 × 135	W36 × 182
Story 8			W36 × 135	W36 × 182
Story 9				W36 × 150
Story 10				W36 × 150
Beams				
Story 1	W16 × 67	W18 × 71	W21 × 83	W21 × 68
Story 2	W16 × 57	W18 × 76	W21 × 93	W21 × 93
Story 3	W16 × 45	W18 × 76	W21 × 93	W21 × 101
Story 4	W16 × 40	W16 × 67	W21 × 83	W21 × 101
Story 5		W16 × 50	W18 × 71	W21 × 101
Story 6		W16 × 45	W18 × 65	W21 × 93
Story 7			W18 × 55	W21 × 73
Story 8			W18 × 46	W21 × 68
Story 9				W21 × 57
Story 10				W21 × 50

provided by the contribution of the angles of the PTC and by posttensioned strands. Wires and angles work as springs in parallel. Posttensioned strands exhibit linear behavior, while connecting angles behave nonlinearly. Figure 3 shows a typical example of a hysteretic curve corresponding to a posttensioned connection. This behavior was modeled by mean of equations (1) and (2) which represent the loading and unloading curves, respectively, obtained from the superposition of the exponential equation proposed by Richard [30] for semirigid connections and the linear contribution of the strands, as well as decompression moments (M_d) and the closing moment (M_c) of the connection. The first function, given by equation (1), corresponds to the initial loading cycle; two types of variables are observed: (1) variables depending only on geometric and physical properties of angles, such as initial (k) and postyield (k_p) stiffnesses, the reference moment (M_o), and N that defines the curvature in the transition between the linear and plastic behavior and (2) variables depending on the number and type of tendons such as the rigidity of the posttensioned tendons ($k_{\theta S}$) and the bending moment associated with the opening of the connection (named decompression moment, M_d) which is a function of the resulting initial tension in the tendons. The second function, given by equation (2), defines the unloading and reloading process in the connection; M_a and θ_a are the maximum values reached in each cycle, and the parameter φ defines the magnitude of the closing moment of the connection (M_c), which must be greater than zero in order to insure complete closure of the connection after getting complete unloading; moreover, this parameter largely defines the E_H dissipation capacity of the connection (enclosed area). The curves obtained with the modified model exhibit good accuracy in comparison with experiment results, and they were modeled in RUAUMOKO [31] as the flag-shaped bilinear hysteresis [32].

$$M = M_d + \frac{\left(k - k_p\right)\theta_r}{\left[1 + \left|\left(\left(k - k_p\right)\theta_r\right)/M_o\right|^N\right]^{1/N}} + \left(k_p + k_{\theta S}\right)\theta_r, \tag{1}$$

$$M = M_a - \frac{\left(k - k_p\right)\left(\theta_a - \theta_r\right)}{\left[1 + \left|\left(\left(k - k_p\right)\left(\theta_a - \theta_r\right)\right)/\varphi M_o\right|^N\right]^{1/N}} - \left(k_p + k_{\theta S}\right)\left(\theta_a - \theta_r\right). \tag{2}$$

2.3. Earthquake Ground Motions. A total of 30 narrow-band earthquake ground motions recorded at soft soil sites of Mexico City are used for the time story analyses of the MSRF and FPTC. The main characteristic of the selected ground motions recorded on soft soils is that they demand large energy on structures in comparison to those recorded on firm soils [33, 34]. The ground motions were recorded in sites where the period of the soil was close to two seconds and structures were more severely damaged during the 1985 Mexico City Earthquake. The duration was computed according with Trifunac and Brady [35]. Table 2 summarizes the most important characteristics of the records. In the table, while PGA and PGV denote the peak ground acceleration and velocity, t_D indicates duration.

2.4. Evaluation of Structural Reliability. The incremental dynamic analysis [36] is used to assess the seismic performance of the steel frames under narrow-band motions at different intensity levels. Next, the well-known seismic performance-based assessment procedure suggested by the Pacific Earthquake Engineering Center [37] in the United States was employed in this study, which indicates that the mean annual frequency of exceedance of an engineering demand parameter (EDP) of interest exceeding a certain level EDP can be computed as follows:

$$\lambda\left(\mathrm{EDP} > \mathrm{edp}\right) \cong \int_{\mathrm{IM}} P\left[\mathrm{EDP} > \mathrm{edp} \mid \mathrm{IM} = \mathrm{im}\right] \cdot \left|d\lambda_{\mathrm{IM}}\left(\mathrm{im}\right)\right|, \tag{3}$$

where IM denotes the ground motion intensity measure (e.g., peak ground acceleration, spectral acceleration at the

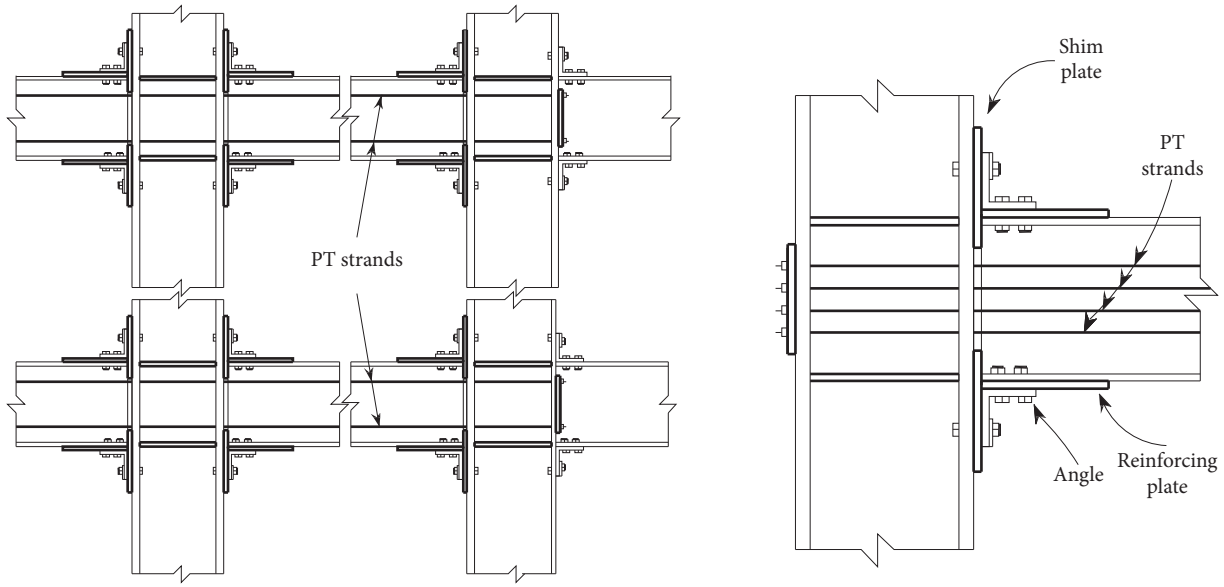

Figure 2: Angles and posttensioned strands in the FPTC structures.

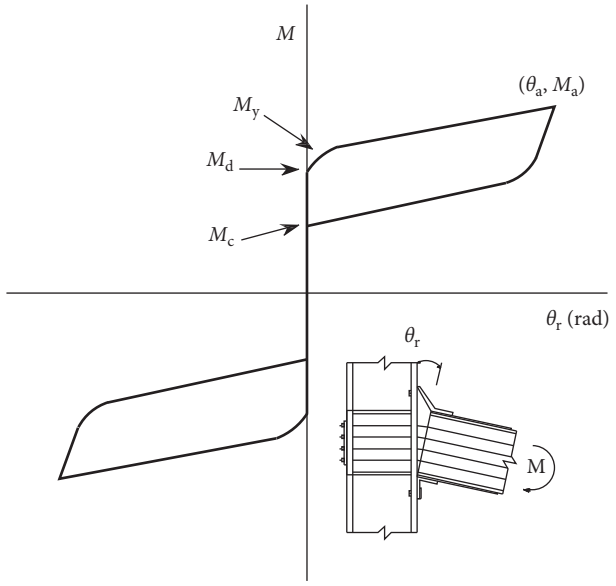

Figure 3: Moment-relative rotation hysteretic curve for the posttensioned connections.

first-mode period of vibration, and inelastic displacement demand at the building's fundamental period of vibration) and $P[\mathrm{EDP} > \mathrm{edp} \mid \mathrm{IM} = \mathrm{im}]$ is the conditional probability that an EDP exceeds a certain level of EDP given that the IM is evaluated at the ground motion intensity measure level im. In addition, $d\lambda_{\mathrm{IM}}(\mathrm{im})$ refers to the differential of the ground motion hazard curve for the IM. In this context, while the first term in the right-hand side of equation (3) can be obtained from probabilistic estimates of the EDP of interest with incremental dynamic analyses, the second term in equation (3) is represented by the seismic hazard curve, which can be computed from conventional Probabilistic Seismic Hazard Analysis (PSHA), evaluated at the ground motion intensity level im. Note the importance of the ground motion intensity measure for assessment of seismic performance, which is the joint between earthquake engineering and seismology. In this study, the spectral acceleration at first mode of vibration $S_a(T_1)$ was selected as IM, in such a way that equation (3) can be expressed as

$$\lambda(\mathrm{EDP} > \mathrm{edp}) \cong \int_{S_a(T_1)} P\left[\mathrm{EDP} > \mathrm{edp} \mid S_a(T_1) = s_a\right] \cdot \left|d\lambda_{S_a(T_1)}(s_a)\right|, \tag{4}$$

where $d\lambda_{S_a(T_1)}(s_a) = \lambda_{S_a(T_1)}(s_a) - \lambda_{S_a(T_1)}(s_a + ds_a)$ is the hazard curve differential expressed in terms of $S_a(T_1)$. Equation (4) was used to evaluate the structural reliability of the study-case frames in terms of two EDPs: peak and residual interstory drift demands. For evaluating the first term in the integrand for peak and residual drift demands, a lognormal cumulative probability distribution was used [5]. Therefore, the term $P(\mathrm{EDP} > \mathrm{edp} \mid S_a(T_1) = s_a)$ is analytically evaluated as follows:

$$P\left(\mathrm{EDP} > \mathrm{edp} \mid S_a(T_1) = s_a\right) = 1 - \Phi\left(\frac{\ln \mathrm{edp} - \widehat{\mu}_{\ln \mathrm{EDP} \mid S_a(T_1) = s_a}}{\widehat{\sigma}_{\ln \mathrm{EDP} \mid S_a(T_1) = s_a}}\right), \tag{5}$$

where $\widehat{\mu}_{\ln \mathrm{EDP} \mid S_a(T_1) = s_a}$ and $\widehat{\sigma}_{\ln \mathrm{EDP} \mid S_a(T_1) = s_a}$ are the geometric mean and standard deviation of the natural logarithm of the EDP, respectively, and $\Phi(\cdot)$ is the standard normal cumulative distribution function. It is important to say as Bojórquez et al. [38] indicate that the ground motion records used in the present study allow the use of spectral acceleration at first mode of vibration as intensity measure due to its sufficiency with respect to magnitude and distance and because of the similarity of the spectral shape of the records since they have similar values of the spectral parameter N_p [39].

2.5. Seismic Performance in terms of Peak and Residual Drift Demands: MRSFs vs Steel Frames with PTC. The first step to

Table 2: Narrow-band motions used for the present study.

Record	Date	Magnitude	Station	PGA (cm/s^2)	PGV (cm/s)	t_D (s)
1	19/09/1985	8.1	SCT	178.0	59.5	34.8
2	21/09/1985	7.6	Tlahuac deportivo	48.7	14.6	39.9
3	25/04/1989	6.9	Alameda	45.0	15.6	37.8
4	25/04/1989	6.9	Garibaldi	68.0	21.5	65.5
5	25/04/1989	6.9	SCT	44.9	12.8	65.8
6	25/04/1989	6.9	Sector popular	45.1	15.3	79.4
7	25/04/1989	6.9	Tlatelolco TL08	52.9	17.3	56.6
8	25/04/1989	6.9	Tlatelolco TL55	49.5	17.3	50.0
9	14/09/1995	7.3	Alameda	39.3	12.2	53.7
10	14/09/1995	7.3	Garibaldi	39.1	10.6	86.8
11	14/09/1995	7.3	Liconsa	30.1	9.62	60.0
12	14/09/1995	7.3	Plutarco Elías Calles	33.5	9.37	77.8
13	14/09/1995	7.3	Sector popular	34.3	12.5	101.2
14	14/09/1995	7.3	Tlatelolco TL08	27.5	7.8	85.9
15	14/09/1995	7.3	Tlatelolco TL55	27.2	7.4	68.3
16	09/10/1995	7.5	Cibeles	14.4	4.6	85.5
17	09/10/1995	7.5	CU Juárez	15.8	5.1	97.6
18	09/10/1995	7.5	Centro urbano Presidente Juárez	15.7	4.8	82.6
19	09/10/1995	7.5	Córdoba	24.9	8.6	105.1
20	09/10/1995	7.5	Liverpool	17.6	6.3	104.5
21	09/10/1995	7.5	Plutarco Elías Calles	19.2	7.9	137.5
22	09/10/1995	7.5	Sector popular	13.7	5.3	98.4
23	09/10/1995	7.5	Valle Gómez	17.9	7.18	62.3
24	11/01/1997	6.9	CU Juárez	16.2	5.9	61.1
25	11/01/1997	6.9	Centro urbano Presidente Juárez	16.3	5.5	85.7
26	11/01/1997	6.9	García Campillo	18.7	6.9	57.0
27	11/01/1997	6.9	Plutarco Elías Calles	22.2	8.6	76.7
28	11/01/1997	6.9	Est. # 10 Roma A	21.0	7.76	74.1
29	11/01/1997	6.9	Est. # 11 Roma B	20.4	7.1	81.6
30	11/01/1997	6.9	Tlatelolco TL08	16.0	7.2	57.5

evaluate the structural reliability is the computation of the incremental dynamic analysis; thus, the maximum or residual interstory drift at different values of the ground motion intensity measure which in the present study is $S_a(T_1)$ is calculated. Figure 4 illustrates as an example the incremental dynamic analysis of the traditional frame F4 under the selected narrow-band motions. It can be observed the increase of the maximum interstory drift as the spectral acceleration at first mode of vibration tends to increase. Likewise, notice that the uncertainty in the structural response also tend to increase for larger values of $S_a(T_1)$. Then, the fragility curves are computed through equation (5), which are combined with the seismic hazard curves to compute the mean annual rate of exceedance, thus the structural reliability via equation (4) in terms of peak and residual interstory drift. Note that in this case, the spectral acceleration hazard curves corresponding to the first-mode period of vibration of each building and for the *Secretaría de Comunicaciones y Transportes* (SCT) site in Mexico City were developed following the procedure suggested by Alamilla [40].

The Mexican City seismic design code takes into account the peak interstory drift. Recently, Bojórquez and Ruiz-García [5] demonstrated that, for MRSFs designed with the Mexican City Building Code, the control of maximum or peak interstory drift demands does not necessarily guarantee a good seismic performance in terms of residual drift demands. In fact, by comparing peak and residual drift demand hazard curves, Bojórquez and Ruiz-García [5] concluded that, for steel structures that exhibit peak drift demands of about 3% (the threshold recommended by the MCSDP to avoid collapse), the maximum residual drifts is larger than 0.5%, which is the threshold residual drift that could be tolerable to human occupants, and it could lead to human discomfort identified from recent field investigations [4] when subjected to narrow-band earthquake ground motions of high intensity. For this reason, the residual interstory drift should be considered in future versions of the

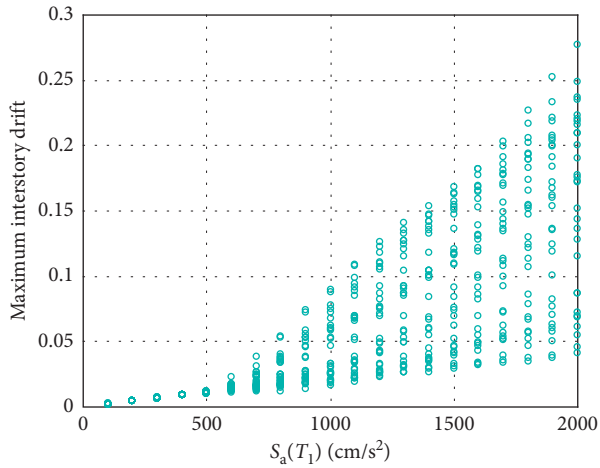

Figure 4: Incremental dynamic analysis of frame F4.

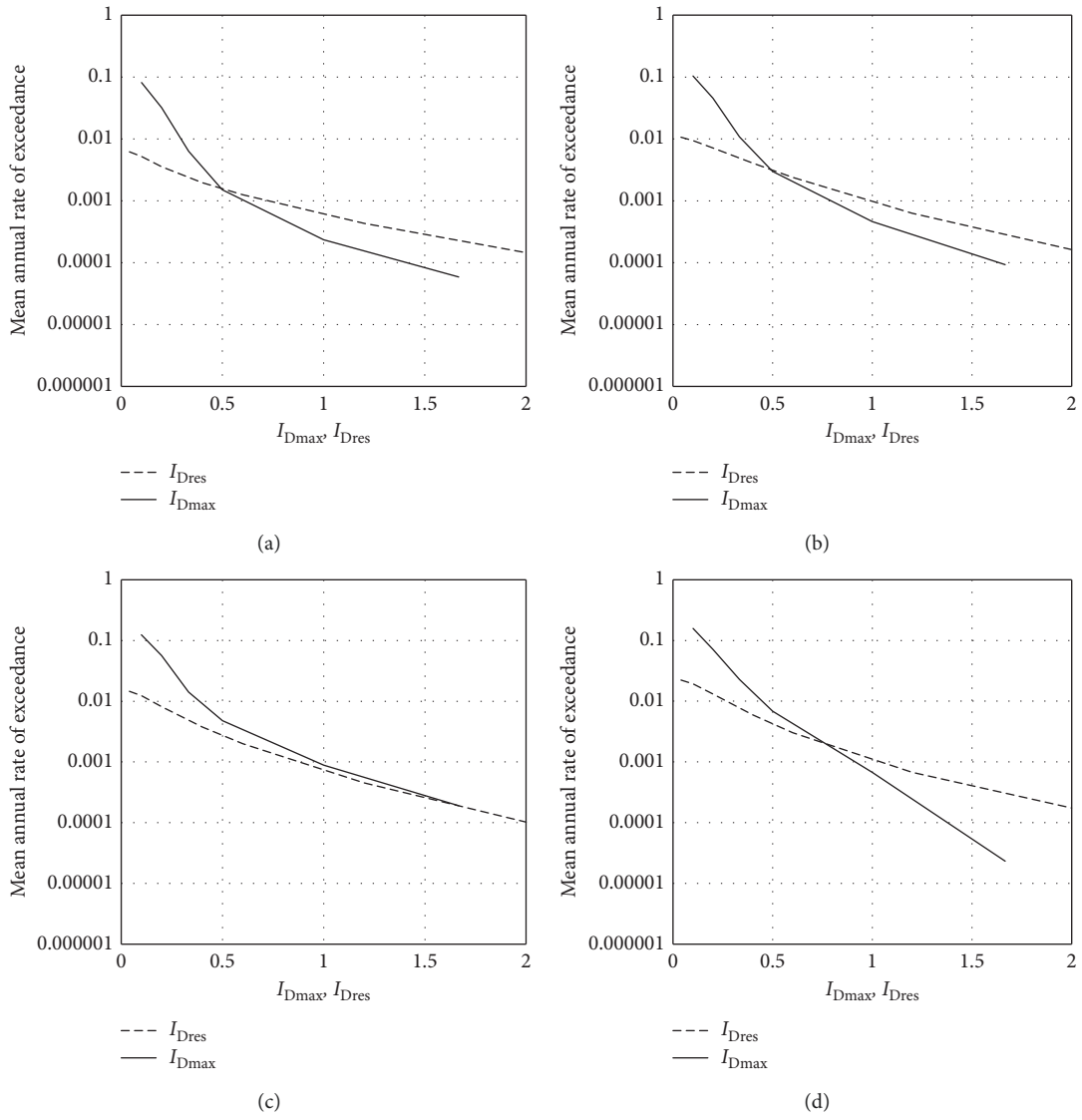

Figure 5: Comparison of the I_{Dmax} and I_{Dres} hazard curves for the MRSFs: (a) F4, (b) F6, (c) F8, and (d) F10.

Mexican Building Code to guarantee an adequate structural dynamic behavior of buildings prone to earthquakes. To further illustrate the importance of residual drift demands in comparison with peak interstory drift demands via seismic analysis. Two damage indicators are computed. The first damage parameter is calculated as the ratio of the maximum interstory drift demand divided by 3%, the threshold value of maximum drift to avoid collapse according to the MCBC, in such a way that values equal to or larger than one of this maximum drift damage index (I_{Dmax}) indicates the failure of the system in terms of peak drift. On the other hand, the second damage index I_{Dres} is similar to the first one but the residual peak drift demand divided by a value of 0.5% should be considered (the threshold residual drift limit that could be perceptible to human occupants and it could lead to human discomfort [4]). Values larger than one of I_{Dres} are related to the structural failure in terms of residual demands. Figure 5 compares the I_{Dmax} and I_{Dres} hazard curves for all the MRSFs at different performance levels. It is observed that in the case of the frames F4, F6, F8, and F10, when the damage index is equals to one, the mean annual rate of exceedance (MARE) is smaller in terms of peak interstory drift demands in comparison with the residual drift. In other words, the structural reliability of the selected MRSFs is larger for peak drifts indicating that the control of maximum demand does not necessarily guarantee the same level of safety in terms of residual drift demands. For this reason, if the parameter to estimate the structural performance of structures is the maximum interstory drift demand, it is necessary to obtain larger structural reliability levels aimed to provide adequate structural performance in terms of residual drift because it is necessary to obtain at least the same structural reliability in terms of I_{Dmax} and I_{Dres}. For this reason, with the aim to increase the seismic performance for residual drift demands, PTCs are incorporated in the selected MRSFs.

The seismic hazard curves in terms of maximum interstory drift damage index I_{Dmax} obtained for the MRSFs and the PTC steel frames are compared in Figure 6. In this

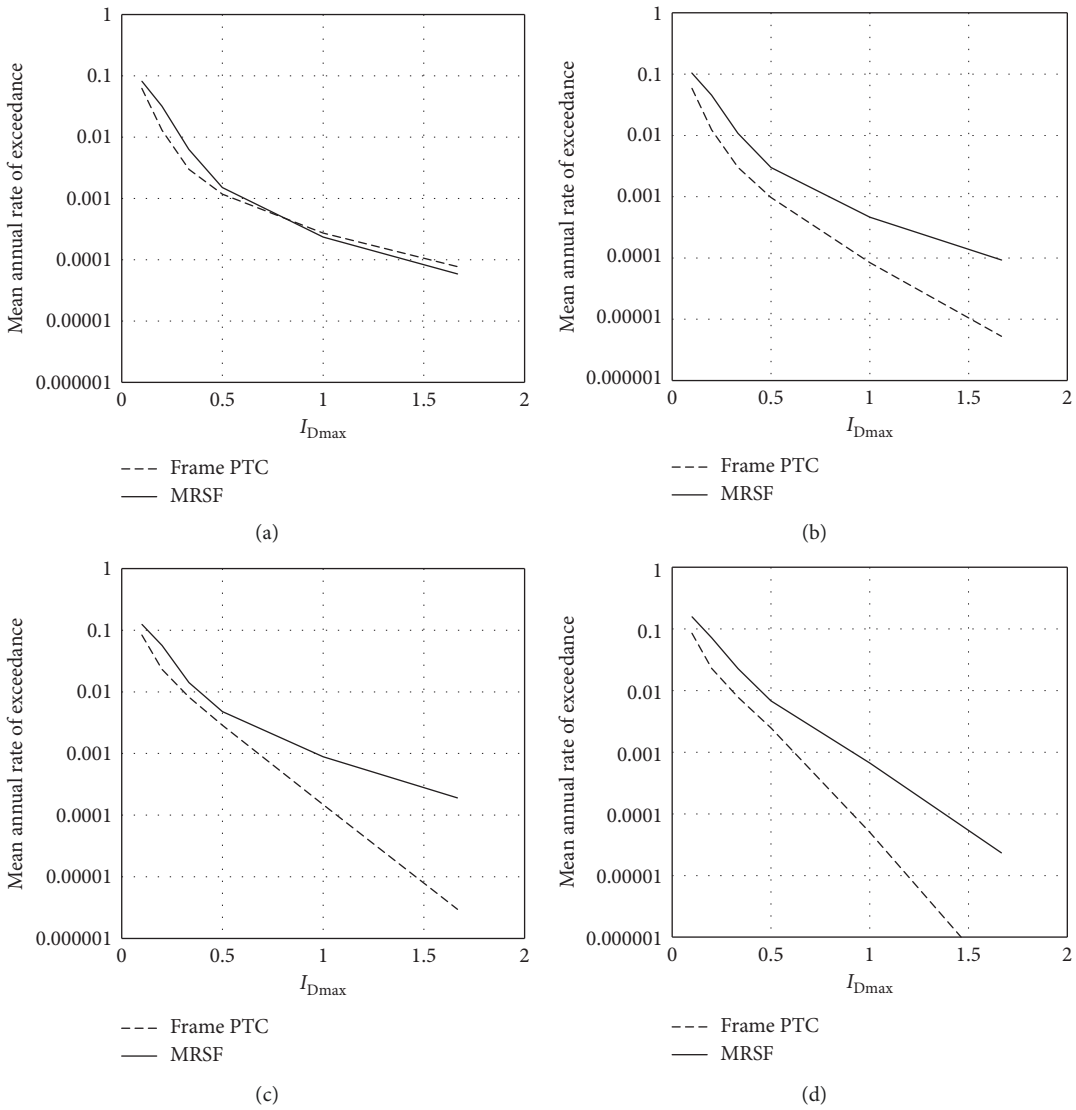

FIGURE 6: Comparison of the I_{Dmax} curves for the MRSFs and the PTC steel frames with (a) 4 stories, (b) 6 stories, (c) 8 stories, and (d) 10 stories.

figure, it can be observed that the structural reliability or the mean annual rate of exceeding a specific value of maximum interstory drift is in general smaller for the steel frame with PTC. Thus, the seismic performance in terms of peak demands is increasing when the PTCs are incorporated in the traditional MRSFs, which also could represent an increase in the structural reliability for the residual interstory drift demands as will be discussed below.

The comparison of the structural reliability for the MRSFs and the PTC frames in terms of residual drift demands provided by the I_{Dres} (damage index in terms of residual displacements) is illustrated in Figure 7. As it was expected, the mean annual rate of exceedance of I_{Dres} value is reduced when PTCs are incorporated into the traditional steel frames, which is valid for all the structures under consideration. In such a way, the use of PTC is a good alternative, for example, as a solution for rehabilitation of buildings or in order to reduce peak and residual drift demands of traditional structural steel systems under severe earthquakes.

Finally, a comparison of the mean annual rate of exceedance values when the damage index is equal to one in terms of I_{Dmax} for the MRSFs and in terms of I_{Dres} for the PTC steel frames is provided in Table 3. The aim of using the MARE values for I_{Dmax} is because they represent the target structural reliability levels obtained buildings designed according to the Mexican Building Code. Thus, the MARE values in terms of I_{Dres} for the PTC steel frames should be reduced in comparison to those of peak interstory drift for the MRSFs to guarantee that by including PTC in the traditional steel frames, it is possible to satisfy the structural reliability for the residual demands provided by the requirements of the Mexican Code. In Table 3, a column name ratio was used which represents the ratio of MARE of I_{Dres} (PTC steel frames) divided by I_{Dmax} (MRSFs), and values

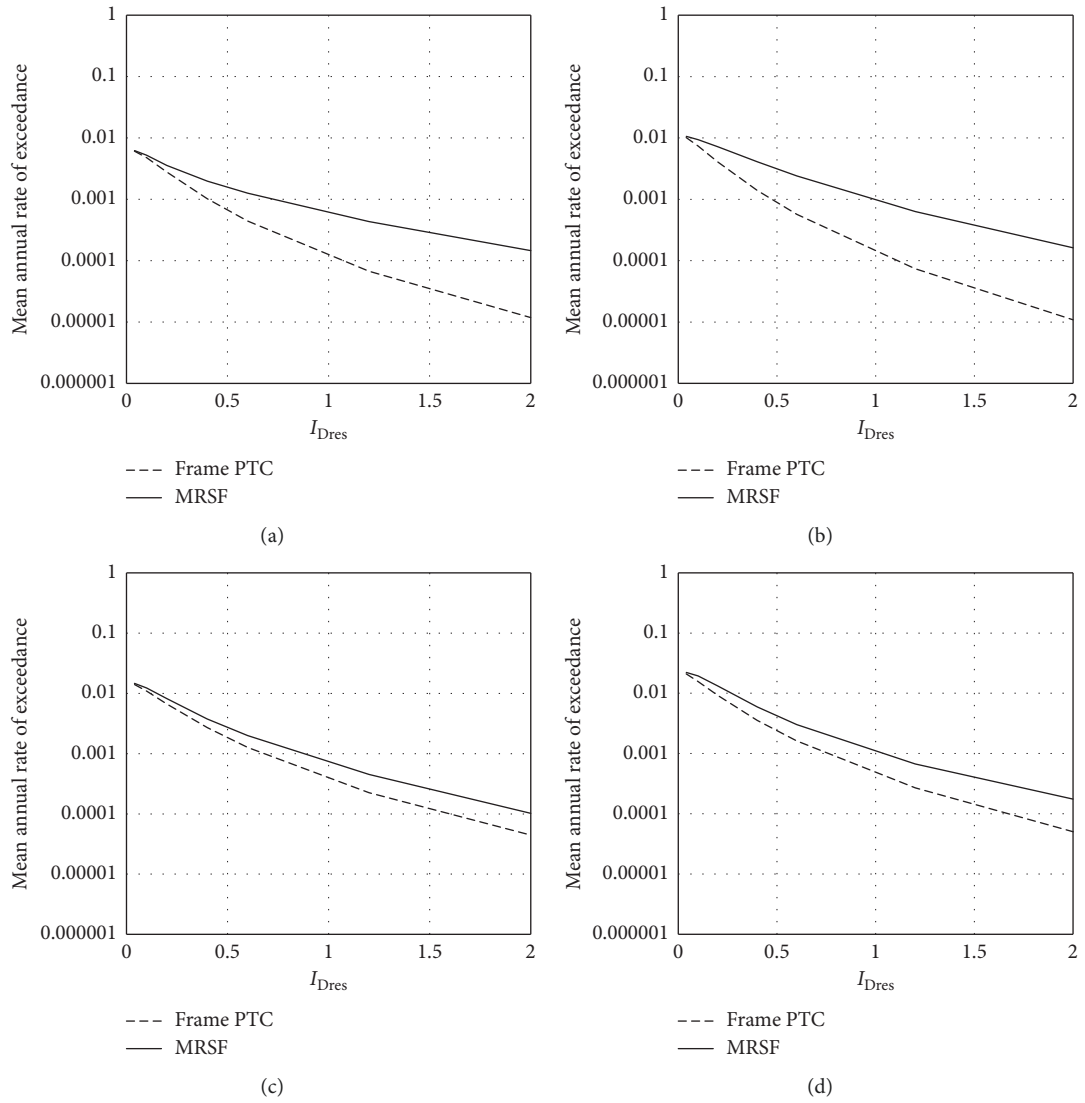

Figure 7: Comparison of the I_{Dres} hazard curves for the MRSFs and the PTC steel frames with (a) 4 stories, (b) 6 stories, (c) 8 stories, and (d) 10 stories.

Table 3: Mean annual rate of exceedance values when the damage index is equal to one in terms of I_{Dmax} for the MRSFs and in terms of I_{Dres} for the PTC steel frames.

Steel frame	MARE for $I_{Dmax} = 1$	Steel frame	MARE for $I_{Dres} = 1$	Ratio
F4	0.00024	F4	0.00019	0.79
F6	0.00046	F6	0.00024	0.52
F8	0.00089	F8	0.00057	0.64
F10	0.00067	F10	0.00072	1.07

smaller or equal to one indicates that the structural reliability is larger in terms of residual drift demands for the PTC frames comparing with the peak drifts of the MRSFs. It is observed that the values of the mean annual rates of exceedance for the PTC steel frames are in general smaller to those of the traditional structures when the damage index is equal to one.

3. Conclusions

The structural reliability of four moment-resisting steel frames is estimated in terms of peak and residual interstory drift seismic demands. For this aim, all the structures are subjected to 30 narrow-band ground motion records of the soft soil of Mexico City. The numerical results indicates that the structural reliability of the traditional steel frames is not adequate in terms of residual interstory drift demands. For this reason, PTCs are incorporated into the selected steel framed buildings in order to increase the structural reliability based on a damage index for the residual interstory drifts. As it was expected, for most of the steel framed buildings, the ability of self-centering for the steel frames incorporating PTC reduces significantly the residual demands; in fact, for this type of structural systems, the structural reliability is larger in terms of residual interstory drifts for most of the frames under consideration in comparison with peak demands of the

MRSFs. Moreover, the seismic performance in terms of peak demands is also increasing when PTCs are incorporated into the traditional MRSFs. It is concluded that the use of PTC is a good alternative as a solution for rehabilitation of buildings or in order to reduce peak and residual interstory drift seismic demands of traditional structural steel systems under severe earthquakes. Furthermore, PTC in steel frames could be an interesting solution toward structural systems with high seismic resilience.

Data Availability

The data used to support the findings of this study are available from the corresponding author upon request.

Conflicts of Interest

The authors declare that there are no conflicts of interest regarding the publication of this paper.

Acknowledgments

The financial support given by the Universidad Autónoma de Sinaloa under grant PROFAPI and the Universidad Michoacana de San Nicolás de Hidalgo is appreciated. The authors express their gratitude to the *Consejo Nacional de Ciencia y Tecnología* (CONACYT) in Mexico for funding the research reported in this paper under grant Ciencia Básica. Financial support also was given by DGAPA-UNAM under grant PAPIIT IN10351. In addition, Julián Carrillo thanks the Vicerrectoría de Investigaciones at Universidad Militar Nueva Granada for providing research grants.

References

[1] E. Rosenblueth and R. Meli, "The 1985 Mexico earthquake: causes and effects in Mexico City," *Concrete International (ACI)*, vol. 8, no. 5, pp. 23–34, 1986.

[2] T. Okada, T. Kabeyasawa, T. Nakano, M. Maeda, and T. Nakamura, "Improvement of seismic performance of reinforced concrete school buildings in Japan-Part 1 Damage survey and performance evaluation after the 1995 Hyogo-Ken Nambu earthquake," in *Proceedings of the 12th World Conference on Earthquake Engineering*, vol. 2421, Auckland, New Zealand, February 2000.

[3] Y. Iwata, H. Sugimoto, and H. Kuguamura, "Reparability limit of steel structural buildings based on the actual data of the Hyogoken-Nanbu earthquake," in *Proceedings of the 38th Joint Panel*, vol. 1057, pp. 23–32, Wind and Seismic effects, NIST Special Publication, Gaithersburg, MD, USA, May 2006.

[4] J. McCormick, H. Aburano, M. Ikenaga, and M. Nakashima, "Permissible residual deformation levels for building structures considering both safety and human elements," in *Proceedings of the 14th World Conference on Earthquake Engineering*, Beijing, China, October 2008.

[5] E. Bojórquez and J. Ruiz-García, "Residual drift demands in moment-resisting steel frames subjected to narrow-band earthquake ground motions," *Earthquake Engineering and Structural Dynamics*, vol. 42, no. 11, pp. 1583–1598, 2013.

[6] S. Pampanin, C. Christopoulos, and M. J. Nigel Priestley, "Performance-based seismic response of frame structures including residual deformations: part II: multi-degree of freedom systems," *Journal of Earthquake Engineering*, vol. 7, no. 1, pp. 119–147, 2003.

[7] D. Pettinga, C. Christopoulos, S. Pampanin, and N. Priestley, "Effectiveness of simple approaches in mitigating residual deformations in buildings," *Earthquake Engineering & Structural Dynamics*, vol. 36, no. 12, pp. 1763–1783, 2006.

[8] J. Erochko, C. Christopoulos, R. Tremblay, and H. Choi, "Residual drift response of SMRFs and BRB frames in steel buildings designed according to ASCE 7-05," *Journal of Structural Engineering*, vol. 137, no. 5, pp. 589–599, 2011.

[9] J. Ruiz-García and E. Miranda, "Performance-based assessment of existing structures accounting for residual displacements," John A. Blume Earthquake Engineering Center, Technical Report 153, Stanford University, Stanford, CA, USA, 2005, http://blume.stanford.edu/Blume/TechnicalReports.htm.

[10] J. Ruiz-García and E. Miranda, "Evaluation of residual drift demands in regular multi-storey frames for performance-based seismic assessment," *Earthquake Engineering & Structural Dynamics*, vol. 35, no. 13, pp. 1609–1629, 2006.

[11] J. Ruiz-García and E. Miranda, "Probabilistic estimation of residual drift demands for seismic assessment of multi-story framed buildings," *Engineering Structures*, vol. 32, no. 1, pp. 11–20, 2010.

[12] S. R. Uma, S. Pampanin, and C. Christopoulos, "Development of probabilistic framework for performance-based seismic assessment of structures considering residual deformations," *Journal of Earthquake Engineering*, vol. 14, no. 7, pp. 1092–1111, 2010.

[13] U. Yazgan and A. Dazio, "Post-earthquake damage assessment using residual displacements," *Earthquake Engineering & Structural Dynamics*, vol. 41, no. 8, pp. 1257–1276, 2012.

[14] J. M. Ricles, R. Sause, M. M. Garlock, and C. Zhao, "Post-tensioned seismic-resistant connections for steel frames," *Journal of Structural Engineering*, vol. 127, no. 2, pp. 113–121, 2001.

[15] J. M. Ricles, R. Sause, S. W. Peng, and L. W. Lu, "Experimental evaluation of earthquake resistant posttensioned steel connections," *Journal of Structural Engineering*, vol. 128, no. 7, pp. 850–859, 2002.

[16] J. M. Ricles, R. Sause, Y. C. Lin, and C. Y. Seo, "Self-centering moment connections for damage-free seismic response of steel MRFs," in *Proceedings of the Structures Congress*, vol. 2010, Orlando, FL, USA, May 2010.

[17] C. Christopoulos, A. Filiatrault, and C. M. Uang, "Self-centering post-tensioned energy dissipating (PTED) steel frames for seismic regions," Report no. SSRP-2002/06, University of California, Oakland, CA, USA, 2002.

[18] C. Christopoulos and A. Filiatrault, "Seismic response of posttensioned energy dissipating moment resisting steel frames," in *Proceedings of the 12th European Conference on Earthquake Engineering*, London, UK, September 2002.

[19] C. Christopoulos, A. Filiatrault, and C. M. Uang, "Seismic demands on post-tensioned energy dissipating moment-resisting steel frames," in *Proceedings of the Steel Structures in Seismic Areas (STESSA)*, Naples, Italy, June 2003.

[20] M. M. Garlock, J. M. Ricles, and R. Sause, "Experimental studies of full-scale posttensioned steel connections," *Journal of Structural Engineering*, vol. 131, no. 3, pp. 438–448, 2005.

[21] M. M. Garlock, R. Sause, and J. M. Ricles, "Behavior and design of posttensioned steel frame systems," *Journal of Structural Engineering*, vol. 133, no. 3, pp. 389–399, 2007.

[22] M. M. Garlock, J. M. Ricles, and R. Sause, "Influence of design parameters on seismic response of post-tensioned steel MRF

systems," *Engineering Structures*, vol. 30, no. 4, pp. 1037–1047, 2008.

[23] H.-J. Kim and C. Christopoulos, "Seismic design procedure and seismic response of post-tensioned self-centering steel frames," *Earthquake Engineering & Structural Dynamics*, vol. 38, no. 3, pp. 355–376, 2009.

[24] C. C. Chung, K. C. Tsai, and W. C Yang, "Self-centering steel connection with steel bars and a discontinuous composite slab," *Earthquake Engineering & Structural Dynamics*, vol. 38, no. 4, pp. 403–422, 2009.

[25] M. Wolski, J. M. Ricles, and R. Sause, "Experimental study of self-centering beam-column connection with bottom flange friction device," *ASCE Journal of Structural Engineering*, vol. 135, no. 5, 2009.

[26] G. Tong, S. Lianglong, and Z. Guodong, "Numerical simulation of the seismic behavior of self-centering steel beam-column connections with bottom flange friction devices," *Earthquake Engineering and Engineering Vibration*, vol. 10, no. 2, pp. 229–238, 2011.

[27] Z. Zhou, X. T. He, J. Wu, C. L. Wang, and S. P. Meng, "Development of a novel self-centering buckling-restrained brace with BFRP composite tendons," *Steel and Composite Structures*, vol. 16, no. 5, pp. 491–506, 2014.

[28] Mexico City Building Code, *Normas Técnicas Complementarias para el Diseño por Sismo*, Departamento del-Distrito Federal, Mexico City, Mexico, 2004, in Spanish.

[29] J. Shen and A. Astaneh-Asl, "Hysteretic behavior of bolted-angle connections," *Journal of Constructional Steel Research*, vol. 51, no. 3, pp. 201–218, 1999.

[30] R. M. Richard, *PRCONN, Moment-Rotation Curves for Partially Restrained Connections*, RMR Design Group, Tucson, Arizona, 1993.

[31] A. Carr, *RUAUMOKO, Inelastic Dynamic Analysis Program*, University of Cantenbury, Department of Civil Engineering, Christchurch, New Zealand, 2011.

[32] A. López-Barraza, E. Bojórquez, S. E. Ruiz, and A. Reyes-Salazar, "Reduction of maximum and residual drifts on posttensioned steel frames with semirigid connections," *Advances in Materials Science and Engineering*, vol. 2013, Article ID 192484, 11 pages, 2013.

[33] E. Bojórquez and S. E. Ruiz, "Strength reduction factors for the valley of Mexico taking into account low cycle fatigue effects," in *Proceedings of the 13° World Conference on Earthquake Engineering*, Vancouver, Canada, August 2004.

[34] A. Teran-Gilmore and J. O. Jirsa, "Energy demands for seismic design against low-cycle fatigue," *Earthquake Engineering & Structural Dynamics*, vol. 36, no. 3, pp. 383–404, 2007.

[35] M. D. Trifunac and A. G. Brady, "A study of the duration of strong earthquake ground motion," *Bulletin of the Seismological Society of America*, vol. 65, no. 3, pp. 581–626, 1975.

[36] D. Vamvatsikos and C. A. Cornell, "Incremental dynamic analysis," *Earthquake Engineering and Structural Dynamics*, vol. 26, no. 3, pp. 701–716, 2002.

[37] G. G. Deierlein, "Overview of a comprehensive framework for performance earthquake assessment," Report PEER 2004/05, Pacific Earthquake Engineering Center, Berkeley, California, 2004.

[38] E. Bojórquez, A. Terán-Gilmore, S. E. Ruiz, and A. Reyes-Salazar, "Evaluation of structural reliability of steel frames: interstory drift versus plastic hysteretic energy," *Earthquake Spectra*, vol. 27, no. 3, pp. 661–682, 2011.

[39] E. Bojórquez and I. Iervolino, "Spectral shape proxies and nonlinear structural response," *Soil Dynamics and Earthquake Engineering*, vol. 31, no. 7, pp. 996–1008, 2011.

[40] J. L. Alamilla, *Reliability-based seismic design criteria for framed structures*, Ph.D. thesis, Universidad Nacional Autónoma de México, UNAM. Mexico City, Mexico, 2001, in Spanish.

Hindawi
Advances in Civil Engineering
Volume 2019, Article ID 7654683, 11 pages
https://doi.org/10.1155/2019/7654683

Research Article

A Framework to Assess the Seismic Resilience of Urban Hospitals

Peng Yu,[1,2] Weiping Wen,[1,2] Duofa Ji,[1,2] Changhai Zhai,[1,2] and Lili Xie[1,3]

[1]*Key Lab of Structures Dynamic Behavior and Control of the Ministry of Education, Harbin Institute of Technology, Harbin 150090, China*
[2]*Key Lab of Smart Prevention and Mitigation of Civil Engineering Disasters of the Ministry of Industry and Information Technology, Harbin Institute of Technology, Harbin 150090, China*
[3]*Institute of Engineering Mechanics, China Earthquake Administration, Harbin 150080, China*

Correspondence should be addressed to Weiping Wen; wenweiping@hit.edu.cn

Received 22 March 2019; Revised 13 May 2019; Accepted 26 May 2019; Published 11 June 2019

Academic Editor: Jorge Ruiz-García

The phenomenon of hospital functional interruption has been widely observed in the historical moderate-strong earthquakes, indicating that hospital functionality cannot be well considered in the current seismic design methods. The concept of seismic resilience pays enough attention to postearthquake functionality of buildings, and it is particularly significant for the urban hospitals which play critical role in the urban postearthquake rescue and recovery. This study proposes a framework to assess the seismic resilience of urban hospitals, by incorporating the fault tree analysis (FTA) to consider the interdependency between the damage of nonstructural components and the functionality of medical equipment, as well as the effect of external supplies on the functionality of hospital. The proposed framework is then applied to a case-study hospital, and the results indicate that this hospital needs 1.1 days to resume emergency functionality under REDi repair strategy after design basis earthquake (DBE), while it needs 28.8 days to resume emergency functionality under REDi repair strategy after maximum considered earthquake (MCE). It is found that the seismic resilience of this hospital after MCE cannot meet the community requirements on the recovery time, and necessary measures are needed to improve the seismic resilience. The proposed framework provides the quantitative results of seismic resilience assessment in the preearthquake environment and can further support emergency response planning and seismic retrofits strategies.

1. Introduction

Urban hospitals are generally expected to offer timely medical services for the earthquake injuries once the moderate-strong earthquakes strike the city. However, the phenomenon of hospital functional interruption has been widely observed in the historical moderate-strong earthquakes [1, 2], indicating that hospital functionality cannot be well considered in the current seismic design methods. The past engineering experience confirmed that the current design codes [3–5] can generally satisfy the requirement on the structural safety. However, nonstructural components damage and functional loss of medical equipment cannot be prevented, and past earthquakes [6–8] have shown that the failure of nonstructural components and medical equipment are the main reason for hospital functional interruption.

Seismic resilience, the ability of a system to maintain preearthquake functionality or recover to a new level, is treated as a promising alternative to deal with the problem of hospital functionality which has been ignored in current seismic codes. Several studies have been performed to study the seismic resilience of hospitals. Yavari et al. [9] defined the hospital performance levels (fully functional, functional, affected functional, and not functional) by utilizing damage data from past earthquakes. The indicators, such as the quality of service and life [10], patient waiting time [11], and functional downtime [12], have been separately adopted to assess the seismic resilience of hospitals. Cimellaro et al. [13] proposed a fast methodology for disaster resilience quantification where factor analysis was used to identify representative factors from varieties of dimensions. Iuliis et al. [14] proposed an interesting method to evaluate the downtime of building structures from three parts (actual

damage, irrational delays, and utilities disruption) by introducing the fuzzy logic, which are expected to increase the accuracy of resilience evaluation. Monti and Nuti [15] used logical schemes to describe the complex hospital organization and presented a reliability-based procedure to assess the failure probability of hospital services after a seismic event, paying no attention on the recovery process. Bruneau et al. [16] proposed a hospital resilience quantification framework by incorporating the physical performance and hospital functionality. Pan American Health Organization (PAHO) [17] gave a hospital safety guide in the form of checklists and scoring system which aims to quickly determine the interventions that can improve its seismic safety. Fault tree analysis (FTA) is a kind of method for analysing complex systems reliability and safety [18], and it has been applied to the building system failure analysis [19, 20]. Jacques et al. [21] analysed the functionality of critical clinical and support services by FTA where fault trees were established based on three main factors (staff, structure, and stuff), but the damage data (e.g., utility loss and its duration) from seismic surveys are needed in their method.

In the postearthquake environment, the functionality of medical equipment is greatly affected by the damage extent of nonstructural components. The interdependency between the damage of nonstructural components and the functionality of medical equipment, which has been generally ignored in the previous studies, is significant for the seismic resilience assessment of hospitals. Besides, the external supplies also have an obvious effect on the functionality of hospital, and the situation of external supplies needs to be included in the seismic resilience assessment of hospitals.

In light of the above discussions, a framework for the assessment of the seismic resilience of hospitals is firstly proposed. The fault tree analysis (FTA) is used in this framework to consider the interdependency between the damage of nonstructural components and the functionality of medical equipment, as well as the effect of external supplies on the functionality of hospitals. The different repair strategies, i.e., series, parallel, and Resilience-based Earthquake Design Initiative (REDi) methods [22], are also included in this framework. Finally, the proposed framework is applied to a case-study hospital, and the quantitative assessment results on the seismic resilience are obtained. Innovative building damage assessment methods [23] and retrofit strategies [24] provide lots of alternatives which can be used to improve seismic resilience of hospitals. The proposed framework can further support the assessment and choice of emergency response planning and seismic retrofits strategies.

2. Resilience Assessment Framework

Based on earthquake observations, PAHO [17] recognized the importance of hospital safety and put forward the following safety objectives: life safety, investment protection, and functional protection. These objectives aim to ensure that hospitals not only remain standing but hold functionality. By considering the safety objectives proposed by PAHO, the following indicators are used in the framework: damage state, casualties, economic loss, and availabilities of medical services. In order to reflect the critical role of emergency functionality in the treatment of earthquake-induced casualties, hospital services are divided into *full* and *emergency*. *Full* means that all components in hospitals are undamaged and hospitals can provide routine and emergency services. *Emergency* indicates that parts of services are interrupted, but emergency service remains operational. The other two functionality levels are *life safety* and *none*. *Life safety* means that the hospital has lost its capacity of providing medical service, but the main structure would not experience the damage that threat people's life. *None* indicates that the main structure of the hospital has experienced severe damage or even collapse. Table 1 summarizes the four levels of functionality for hospitals and the corresponding definition. The functionality levels are ranked in the order of implementation difficulty: full, emergency, life safety, and none.

This framework has five main blocks: the earthquake selection, the physical response, the loss analysis, functionality evaluation, and resilience assessment. The response of structure, in terms of maximum interstory displacement ratio (MIDR) and peak floor acceleration (PFA) are obtained by dynamic time history analysis, enable the fragility analysis of structural, nonstructural components, and medical equipment in hospitals. FEMA P58 [25–27] provide a rich component fragility function database for structural and nonstructural components; however, the functionality of medical equipment and external supplies need to be added. The economic loss and the number of casualties are estimated according to the damage states of all components in hospitals. The estimation of functionality level is operated before repair work (if needed) by the estimation rules mentioned above and repeated until the repair work finishes (i.e., updating the functionality level when the repair work progresses). FTA is adopted in this framework to consider the effect of interdependencies on emergency functionality failure. Meanwhile, the selection of repair strategy, such as parallel repair strategy, serial repair strategy, and REDi methods, has an important effect on the recovery phase. Thus, these three repair strategies are also included, and the quantitative effects can be observed in the following case study. Finally, the functionality curve $Q(t)$ is used in the in this framework. Assessment of the resilience of hospitals in future earthquakes inherently entails significant uncertainties. The resilience of hospitals depends on a number of factors which include the intensity of ground shaking, the response of structures, the vulnerability of components to damage, etc. In the framework, Monte Carlo simulation method is used to consider the uncertainties related to those factors.

Figure 1 shows the details and flow chart for the proposed framework. The details on the functionality evaluation (i.e., step of estimating functionality level in Figure 1) are specially explained here. After the physical responses (e.g., damage state of components and medical equipment), the results of loss analysis (e.g., casualties) are obtained. If components and medical equipment are not damaged, the

Table 1: Four levels of functionality and the corresponding definition.

Functionality	Definition
Full	No damage
Emergency	Emergency service keeps operational
Life safety	Emergency functionality stops but no casualties occur
None	No entry or collapse

functionality of hospital would be in the *Full* level. Once some components or medical equipment are damaged, then FTA is used to analyse whether the hospital can provide the emergency medical service. If not, the rest two levels will be determined by the casualties.

The framework ends with the computed resilience level, and the resilience index [28] adopted herein is expressed as

$$R = \int_{t_{OE}}^{t_{OE}+T_{LC}} \frac{Q(t)}{T_{LC}dt}, \quad (1)$$

T_{LC} is the control time interested and T_{OE} is the time when the event happens.

3. Case Study

3.1. Hospital Description. The hospital used in this study is a five-story reinforced concrete frame building which is 68m long, 45 m wide, and 18.9 m high (Figure 2). Figure 3 illustrates the plan of the first and fifth floor and shows the location of critical departments in emergency service. The reinforced concrete frames are designed based on Chinese seismic design code [5]. The seismic fortification intensity of this building is seven, and soil class is II.

For nonlinear dynamic analysis of the hospital, fourteen ground motion records were selected from the PEER ground motion database with the following criteria: (a) the moment magnitude M_w of the seismic events is above 6.0; (b) the average shear wave velocity of the upper 30 m soil Vs30 varies from 260 m/s to 510 m/s; and (c) the mean acceleration response spectra of selected ground motions match the seismic design spectra of DBE level in Chinese seismic design code [5]. The comparison between the response spectra of selection records and the design spectra is shown in Figure 4, and the good agreement can be observed between them.

Nonlinear time history analysis is performed on three-dimensional frames (Figure 5) by SAP2000 [29]. Beams and columns are modelled using frame elements, and the slabs are modelled as rigid diaphragms. Uniaxial moment plastic hinges are assigned at both ends of the beams, and P-M-M interaction hinges are assigned at the bottom of columns. P-delta effect is considered in the analysis. MIDR and PFA are used in this study to quantify the damage of structural components, nonstructural components, and medical equipment. Figure 6 shows the mean MIDR of this building under SLE (service level earthquake), DBE, and MCE. Figure 7 presents the mean PFA of this building under the above intensity levels. The results in Figure 6 indicate that this building meets the MIDR requirements (i.e., MIDR<1/50) of reinforcement concrete frames in Chinese seismic design code for the collapse prevention.

The logic scheme of the hospital functionality is shown in Figure 8 to illustrate the detailed architecture of hospital medical service. Resuscitation room, radiology department, supply room, oxygen room, and distribution room are located on the first floor. The red arrows in Figure 8 indicate the patient's transfer route from the rescue room to ward. Two elevators and five stairs ensure access to ORs. Two external power grids (black arrows) provide power for the hospital, and no backup generator is equipped here. The emergency service depends on four subsystems: building and medical system, supply system, gas system, and electric system. Hospitals usually set up multiple departments or rooms with the same function to work together in order to expand their treatment capacity (e.g., two operating rooms are set up on the fifth floor in the case study hospital). The interdependencies and redundancies of hospital systems should be considered comprehensively in the estimation of hospital functionality.

FTA is a kind of method to analyse the reliability and safety of complex systems based on the logical combination of a series events. The failure of emergency function is firstly selected as top event of fault tree. Then, intermediate events and basic events are determined by the causal link from top to bottom. The intermediate events are chosen as critical departments in emergency functionality. The fault tree of emergency service is created in collaboration with hospital managers (Figure 9). Rooms or medical equipment with the same functions are connected with AND logic gates to critical departments or rooms in which the redundancy can be taken into account. The basic events, shown as circles, are selected as the damages to critical medical equipment, nonstructural components damage, and loss of external power supply which can be simulated or estimated in preearthquake resilience assessment. The detailed information of all basic events is summarized in Table 2. The interdependencies between damage of nonstructural components and medical equipment are considered here. For example, some sophisticated medical equipment (CT and DR) and medical rooms have special requirements on temperature, humidity, dust, etc. The damage of architecture nonstructural components (e.g., partition wall and pipeline) and interruption of power supply will lead to the interruption of equipment and emergency functionality.

3.2. Functionality Analysis. The fragility functions for nonstructural components are taken from FEMA P-58 [27], and those of medical equipments are assumed to be the same as those of electrical equipments due to the lack of data. The fragilities and consequence functions of basic events in fault tree are listed in Table 2. The failure probability and repair time of external electric grids under different seismic hazards are also assumed in Table 3 for the same reason.

Nonstructural components generally have several damage states, and the corresponding consequence

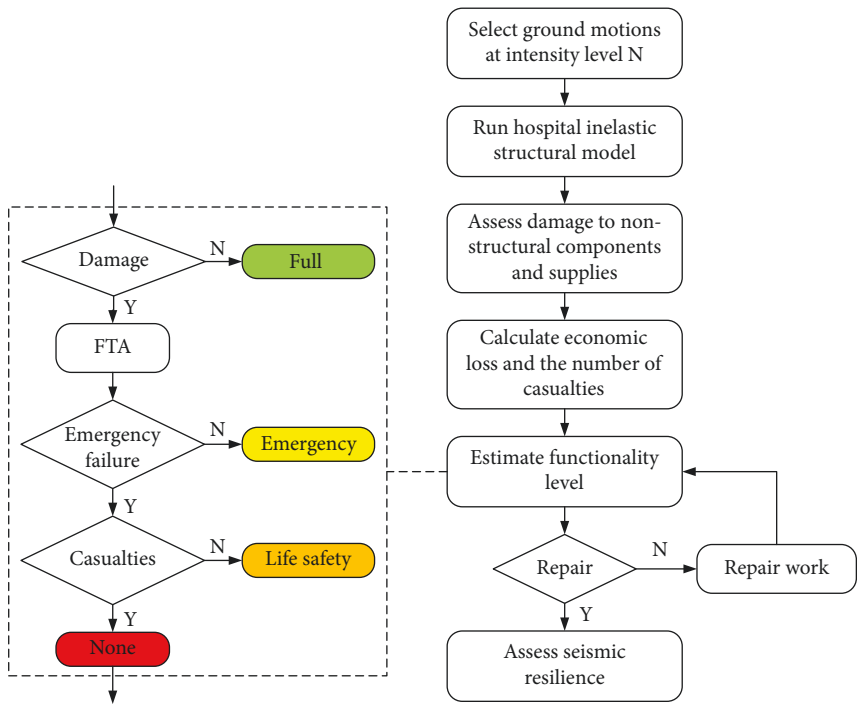

Figure 1: Seismic resilience assessment framework of a hospital.

(a) (b)

Figure 2: The location and exterior of the case study hospital.

functions are different. When using FTA to evaluate the emergency functionality, it is necessary to understand the operation conditions of medical equipment and select the allowable damage states of nonstructural components. For example, CT has strict requirements on air temperature and cleanliness during operation, and the dust generated by partition cracks may cause the CT to run out. So the allowable damage state of partition should be the crack state (i.e., lowest damage state of the partition). For the components that have several damage states, the consequence functions (e.g., repair time) need to be referred to FEMA P-58, and they are not listed in Table 2 for the succinctness.

Performance Assessment Calculation Tool (PACT) [27] is used to calculate the repair cost and repair time under parallel and serial repair strategies. The repair cost is a concerned indicator for hospital managers. Figure 10 shows the median repair cost for the three intensities. At levels of DBE and MCE, the total cost of repair is several magnitudes higher than that at SLE. Probability that the emergency functionality of hospital can keep operational after earthquakes is shown in Figure 11. The emergency functionality is very likely to be continuous under SLE, but the probability reduces to 38.4% under DBE. After MCE, the emergency functionality will be interrupted entirely. The loss caused by nonstructural components

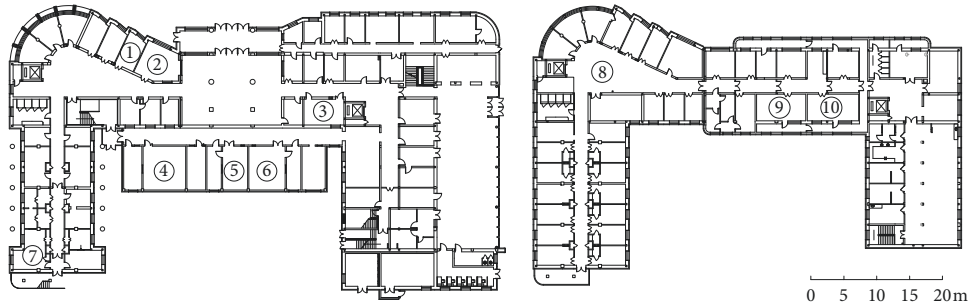

(a) (b)

Figure 3: Hospital building plans. (a) First floor. (b) 5th floor. The rooms numbered from 1 to 9 are resuscitation room, pharmacy, distribution room, magnetic resonance imaging (MRI) room, digital radiography (DR) room, computed tomography (CT) room, supply room, ward, operation room 1, and operation room 2, respectively.

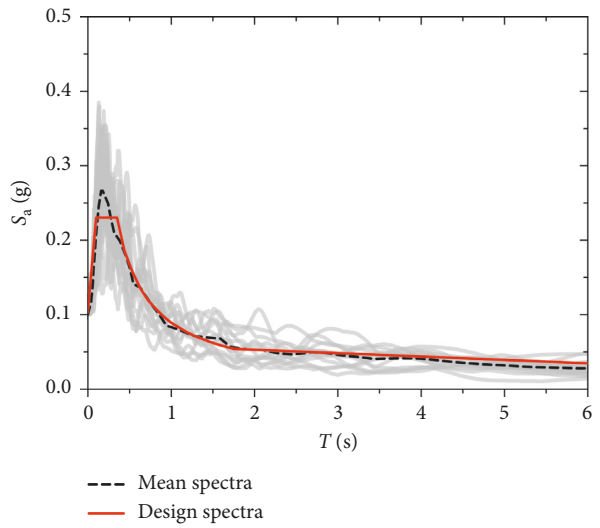

Figure 4: Comparison of mean acceleration response and seismic design spectrums.

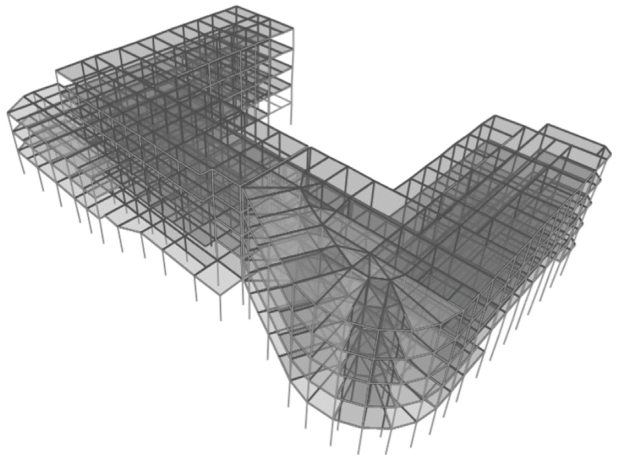

Figure 5: Finite element model of case study hospital.

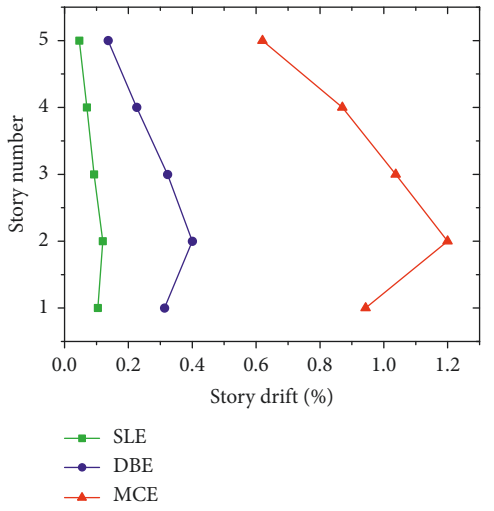

Figure 6: Mean MIDR of hospital building under SLE, DBE, and MCE.

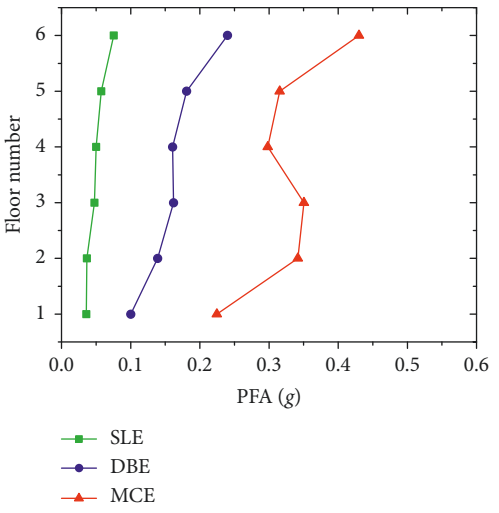

Figure 7: Mean PFA of hospital building under SLE, DBE, and MCE.

accounts for a large portion of the overall economic loss, confirming again on the importance of nonstructural components.

3.3. Resilience Analysis. According to the resilience assessment framework in this study, the hospital functionality level needs to be updated with repair processes. The

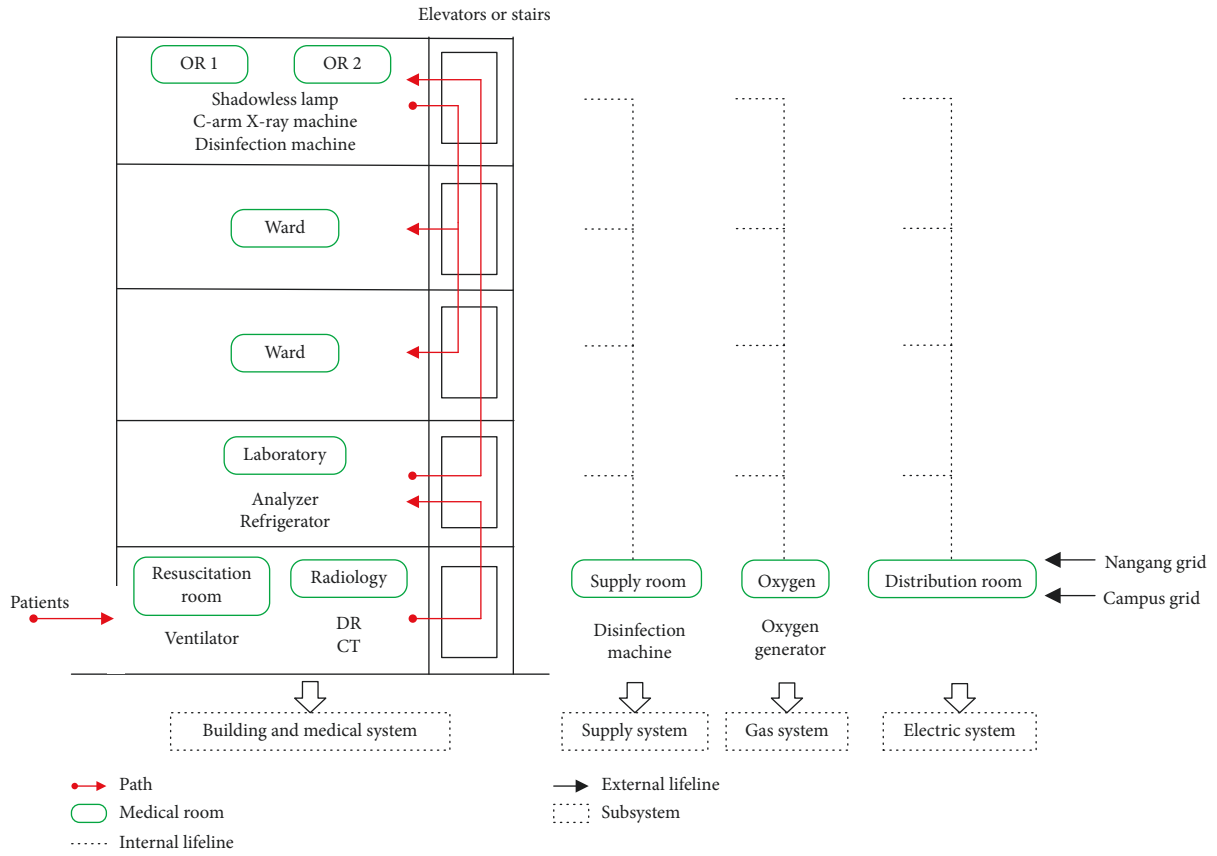

Figure 8: Hospital subsystems and logic scheme of the emergency service.

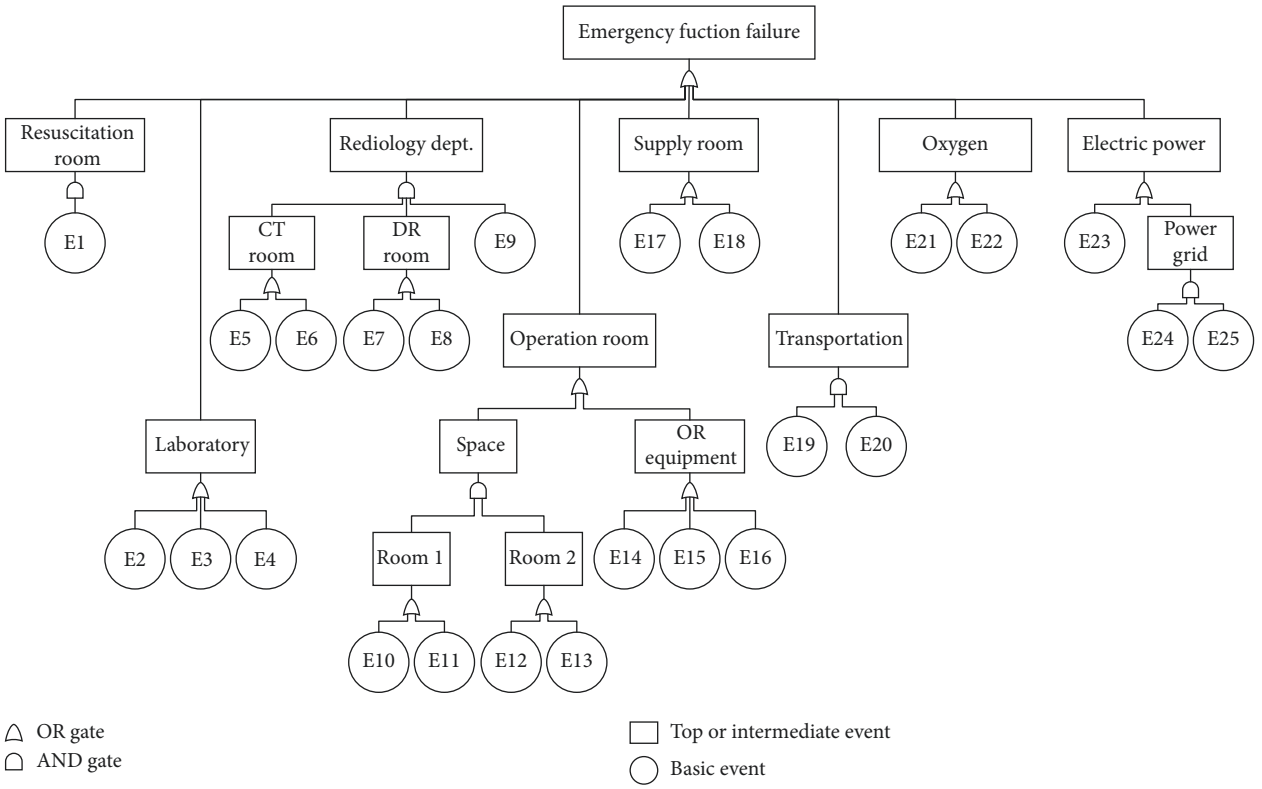

Figure 9: The fault tree of hospital emergency function.

Table 2: Fragilities of basic events in the fault tree and repair time.

No.	Event	EDP	(Median, dispersion)	Repair time (days)
1	Ventilator 1	PFA	(1, 0.5)	(1, 0.5)
2	Refrigerator	PFA	(1, 0.5)	(1, 0.5)
3	Blood analyser	PFA	(0.5, 0.5)	(1, 0.5)
4	Urine analyser	PFA	(0.5, 0.5)	(1, 0.5)
5	CT	PFA	(1, 0.5)	(0.2, 0.5)
6	CT wall	IDR	(0.005, 0.4)	
7	DR	PFA	(1, 0.5)	(0.2, 0.5)
8	DR wall	IDR	(0.004, 0.4)	
9	Portable DR	PFA	(1, 0.5)	(1, 0.5)
10	Shadow-less lamp 1	PFA	(1, 0.5)	(1, 0.5)
11	Partition in OR1	IDR	(0.005, 0.4)	
12	Shadow-less lamp 1	PFA	(1, 0.5)	(1, 0.5)
13	Partition in OR2	IDR	(0.005, 0.4)	
14	Anesthesia machine	PFA	(1, 0.5)	(1, 0.5)
15	Ventilator 2	PFA	(1, 0.5)	(1, 0.5)
16	C-arm X-ray machine	PFA	(1, 0.5)	(1, 0.5)
17	Disinfection machine	PFA	(1, 0.5)	(1, 0.5)
18	Partition 3	IDR	(0.005, 0.4)	
19	Elevator 1	PFA	(0.39, 0.45)	
20	Elevator 2	PFA	(0.39, 0.45)	
21	Oxygen generator	PFA	(1, 0.5)	(1, 0.5)
22	Oxygen pipe	PFA	(1.5, 0.4)	
23	Distribution room	PFA	(0.73, 0.45)	(0.6, 0.4)

Table 3: External electric grid (E24 and E25) failure probability and repair time (days).

	Pf (E24)	Repair time (median, dispersion)	Pf (E25)	Repair time (median, dispersion)
SLE	0.1	(0.5, 0.5)	0.1	(2, 0.5)
DBE	0.2	(1, 0.5)	0.3	(4, 0.5)
MCE	0.3	(2, 0.5)	0.4	(0.3, 4)

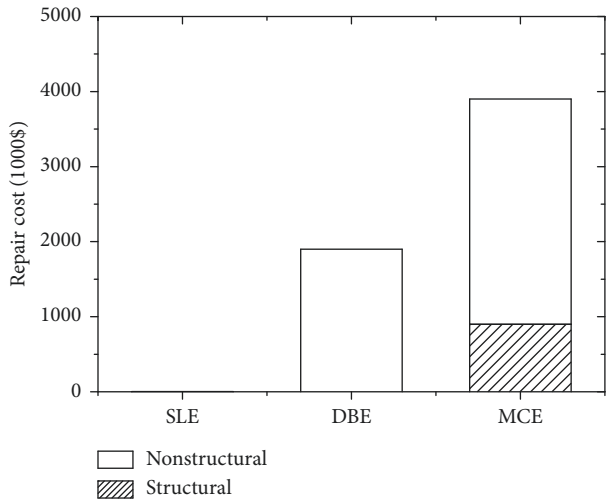

Figure 10: Median repair cost.

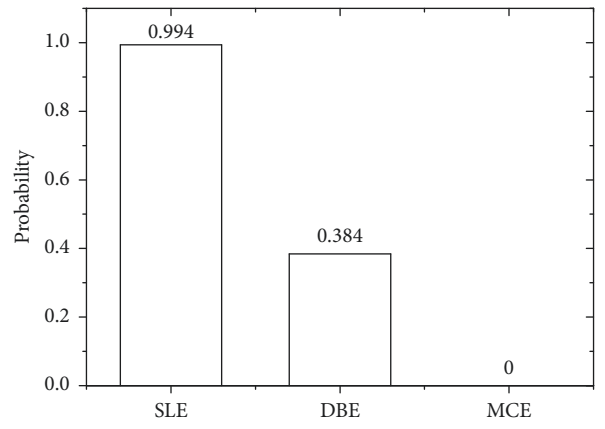

Figure 11: Probability that the emergency functionality of hospital can remain operational after earthquakes.

recovery curve illustrated in Figure 12 can be plotted along with time. The median functionality is used as the post-earthquake hospital functionality, and the T_1 and T_2 in curves are equal to median recovery time to higher functionalities, respectively. For comparing the resilience index of a case-study hospital under MCE, DBE, and SLE, T_{LC} is equal to the longest recovery time under three intensities. Three main repair strategies (parallel, serial, and REDi methods) are considered in the case study. Parallel strategy assumes that repair work is carried out simultaneously at all floors, while serial strategy assumes that repair work is carried out from ground to top floor. Both repair strategies assume that all damaged components are repaired sequentially within one floor. Compare

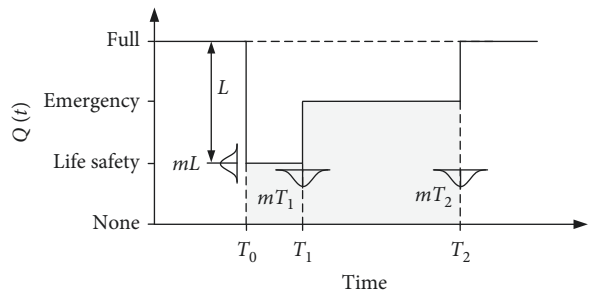

Figure 12: Hospital systems functionality curve and earthquake resilience.

to parallel and serial strategies, REDi method makes improvements on the allocation of labor and repair scheme which fits the reality.

The quantification of the four functionality levels (Table 1) is needed, in order to compute the resilience index expressed by equation (1). The values of functionality function Q for four functionality levels (high to low) is 1.0, 0.5, 0.3, and 0.0, by comprehensively considering the suggestions from experts and hospital managers, as well as our engineering experience. Figure 13 shows the recovery curves of hospital for the cases of three different earthquake levels and three different repair strategies.

It can be observed that the SLE has no effect on the emergency functionality, and the hospital also can recover to preearthquake level very quickly. The emergency functionality would be interrupted by the strike of DBE and MCE, but the main building of hospital would be life safety. The case study hospital needs 1.1 days to resume emergency functionality under REDi repair strategy after DBE, while it needs 28.8 days to resume emergency functionality under REDi repair strategy after MCE. It would take 8.2 days and 50 days to recover to the preearthquake level when the hospital is subjected to DBE and MCE, respectively.

The impact of the repair strategy is obvious for the cases of DBE and MCE. Figure 14 presents the recovery curves for different repair strategies when the hospital is subjected to MCE. The recovery curves in parallel and serial strategies provide the lower and upper bound for that in REDi strategy.

When calculating resilience index R by equation (1), T_{LC} is taken as 50 days which equals the final recovery time corresponding to MCE. The results of final recovery time and resilience index under SLE, DBE, and MCE are summarized in Table 4. The resilience index of case study hospital under MCE equals 0.39 which is much lower than that under SLE (0.99) and DBE (0.92).

After earthquakes, the number of injuries and the demand for medical services will change significantly over time. For example, the injuries in the Northbridge earthquake were more frequent than usual, but injury admissions tended to return to normal levels after several days [30]. As seriously injured patients have a narrow window of survival, the hospital functionality (especially the emergency functionality) should be coordinated with the demand of injuries and meet the minimum survival time. According to the analysis of the case study hospital, the recovery time (e.g., 28.8 days for case of MCE) of the emergency functionality is too long to cure numerous injuries. The results indicate that the case study hospital needs to be retrofitted or strengthened to improve its seismic resilience.

4. Conclusions

A framework is proposed in this study to assess the seismic resilience of hospital. The fault tree analysis (FTA) is used in this framework to consider the interdependency between the damage of nonstructural components and the functionality of medical equipment, as well as the effect of external supplies on the functionality of hospital. The different repair strategies (i.e., series, parallel, and REDi) are also considered in this framework. Finally, the proposed framework is applied to a case-study hospital, and the main conclusions are as following:

(1) The adoption of FTA in the framework facilitates the consideration of interdependency between the damage of nonstructural components and the functionality of medical equipment, as well as the effect of external supplies on the functionality of hospital, making the framework provide more realistic assessment results on seismic resilience.

(2) The case-study hospital needs 1.1 days to resume emergency functionality under REDi repair strategy after DBE (design basis earthquake), while it needs 28.8 days to resume emergency functionality under REDi repair strategy after MCE (maximum considered earthquake). The seismic resilience of case study hospital after MCE cannot meet the community requirements on the recovery time, and decision-makers need to take necessary measures to improve the seismic resilience.

(3) The repair strategy has clear effects on the recovery time and resilience assessment results, and it should be noted that the quantitative assessment results provided by this framework depend the selection of repair strategy (i.e., series, parallel, and REDi).

The lack of fragility and consequence data of medical equipment and external supplies may influence the

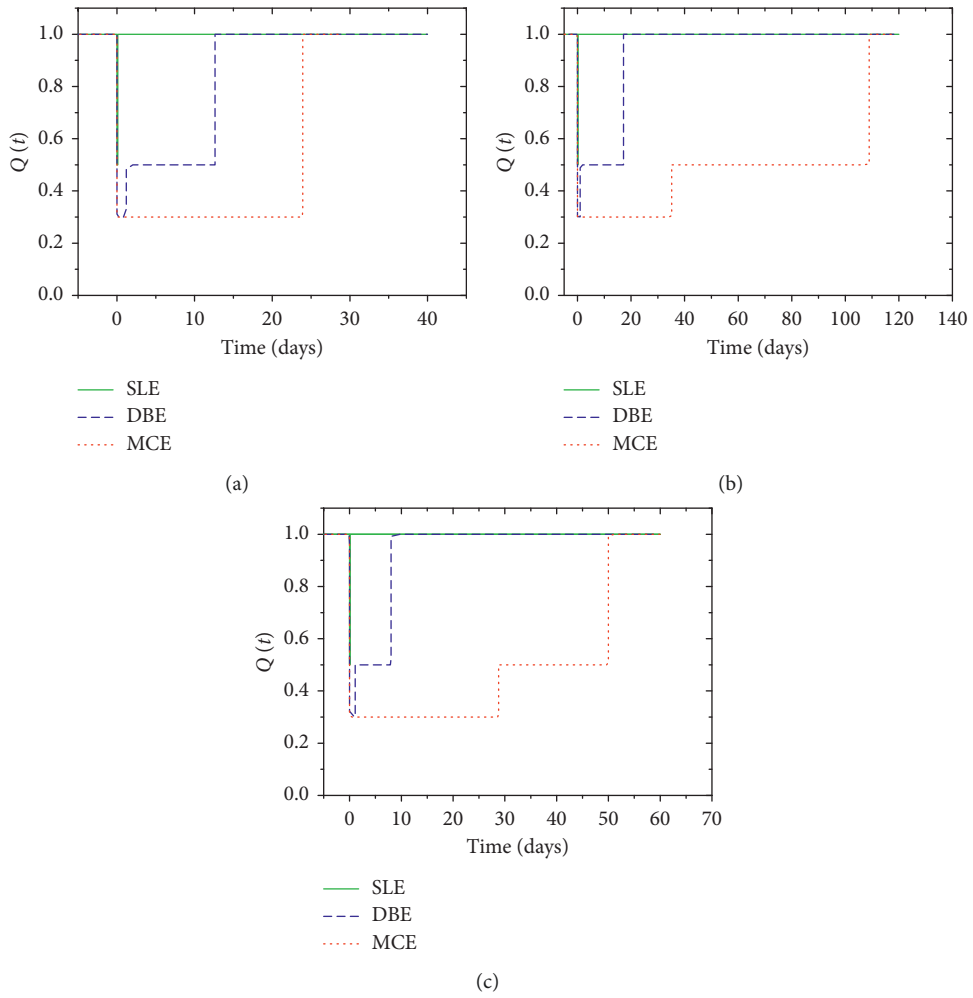

Figure 13: Recovery curves under (a) recovery curves under the parallel strategy, (b) recovery curves under the serial strategy, and (c) recovery curves under REDi strategy.

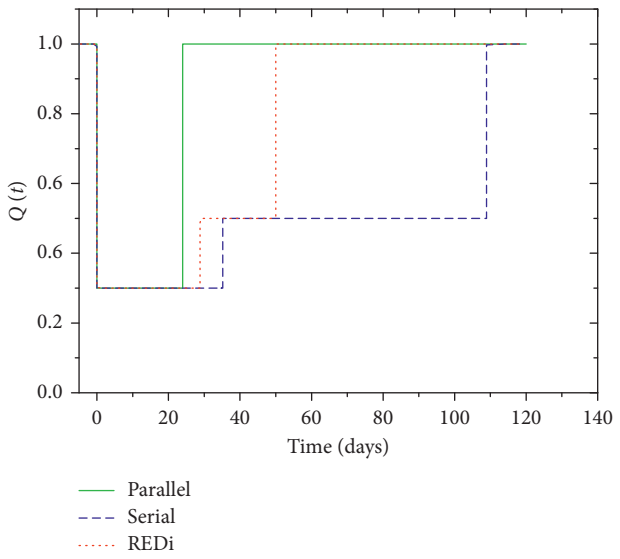

Figure 14: Recovery curves under MCE by different repair strategies.

Table 4: Resilience index and recovery time of case study hospital under three intensity levels.

Earthquake intensity	Recovery time (days)	R
SLE	0.1	0.99
DBE	8.2	0.92
MCE	50	0.39

quantitative results but would not affect the flexibility and usage of the proposed framework. However, attention should be paid to the usability of the fault tree proposed in the case study because of differences among hospitals, and a revised fault tree may be needed. The direct extensions of results beyond the case study are not suggested due to the specific seismic hazards and structure type here. Extensive applications of this framework will be completed by the cooperation of experts from different multidisciplinary such as engineers, architects, specialists in hospital equipment, and health-care professionals. The framework provides evaluation criteria for the update

strategy and can be further applied to other types of critical facilities.

Data Availability

The ground motions used in this study are deposited in the Pacific Earthquake Engineering Research Centre (PEER) Next Generation Attenuation (NGA) relationships database (http://ngawest2.berkeley.edu/). The software PACT is used to support this study, and it is available at https://www.atcouncil.org/p-58.

Conflicts of Interest

The authors declare that there are no conflicts of interest regarding the publication of this paper.

Acknowledgments

The authors want to express their sincere gratitude to Jing Chen, Vice President of Hospital of Harbin Institute of Technology, for her kind help. This investigation is supported by the National Natural Science Foundation of China (nos. 51825801 and 51708161), National Key R&D Program of China (no. 2017YFC1500604), and China Postdoctoral Science Foundation (no. 2018T110305). These supports are greatly appreciated.

References

[1] T. D. Kirsch, J. Mitrani-Reiser, R. Bissell et al., "Impact on hospital functions following the 2010 Chilean earthquake," *Disaster Medicine and Public Health Preparedness*, vol. 4, no. 2, pp. 122–128, 2010.

[2] J. Mitrani-Reiser, M. Mahoney, W. T. Holmes et al., "A functional loss assessment of a hospital system in the bio-bio province," *Earthquake Spectra*, vol. 28, no. 1, pp. 473–502, 2012.

[3] European Committee for Standardization, *Eurocode 8: Design of Structures for Earthquake Resistance-Part 1: General Rules, Seismic Actions and Rules for Buildings*, 2004.

[4] American Society of Civil Engineers/Structural Engineering Institute, *Minimum Design Loads for Buildings and Other Structures ASCE 7-10*, Reston, VA, USA, 2009.

[5] Ministry of Housing and Urban-Rural Development of China, *Code for Seismic Design of Buildings GB 50011-2010*, Beijing, China, 2016, in Chinese.

[6] N. Achour, M. Miyajima, M. Kitaura, and A. Price, "Earthquake-induced structural and nonstructural damage in hospitals," *Earthquake Spectra*, vol. 27, no. 3, pp. 617–634, 2011.

[7] G. Santarsiero, L. Di Sarno, S. Giovinazzi et al., "Performance of the healthcare facilities during the 2016-2017 Central Italy seismic sequence," *Bulletin of Earthquake Engineering*, pp. 1–27, 2018.

[8] R. C. Myrtle, S. F. Masri, R. L. Nigbor, and J. P. Caffrey, "Classification and prioritization of essential systems in hospitals under extreme events," *Earthquake Spectra*, vol. 21, no. 3, pp. 779–802, 2005.

[9] S. Yavari, S. E. Chang, and K. J. Elwood, "Modeling post-earthquake functionality of regional health care facilities," *Earthquake Spectra*, vol. 26, no. 3, pp. 869–892, 2010.

[10] G. P. Cimellaro, A. M. Reinhorn, and M. Bruneau, "Seismic resilience of a hospital system," *Structure and Infrastructure Engineering*, vol. 6, no. 1-2, pp. 127–144, 2010.

[11] G. P. Cimellaro, M. Malavisi, and S. Mahin, "Using discrete event simulation models to evaluate resilience of an emergency department," *Journal of Earthquake Engineering*, vol. 21, no. 2, pp. 203–226, 2017.

[12] P. Favier, A. Poulos, J. A. Vásquez et al., "Seismic risk assessment of an emergency department of a Chilean hospital using a patient-oriented performance model," *Earthquake Spectra*, 2018, In press.

[13] G. P. Cimellaro, M. Malavisi, and S. Mahin, "Factor analysis to evaluate hospital resilience," *ASCE-ASME Journal of Risk and Uncertainty in Engineering Systems, Part A: Civil Engineering*, vol. 4, no. 1, article 04018002, 2018.

[14] M. D. Iuliis, O. Kammouh, G. P. Cimellaro, and S. Tesfamariam, "Downtime estimation of building structures using fuzzy logic," *International Journal of Disaster Risk Reduction*, vol. 34, pp. 196–208, 2019.

[15] G. Monti and C. Nuti, "A procedure for assessing the functional reliability of hospital systems," *Structural Safety*, vol. 18, no. 4, pp. 277–292, 1996.

[16] M. Bruneau and A. Reinhorn, "Exploring the concept of seismic resilience for acute care facilities," *Earthquake Spectra*, vol. 23, no. 1, pp. 41–62, 2007.

[17] Pan American Health Organization (PAHO), *Hospital Safety Index: Guide for Evaluators*, Washington, DC, USA, 2008.

[18] W. S. Lee, D. L. Grosh, F. A. Tillman, and C. H. Lie, "Fault Tree analysis, methods, and applications-a review," *IEEE Transactions on Reliability*, vol. R-34, no. 3, pp. 194–203, 1985.

[19] S. Youance, M.-J. Nollet, and G. McClure, "Effect of critical sub-system failures on the post-earthquake functionality of buildings: a case study for Montréal hospitals," *Canadian Journal of Civil Engineering*, vol. 43, no. 10, pp. 929–942, 2016.

[20] K. Porter and K. Ramer, "Estimating earthquake-induced failure probability and downtime of critical facilities," *Journal of Business Continuity & Emergency Planning*, vol. 5, no. 4, pp. 352–364, 2012.

[21] C. C. Jacques, J. McIntosh, S. Giovinazzi, T. D. Kirsch, T. Wilson, and J. Mitrani-Reiser, "Resilience of the canterbury hospital system to the 2011 christchurch earthquake," *Earthquake Spectra*, vol. 30, no. 1, pp. 533–554, 2014.

[22] I. Almufti and M. Willford, *REDi™ Rating System: Resilience-Based Earthquake Design Initiative for the Next Generation of Buildings*, Arup, San Francisco, CA, USA, 2013.

[23] G. P. Cimellaro, G. Scura, C. S. Renschler, A. M. Reinhorn, and H. U. Kim, "Rapid building damage assessment system using mobile phone technology," *Earthquake Engineering and Engineering Vibration*, vol. 13, no. 3, pp. 519–533, 2014.

[24] G. P. Cimellaro and D. Lopez-Garcia, "Algorithm for design of controlled motion of adjacent structures," *Structural Control and Health Monitoring*, vol. 18, no. 2, pp. 140–148, 2011.

[25] Federal Emergency Management Agency (FEMA), *Seismic Performance Assessment of Buildings Volume 1-Methodology*, Technical Report FEMA-P58, Washington, DC, USA, 2012.

[26] Federal Emergency Management Agency (FEMA), *Seismic Performance Assessment of Buildings Volume 2-Implementation Guide*, Technical Report FEMA-P58, Washington, DC, USA, 2012.

[27] Federal Emergency Management Agency (FEMA), *Seismic Performance Assessment of Buildings Volume 3-Supporting Electronic Materials and Background*, Technical Report FEMA-P58, Washington, DC, USA, 2012.

[28] G. P. Cimellaro, A. M. Reinhorn, and M. Bruneau, "Framework for analytical quantification of disaster resilience," *Engineering Structures*, vol. 32, no. 11, pp. 3639–3649, 2010.

[29] CSI (Computers and Structures Inc.), *SAP2000 v20 Integrated Finite Element Analysis and Design of Structures*, CSI, Berkeley, CA, USA, 2018.

[30] D. L. McArthur, C. Peek-Asa, and J. F. Kraus, "Injury hospitalizations before and after the 1994 Northridge, California earthquake," *American Journal of Emergency Medicine*, vol. 18, no. 4, pp. 361–366, 2000.

Hindawi
Advances in Civil Engineering
Volume 2019, Article ID 9747896, 8 pages
https://doi.org/10.1155/2019/9747896

Research Article

The Effect of Concrete Footing Shape in Differential Settlement: A Seismic Design

Abdoullah Namdar, Yun Dong, and Yin Deyu

Faculty of Architecture and Civil Engineering, Huaiyin Institute of Technology, Huai'an, China

Correspondence should be addressed to Yun Dong; hadyun@163.com

Received 30 December 2018; Accepted 21 February 2019; Published 10 April 2019

Guest Editor: Edén Bojórquez

This paper presents the numerical results of concrete footing-soil foundation seismic interaction mechanism. The concrete footing has been made with two different shapes, but with the equal volume of concrete material. The concrete footing-soil foundation has been analyzed using nonlinear finite elements, with the fixed-base state. The simulated near-fault ground motions have been applied to the concrete footing-soil foundation. The problem has been formulated based on the settlement controlled analysis. The local geotechnical conditions of all configurations have been analyzed. The numerical analysis results indicate that the shape of a concrete footing alters seismic response, revises inertial interaction, enhances damping ratio, improves load carry capacity, modifies cyclic differential settlement, revises failure patterns, minimizes nonlinear deformation, and changes cyclic strain energy dissipation. The novelty of this research work is the strain energy has more been dissipated with artistic concrete footing design.

1. Introduction

A number of the buildings have been collapsed due to improper soil-footing interaction; it has occurred when dynamic or seismic forces have been applied to them. The improvement of soil-footing seismic interaction mechanism is an art in geotechnical earthquake engineering design and needs to select appropriate footing shape to enhance the safety of the structure.

There are many experimental, numerical, and theoretical research studies which mainly focus on differential settlement and bearing capacity of the soil when the soil has been subjected to simulated seismic loading, liquefaction, and landslide. The outcome of these research studies has been realizing failure mitigation of soil foundation and introducing different methods for improving soil foundation stability [1–12]. Using research idea from different branches of science and applying them in geotechnical earthquake engineering is an acceptable research methodology. In this regard, there is an investigation on quantitative shape evaluation of graphite particles in ductile iron [13]; with attention to this research work, the effect of concrete footing shape in minimizing differential settlement of soil foundation needs to be investigated. However, the geotechnical earthquake engineering is a young field, and the concept of the seismic stress response of concrete footing-soil foundation model is a complicated mechanism and needs more investigation. In the present study, the seismic design of concrete footing with considering the configuration of concrete footing to minimize differential settlement at the base of concrete footing has been investigated. Earthquake includes differential settlement, but the shape of concrete footing in producing differential settlement has not been studied with considering seismic response at the base of a concrete footing, energy dissipation, hysteretic soil damping, strain travel paths, inertial interaction, nonlinear deformation patterns, and footing-soil seismic interaction mechanism. We hope all we have done could support the seismic design of concrete footing in considering the safety of concrete footing and soil foundation to support solving geotechnical earthquake engineering problems.

2. Problem Definition

In the previous studies, many investigations have been made in understanding the differential settlement of soil, when the

soil has been subjected to dynamic loading [2, 3, 6, 12]. The present investigations analyzed the soil foundation-concrete footing seismic interaction mechanism and stability, with considering concrete shape. There is no investigation on the effect of concrete footing geometry to soil foundation-concrete footing seismic interaction present in the literature, and the associated simulation indirectly even cannot be found in the literature. The idea to do this research work is to understand the effect of concrete footing shape on (i) soil foundation-concrete footing seismic interaction mechanism, (ii) the differential settlement, (iii) the nonlinear deformation, (iv) the strain paths, and (v) the failure patterns. Two types of concrete foundations have been considered and have been analyzed numerically. The concrete footing and soil foundation, simultaneously, have been subjected to seismic loading. In all configurations, single concrete footing has been analyzed. In the present study, the specific geometry of concrete footing may increase or reduce soil-footing interaction. From the theoretical concept point of view, to provide an appropriate solution for this problem, and for solving and demonstrating this elasticity problem, the ABAQUS software has been employed. The ABAQUS has been employed to solve and explain many engineering problems in the various fields through numerical simulation [12, 14–18]. The ABAQUS has the ability to solve nonlinear problems in high quality. To design the concrete footing with maximum safety and minimum cost, two different configurations of concrete footing have numerically been investigated. In both configurations, the same volume and grade of concrete have been used. The method of embedded concrete footing in the soil foundation is adopted, and also the interaction method for soil foundation with concrete footing in ABAQUS environment has been adopted. The footing and soil have been loaded. The problem has been formulated based on the settlement controlled analysis. The seismic response of concrete footing and soil foundation in all models has been compared.

3. Domain Theoretical Concept for Present Analysis

The nonlinear deformation develops due to six components of stresses applied to a body element; the six components of stresses are $\sigma_x, \sigma_y, \sigma_z, \tau_{xy}, \tau_{xz}$, and τ_{yz}.

Two types of distortions arise: (i) direct strain $\varepsilon_x, \varepsilon_y$, and ε_{yz} from σ_x, σ_y, and σ_z and (ii) angular distortions e_{xy}, e_{xz}, and e_{yz} from τ_{xy}, τ_{xz}, and τ_{yz}. The strains and rotation components for each tensor may be expressed in terms of their respective displacements gradients:

$$e_{ij} = \begin{bmatrix} \dfrac{\partial u}{\partial x} & \dfrac{\partial u}{\partial y} & \dfrac{\partial u}{\partial z} \\ \dfrac{\partial v}{\partial x} & \dfrac{\partial v}{\partial y} & \dfrac{\partial v}{\partial z} \\ \dfrac{\partial w}{\partial x} & \dfrac{\partial w}{\partial y} & \dfrac{\partial w}{\partial z} \end{bmatrix}. \quad (1)$$

The strain matrix is

$$\varepsilon_{ij} = \begin{bmatrix} \dfrac{\partial u}{\partial x} & \dfrac{1}{2}\left(\dfrac{\partial u}{\partial y} + \dfrac{\partial v}{\partial x}\right) & \dfrac{1}{2}\left(\dfrac{\partial u}{\partial z} + \dfrac{\partial w}{\partial x}\right) \\ \dfrac{1}{2}\left(\dfrac{\partial u}{\partial y} + \dfrac{\partial v}{\partial x}\right) & \dfrac{\partial v}{\partial y} & \dfrac{1}{2}\left(\dfrac{\partial v}{\partial z} + \dfrac{\partial w}{\partial y}\right) \\ \dfrac{1}{2}\left(\dfrac{\partial u}{\partial z} + \dfrac{\partial w}{\partial x}\right) & \dfrac{1}{2}\left(\dfrac{\partial v}{\partial z} + \dfrac{\partial w}{\partial y}\right) & \dfrac{\partial w}{\partial z} \end{bmatrix}. \quad (2)$$

The rotation matrix is

$$\omega_{ij} = \begin{bmatrix} 0 & \dfrac{1}{2}\left(\dfrac{\partial u}{\partial y} - \dfrac{\partial v}{\partial x}\right) & \dfrac{1}{2}\left(\dfrac{\partial u}{\partial z} - \dfrac{\partial w}{\partial x}\right) \\ -\dfrac{1}{2}\left(\dfrac{\partial u}{\partial y} - \dfrac{\partial v}{\partial x}\right) & 0 & \dfrac{1}{2}\left(\dfrac{\partial v}{\partial z} - \dfrac{\partial w}{\partial y}\right) \\ -\dfrac{1}{2}\left(\dfrac{\partial u}{\partial z} - \dfrac{\partial w}{\partial x}\right) & -\dfrac{1}{2}\left(\dfrac{\partial v}{\partial z} - \dfrac{\partial w}{\partial y}\right) & 0 \end{bmatrix},$$

$$\begin{bmatrix} e_x & e_{xy} & e_{xz} \\ e_{yx} & e_y & e_{yz} \\ e_{zx} & e_{zy} & e_z \end{bmatrix} = \begin{bmatrix} \varepsilon_x & \varepsilon_{xy} & \varepsilon_{xz} \\ \varepsilon_{yx} & \varepsilon_y & \varepsilon_{yz} \\ \varepsilon_{zx} & \varepsilon_{zy} & \varepsilon_z \end{bmatrix} + \begin{bmatrix} \omega_x & \omega_{xy} & \omega_{xz} \\ \omega_{yx} & \omega_y & \omega_{yz} \\ \omega_{zx} & \omega_{zy} & \omega_z \end{bmatrix}. \quad (3)$$

Consequently, the complete distortion of a volume element may be expressed as the sum of corresponding strains and rotations in the matrix form [19]. In this study, the nonlinear finite element analysis has been applied to analyze seismic behavior of concrete footing-soil foundation interaction. Accordingly, the soil foundation and concrete footing have numerically been investigated. The six strain components will not act independently; they have a direct relationship with the displacements. Under earthquake function, due to loading, unloading, and reloading process, an element can translate, rotate, compress, or elongate.

4. Materials and Modeling

The concrete footing-soil foundation has been modeled using nonlinear finite elements, with the fixed-base state. The soil foundation is $1.8 * 1.8 * 0.9$ (m). The concrete footing for configuration-1 and configuration-2 are $0.6 * 0.6 * 0.4$ (m) and $0.4 * 0.9 * 0.4$ (m), respectively. For both models, the concrete foundation of $0.2 * 0.2 * 0.2$ (m) is installed on center of concrete footing. The soil foundation-concrete footing seismic interaction has been evaluated. The concrete footing configuration is with two different shapes and equal volume. In the numerical analysis, the typical mesh has been used. The concrete footing is placed on a horizontal surface of the soil foundation; it is shown in Figures 1 and 2. The simulated near-fault ground motions, with equal magnitude, have numerically been applied to concrete footing and soil foundation. The acceleration history of the earthquake occurred in Norcia, Italy, has been used in numerical analysis and is shown in Figures 3 and 4. From 22 to 28 seconds of the earthquake, the main seismic excitation has been observed. In comparing E, N, and Z comps, the E comp has maximum acceleration history and

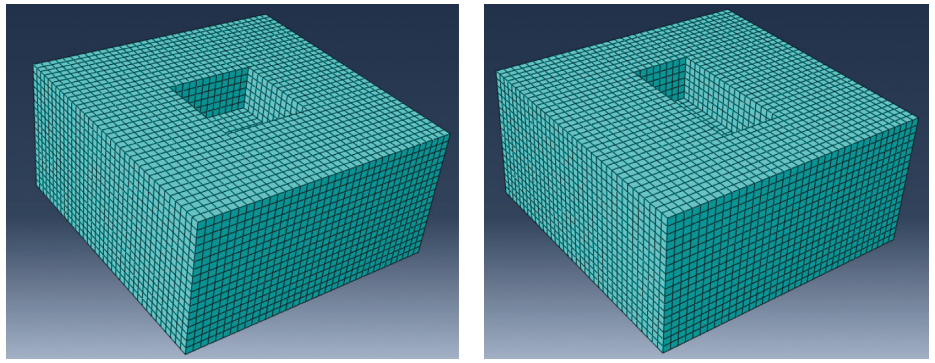

(a) (b)

Figure 1: Soil models. (a) Configuration-1. (b) Configuration-2.

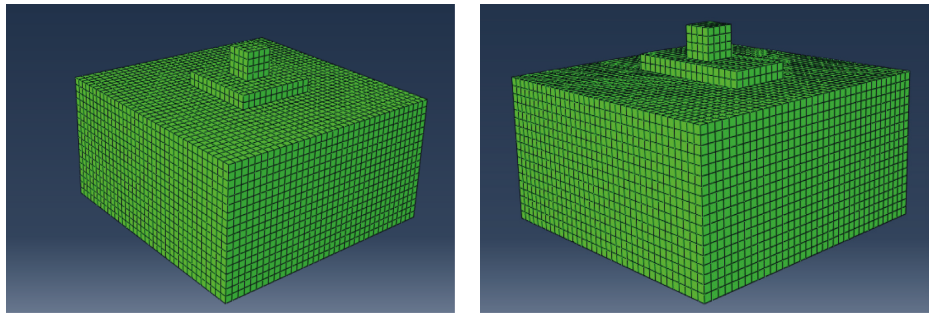

(a) (b)

Figure 2: Concrete footing-soil configurations. (a) Configuration-1. (b) Configuration-2.

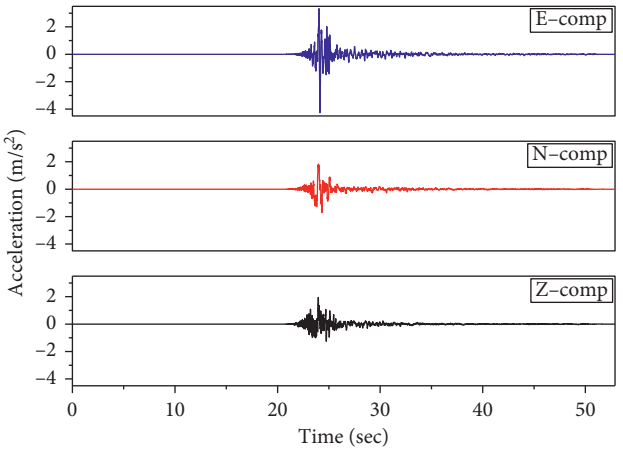

Figure 3: Acceleration history of Norcia Earthquake [20].

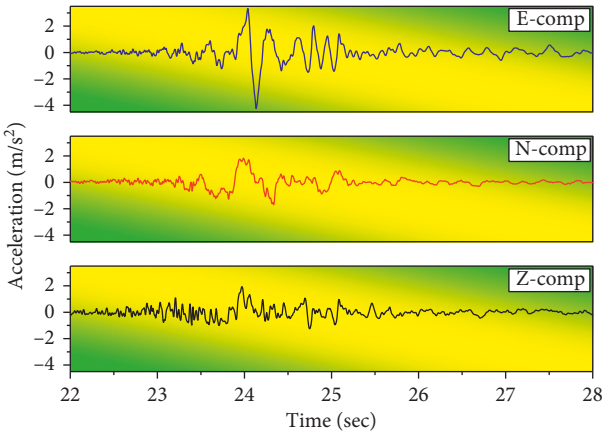

Figure 4: Acceleration history of Norcia Earthquake [20].

nonlinearity tolerance in Norcia Earthquake. However, due to these reasons, the E comp has been selected for numerical analysis. The mechanical properties of materials have been used in this analysis, extracted from those reported in the literature, and are shown in Table 1. The soil is often discretized with solid finite elements. Nonlinear numerical analysis has been performed based on realistic seismic data. The earthquake data have been used in numerical analysis and are reported by AMATRICE station, with 8.9 (km) distance from the epicenter of the earthquake. The Norcia Earthquake occurred with 6.2 magnitude, at the location of 42.71 N 13.17 E, and depth of 10.0 km, on 1 : 36 : 33 UTC, 24 August 2016.

5. Numerical Analysis, Discussion, and Verification of the Result

Enhancement geometry of a concrete footing considerably changes soil-footing seismic interaction mechanism, and this process leads to develop a new concept for the satisfactory seismic design of a concrete footing. The morphology

Table 1: Mechanical properties of materials [21, 22].

Materials	Modulus elasticity, E (MPa)	Poisson's ratio, (ν)	Friction angle, ϕ (degree)	Dilatancy angle, ψ (degree)	Cohesion, c (kPa)	Unit weight, γ (kN/m^3)	Ref
Soil	120	0.35	53	21	0.01	22.68	[21]
Concrete	49195	0.24	—	—	—	24.405	[22]

of concrete footing influences on the shear strain travel paths and seismic energy distribution. The meaningful relationships have been observed between simulated near-fault ground-shaking and energy dissipation mechanism at each configuration. The characteristics of seismic waves are altered as it is facing different simulated geomorphological conditions. The seismic wave dispersion modifies damping ratio and governs nonlinear deformation patterns of soil foundation and footing-soil seismic interaction mechanism. However, the morphology of concrete footing significantly affects the amplitude of earthquake ground motions; it may be known as "geomorphological conditions effect" in concrete footing-soil foundation seismic design. The numerical analysis results have confirmed that the geomorphological condition influence to strain energy dissipation, and this process leads to developing nonlinear deformation patterns and differential settlement with the specific shape at each configuration, and subsequently, it is understood that the geomorphological conditions are important in the distribution of earthquake damage. The flexible soil foundation area-to-ridge concrete footing area interaction is responsible for the failure mechanism of soil foundation at each configuration. However, the design of concrete footing shape at each configuration is important in the stability of concrete footing and soil foundation as well. The modified shape of concrete footing leads to change in the concrete footing center of gravity and shape of cyclic load distribution; this phenomenon results in the modification of concrete footing-soil foundation seismic interaction mechanism and seismic load response. And on the other hand, the geomorphological conditions and morphology of concrete footing are responsible for developing characteristics of strain paths, and the strain path is a factor in developing a differential settlement, failure mechanism, deformation, and bearing capacity. The seismic site response is highly variable with respect to concrete footing morphology, while the volume of used concrete is equal in both configurations, and cost effectiveness of the project is considered with seismic design of concrete footing. The geotechnical condition is another factor in ground motion behavior prediction. The geomorphological condition affects the seismic response of an infrastructure. It can suggest beyond the theoretical seismic design; it requires to numerically simulate the influence of geomorphological conditions to predict seismic stability of the infrastructure. The near-fault ground motions change strain energy dissipation via travel path of seismic wave propagation. The hysteretic behavior of soil significantly affects the concrete footing seismic response. This process affects concrete footing and soil foundation inertial interaction and leads to stress response of the soil foundation. Cyclic seismic load response has been developed due to concrete footing morphology, and it is shown in Figures 5 and 6. The seismic loading and concrete footing

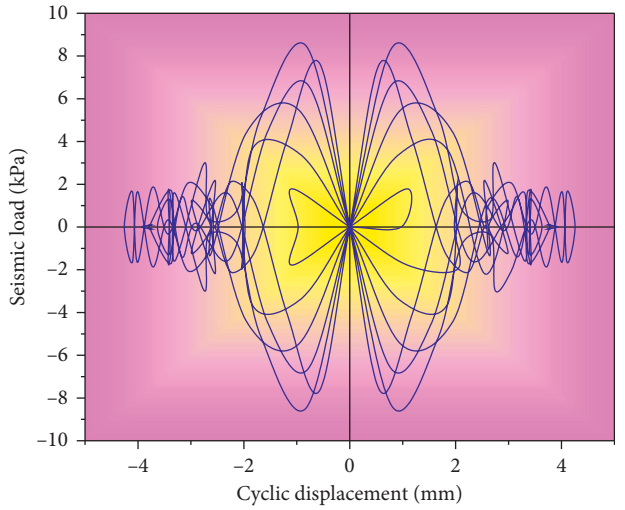

Figure 5: Seismic load (kPa) vs cyclic displacement (mm) at the base of a concrete footing, configuration-1.

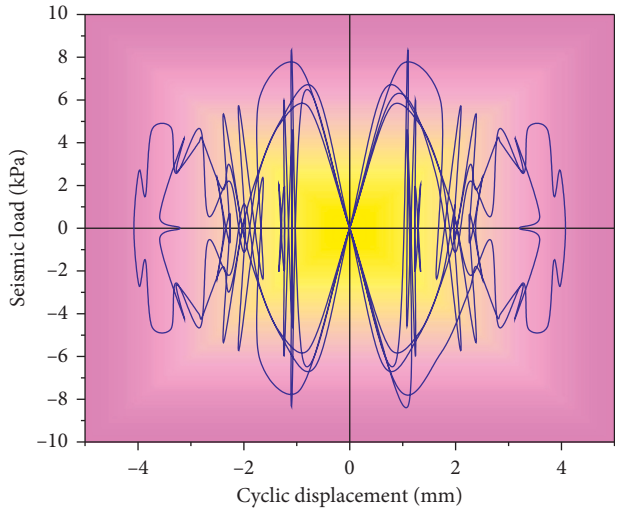

Figure 6: Seismic load (kPa) vs cyclic displacement (mm) at the base of a concrete footing, configuration-2.

morphology are responsible for soil compaction, modify soil foundation shear strength, and alter concrete footing-soil foundation seismic interaction mechanism. The geomorphological conditions affect wave motion behavior, and it causes differential ground deformation and differential rotations of concrete footing along its base to interact with soil foundation. The wave energy propagates in different directions and results in forming cyclic volumetric strain and produces nonlinear deformation for each configuration; it is shown in Figures 7 and 8. In configurations 1 and 2, the different ground motions response has been observed; it

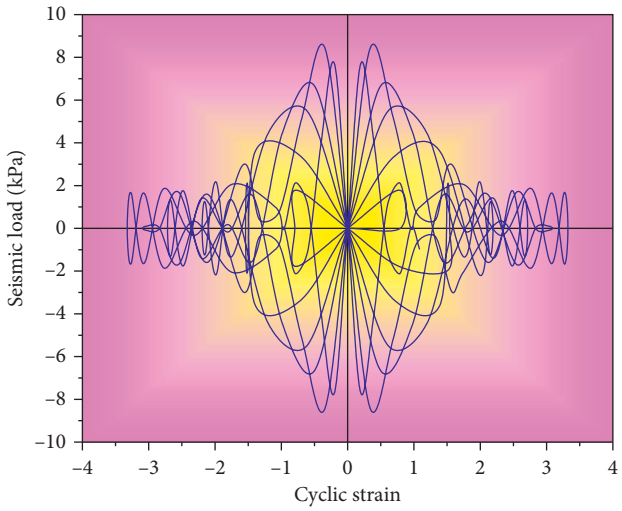

Figure 7: Seismic load (kPa) vs cyclic strain at the base of a concrete footing, configuration-1.

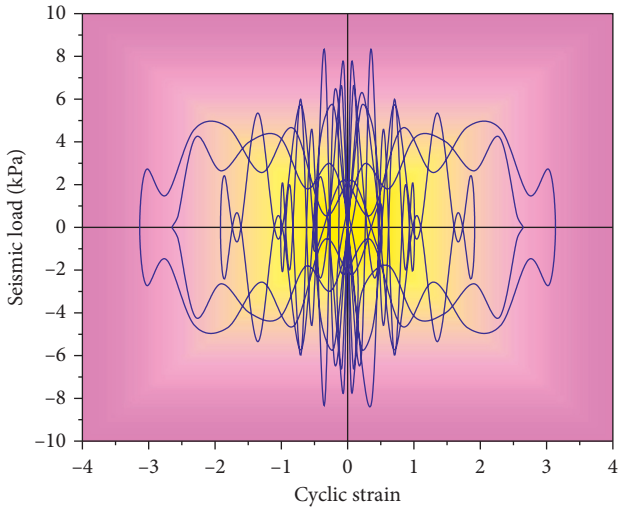

Figure 8: Seismic load (kPa) vs cyclic strain at the base of a concrete footing, configuration-2.

developed with respect to concrete footing shape, and this phenomenon supports in earthquake damage estimation, when the movement of seismic wave radiates along the base and sides of the concrete footing. The seismic wave radiate dislocates the concrete footing at any possible directions, and this phenomenon results in accelerating model and releasing cyclic strain energy. The hysteretic energy dissipation is scattered in all configurations, with the critical mechanism in respect to the flexible the soil foundation area-to-the ridge concrete footing area interaction; this mechanism is responsible for failure mechanism of soil foundation at each configuration. Inertia has been developed due to near-fault ground motions applied to each configuration; it has appeared in the form of base shear, moment, and torsional excitation and causes differential displacements and nonlinear deformation rotation, with a different magnitude in respect to the soil foundation flexibility and concrete footing shape. The damping ratio in configuration-2 is reduced by 15% compared to configuration-1. The shape of concrete footing governs hysteretic soil damping and inertial interaction; this process occurs based on kinematic interaction of concrete footing-soil foundation characteristics and causes concrete foundation motions in soil foundation. The nonlinear deformation significantly influences the overall concrete footing seismic behavior, especially with respect to damping and seismic degrees of damage.

The stress third invariant behavior is depicted in Figures 9–12. A comparative numerical analysis of the seismic response between two differently shaped and equal volume of concrete footing under significantly invariant stresses through establishing nonlinear finite element analysis has been made. The stress third invariant at the base of concrete footing for configuration-1 is formed with higher strain energy and lower energy dissipation magnitude compared to configuration-2. This complex mechanism influences load carry capacity of soil foundation and types of earthquake damage. The evaluated results show that the shearing resistance at configuration-2 is improved due to lower degradation of soil by cyclic loading. The nonlinear seismic load-cyclic strain curve expresses the variation of stiffness and shear strength at the base of the concrete footing. The cyclic strain energy causes increasing nonlinear shear deformation and soil foundation failure if cyclic shear stress increases more than the shear strength of the soil foundation. Figure 9 shows the stress invariant at the base of concrete footing for configurations 1 and 2. As a result, the cyclic strain behavior would be expected to provide a more reliable prediction of differential settlement, in considering concrete footing-soil foundation seismic interaction. The nonlinear seismic load-cyclic strain relationship at both configurations shows the higher strain energy concentration is developed at the base of the configuration-1, with respect to the magnitude and shape of the seismic loading. However, the differential settlement is significantly minimized in configuration-2. The higher cyclic strain energy concentration has a direct relationship with nonlinear shear deformation and nonlinear volume change. The failure patterns are plotted in Figure 9, in such a way that red and blue zone implies a fully plastic state. Due to the nature of cyclic loading, nonplastic deformation occurred in any possible direction. The geometry of the failure patterns shows the plastic slice has been occupied more area in configuration-1. The plastic deformation morphology shows that the differential settlement for both models is not the same, and a higher magnitude of differential settlement occurred in configuration-1.

Figures 10 and 11 show the cyclic stress behavior of the configurations 1 and 2 in respect to the size and shape of the plastic deformation. And it describes increment of cyclic stress invariant. The stronger response of earthquake shaking in the configuration-1 has been observed. However, it is a possibility for permanent deformation in configuration-1. The strong strain in several parts of the configuration-1 results in permanent nonlinear shear deformations and nonlinear volume change. The nonlinear volumetric strain often refers to ground failure. It is the

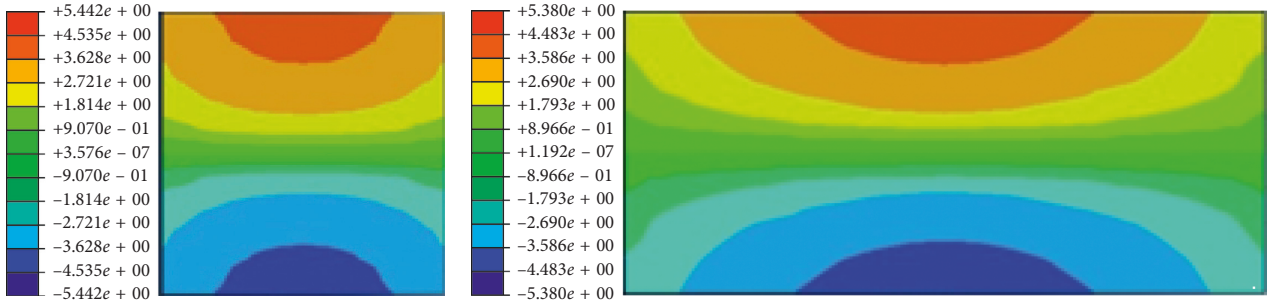

Figure 9: Cyclic stress invariant at the base of the concrete footing. (a) Configuration-1. (b) Configuration-2.

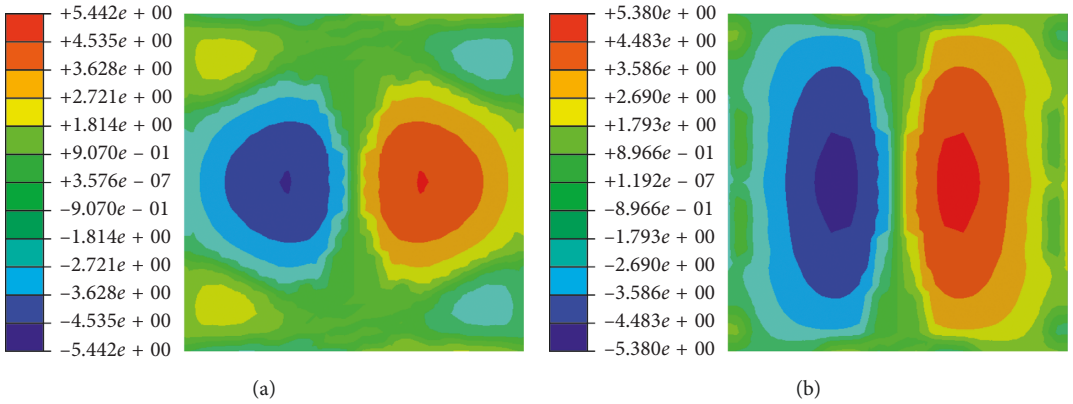

Figure 10: Cyclic stress invariant at the base of the soil foundation. (a) Configuration-1. (b) Configuration-2.

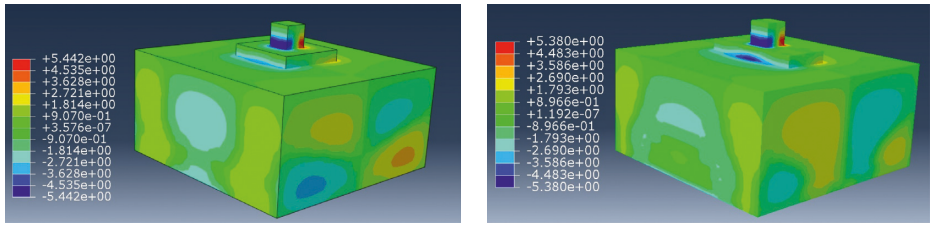

Figure 11: Cyclic stress invariant for configurations 1 and 2. (a) Configuration-1. (b) Configuration-2.

possibility of ground failure in the form of lateral ground displacement, and it can contribute to the failure of the soil foundation.

Color map surface projection techniques are used in matrix analysis to simulate results of ABAQUS software, which is reported in cyclic stress invariant. According to Figure 12, by using the matrix in numerical simulation, the development of cyclic stress invariant due to seismic acceleration load response at the base of the soil foundation is illustrated. Figure 12 shows the seismic load travel paths and seismic load directions. The loading and reloading process has been depicted in different colors. The load distribution among two soil foundations is varied; configuration-2 is subjected to more distributed cyclic load compared to configuration-1; it is a result of increasing stable soil-concrete footing interaction in configuration-2. It can be concluded that the stability of configuration-2 is higher than configuration-1.

The minimum strain energy density allows the influence of the T-stress on the mixed modes I/II fracture strength [23]. And the specimen geometry can strongly influence the mode-I fracture strength [24]. The hysteretic energy dissipation influences the flexible soil foundation area-to-the ridge concrete footing area interaction and governs failure mechanism. The configurations 1 and 2 affect strain energy dissipation, according to their geometry. The results of the numerical analysis show good agreements with those reported in the literature.

The different types of loads can store elastic energy before damage, and this energy storage accelerates and develops damage mechanism [25–33]. In the present numerical analysis, it has been observed that the shape of

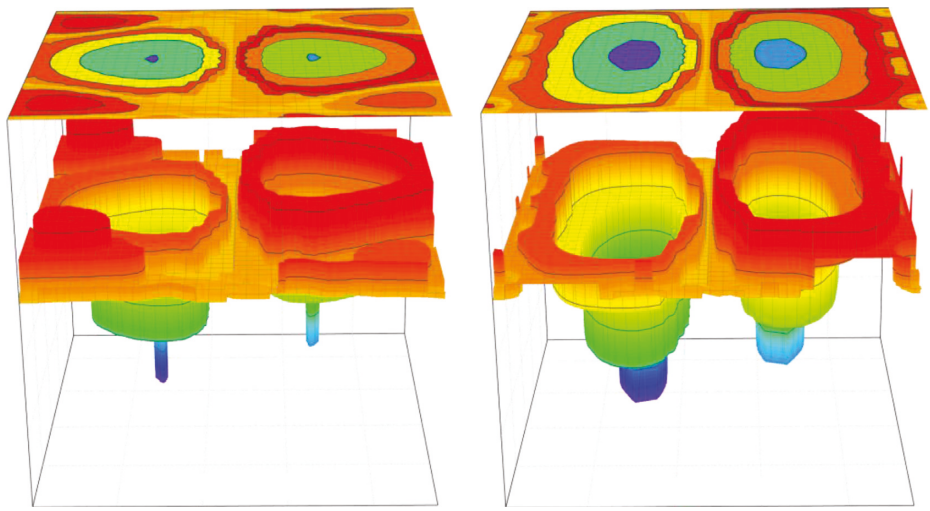

(a) (b)

Figure 12: 3D cyclic stress invariant of soil at the base of soil foundation, using matrix for numerical simulation. (a) Configuration-1. (b) Configuration-2.

concrete footing causes storage strain energy mechanism and strain energy dissipation as well. The cyclic strain energy causes deformation, with respect to the shape of the concrete footing. The soil foundation was subjected to the seismic excitation and deforms. This deformation occurs according to an internal energy mechanism and concrete footing shape. This internal energy is known as strain energy. In the present study, the strain energy has more been dissipated with artistic concrete footing design. The configuration of soil foundation-concrete footing significantly modified strain energy storage and damage patterns. The stress component distribution due to the external forces depends on the strain energy function. However, the shape of concrete footing directly affects seismic acceleration response, damping mechanism, energy dissipation, load carry capacity, differential settlement, nonlinear deformation, strain-stress travel paths, and inertial interaction.

6. Conclusion

The nonlinear finite elements are applied in the analysis of concrete footing-soil seismic interaction mechanism. The concrete footing is built up with two different shapes and equal volume. The simulated near-fault ground motions have been applied to each configuration. In the present study, the following aims have been achieved:

(i) It has been found that the concrete footing-soil interaction and morphology of differential settlement have been changed with respect to the shape of the concrete footing.

(ii) The local geotechnical conditions have been modified ground-shaking characteristics. The anomalous damage distributions may not derive with the select appropriate shape of a concrete footing, considering local site conditions.

(iii) The morphology of concrete footing affects the seismic energy travel paths, and meaningful relationships have been observed between simulated near-fault ground-shaking and energy dissipation mechanism. The strain energy has more been dissipated with artistic concrete footing design.

(iv) The shape of concrete footing governs hysteretic soil damping and inertial interaction; these processes have occurred based on kinematic interaction of concrete footing-soil foundation characteristics.

(v) The higher strain energy concentration has been observed at the base of the configuration-1, with respect to the magnitude and shape of the seismic loading response. The differential settlement is significantly minimized in configuration-2.

(vi) The cyclic strain causes plastic cyclic deformation, with respect to the shape of concrete footing and related to increment of stress. According to the numerical results, this approach supports in forecasting the seismic stability of concrete footing.

Data Availability

No data were used to support this study.

Conflicts of Interest

The authors declare that they have no conflicts of interest.

Acknowledgments

The support by the Major Projects of Natural Science Research in Jiangsu Colleges and Universities (grant no. 17KJA560001), the Science and Technology Planning Project of Jiangsu Province (grant no. BY2016061-29), the Jiangsu Province Six Talent Peak High-Level Talent Project (grant no. JZ-011), and the New Wall Materials and Development of Bulk Cement Projects of Jiangsu Economic and Information Commission (grant no. 2017-21) is greatly acknowledged.

References

[1] A. Namdar and M. K. Pelkoo, "Numerical analysis of soil bearing capacity by changing soil characteristics," *Frattura ed Integrità Strutturale*, vol. 3, no. 10, pp. 38–42, 2009.

[2] A. Namdar, "Liquefaction zone and differential settlement of cohesionless soil subjected to dynamic loading," *EJGE*, vol. 21, no. 2, pp. 593–605, 2016.

[3] A. Namdar and G. S. Gopalakrishna, "Seismic mitigation of embankment by using dense zone in subsoil," *Emirates Journal for Engineering Research*, vol. 13, no. 3, pp. 55–61, 2008.

[4] O. F. Drbe and M. H. El Naggar, "Axial monotonic and cyclic compression behaviour of hollow-bar micropiles," *Canadian Geotechnical Journal*, vol. 52, no. 4, pp. 426–441, 2014.

[5] A. V. Rose, R. N. Taylor, and M. H. El Naggar, "Numerical modelling of perimeter pile groups in clay," *Canadian Geotechnical Journal*, vol. 50, no. 3, pp. 250–258, 2013.

[6] A. Namdar, "Tsunami and liquefaction resistance of subsoil," *Electronic Journal of Geotechnical Engineering*, vol. 18, pp. 5907–5919, 2013.

[7] H. Toyota and S. Takada, "Geotechnical distinction of landslides induced by near-field earthquakes in niigata, Japan," *Geography Journal*, vol. 2015, Article ID 359047, 11 pages, 2015.

[8] A. Y. Abd Elaziz and M. H. El Naggar, "Geotechnical capacity of hollow-bar micropiles in cohesive soils," *Canadian Geotechnical Journal*, vol. 51, no. 10, pp. 1123–1138, 2014.

[9] A. M. Alnuaim, M. H. El Naggar, and H. El Naggar, "Numerical investigation of the performance of micropiled rafts in sand," *Computers and Geotechnics*, vol. 77, pp. 91–105, 2016.

[10] J. Kumar and V. B. K. Mohan Rao, "Seismic bearing capacity factors for spread foundations," *Géotechnique*, vol. 52, no. 2, pp. 79–88, 2002.

[11] D. Chakraborty and J. Kumar, "Seismic bearing capacity of shallow embedded foundations on a sloping ground surface," *International Journal of Geomechanics*, vol. 15, no. 1, article 04014035, 2015.

[12] A. Namdar, "A numerical investigation on soil-concrete foundation interaction," *Procedia Structural Integrity*, vol. 2, pp. 2803–2809, 2016.

[13] A. D. Santis, O. D. Bartolomeo, D. Iacoviello, and F. Iacoviello, "Quantitative shape evaluation of graphite particles in ductile iron," *Journal of Materials Processing Technology*, vol. 196, no. 1–3, pp. 292–302, 2008.

[14] A. Namdar, E. Darvishi, X. Feng, and Q. Ge, "Seismic resistance of timber structure—a state of the art design," *Procedia Structural Integrity*, vol. 2, pp. 2750–2756, 2016.

[15] R. Ali, Q. Z. Khan, and A. Ahmad, "Numerical investigation of load-carrying capacity of GFRP-reinforced rectangular concrete members using CDP model in ABAQUS," *Advances in Civil Engineering*, vol. 2019, Article ID 1745341, 21 pages, 2019.

[16] A. Namdar, Y. Dong, and Y. Liu, "The effect of nonlinearly of acceleration histories to timber beam seismic response," *Material Design and Processing Communication*, 2019, In press.

[17] S. Frank, Ó. R. Ramos, J. P. Reyes, and M. J. Pantaleón, "Relative displacement method for track-structure interaction," *The Scientific World Journal*, vol. 2014, Article ID 397515, 7 pages, 2014.

[18] A. S. Genikomsou and M. A. Polak, "Finite element analysis of punching shear of concrete slabs using damaged plasticity model in ABAQUS," *Engineering Structures*, vol. 98, pp. 38–48, 2015.

[19] D. W. A. Rees, *Basic Engineering Plasticity*, Elsevier, Amsterdam, Netherlands, 2006.

[20] https://strongmotioncenter.org/.

[21] Y. Yu, R. J. Bathurst, and T. M. Allen, "Numerical modelling of two full-scale reinforced soil wrapped-face walls," *Geotextiles and Geomembranes*, vol. 45, no. 4, pp. 237–249, 2017.

[22] J. Li, C. Wu, and H. Hao, "An experimental and numerical study of reinforced ultra-high performance concrete slabs under blast loads," *Materials & Design*, vol. 82, pp. 64–76, 2015.

[23] M. R. Ayatollahi, M. Rashidi Moghaddam, and F. Berto, "A generalized strain energy density criterion for mixed mode fracture analysis in brittle and quasi-brittle materials," *Theoretical and Applied Fracture Mechanics*, vol. 79, pp. 70–76, 2015.

[24] M. R. Ayatollahi, M. Rashidi Moghaddam, S. M. J. Razavi, and F. Berto, "Geometry effects on fracture trajectory of PMMA samples under pure mode-I loading," *Engineering Fracture Mechanics*, vol. 163, pp. 449–461, 2016.

[25] S. You, H. Ji, Z. Zhang, and C. Zhang, "Damage evaluation for rock burst proneness of deep hard rock under triaxial cyclic loading," *Advances in Civil Engineering*, vol. 2018, Article ID 8193638, 7 pages, 2018.

[26] L. Chen, L. Qiao, J. Yang, and Q. Li, "Laboratory investigation of energy propagation and scattering characteristics in cylindrical rock specimens," *Advances in Civil Engineering*, vol. 2018, Article ID 2052781, 7 pages, 2018.

[27] Z. Wang, J. Yao, N. Tian, J. Zheng, and P. Gao, "Mechanical behavior and damage evolution for granite subjected to cyclic loading," *Advances in Materials Science and Engineering*, vol. 2018, Article ID 4312494, 10 pages, 2018.

[28] B. H. Osman, X. Sun, Z. Tian, H. Lu, and G. Jiang, "Dynamic compressive and tensile characteristics of a new type of ultra-high-molecular weight polyethylene (UHMWPE) and polyvinyl alcohol (PVA) fibers reinforced concrete," *Shock and Vibration*, vol. 2019, Article ID 6382934, 19 pages, 2019.

[29] A. Reyes-Salazar, E. Bojórquez, Juan Bojorquez, F. Valenzuela-Beltran, and M. D. Llanes-Tizoc, "Energy dissipation and local, story, and global ductility reduction factors in steel frames under vibrations produced by earthquakes," *Shock and Vibration*, vol. 2018, Article ID 9713685, 19 pages, 2018.

[30] E. Bojorquez, A. Reyes-Salazar, A. Teran-Gilmore, and S. E. Ruiz, "Energy-based damage index for steel structures," *Steel & Composite structures*, vol. 10, no. 4, pp. 331–348, 2010.

[31] B. Dadfar, M. H. El Naggar, and M. Nastev, "Vulnerability of buried energy pipelines subject to earthquake-triggered transverse landslides in permafrost thawing slopes," *Journal of Pipeline Systems Engineering and Practice*, vol. 9, no. 4, article 04018015, 2018.

[32] N. Bonora, D. Gentile, P. P. Milella, G. Newaz, and F. Iacoviello, "Ductile damage evolution under different strain rate conditions," *ASME*, vol. 246, pp. 145–154, 2000.

[33] L. Susmel, F. Berto, and Z. Hu, "The strain energy density to estimate lifetime of notched components subjected to variable amplitude fatigue loading," *Frattura ed Integrità Strutturale*, vol. 13, no. 47, pp. 383–393, 2019.

Hindawi
Advances in Civil Engineering
Volume 2019, Article ID 9710529, 12 pages
https://doi.org/10.1155/2019/9710529

Research Article

Performance of the Cold-Bending Channel-Angle Buckling-Restrained Brace under Cyclic Loading

Kun Wang,[1,2] **Junwu Xia**,[1,2] **Xiaomiao Chen**,[1] **Bo Xu**,[1] **Xiangzhou Liang**,[1] **and Jian Wang**[1]

[1]*Jiangsu Key Laboratory of Environmental Impact and Structural Safety in Engineering, China University of Mining and Technology, Xuzhou, Jiangsu 221116, China*
[2]*Jiangsu Collaborative Innovation Center for Building Energy Saving and Construction Technology, Xuzhou, Jiangsu 221116, China*

Correspondence should be addressed to Junwu Xia; xiajunwu100@163.com

Received 2 January 2019; Accepted 10 March 2019; Published 1 April 2019

Academic Editor: Jorge Ruiz-García

In this study, three restricted cold-bending channel-angle buckling-restrained brace (CCA-BRB) specimens were experimentally characterised by a low-reversed cyclic loading test. Three specimens had steel cores with cruciform cross section. Two restraining units were assembled to form an external constraint member, each of which was composed of an equilateral cold-bending channel and two equilateral cold-bending angles via welding. A gap or a thin silica gel plate was set between the internal core and the external constraint member to form an unbonded layer. Several evaluation parameters on the seismic performance, hysteretic behaviour, and energy dissipation capability of the CCA-BRB was investigated, including hysteresis curve, skeleton curve, compression strength adjustment factor, measured and computed stiffness, energy dissipation coefficient, equivalent viscous damping ratio, ductility coefficient, and cumulative plastic deformation. The test results and evaluation indices demonstrated that the hysteretic performance of braces with a rigid connection was stable. A Ramberg–Osgood model and two model parameters were calibrated to predict, with fidelity, the skeleton curve of CCA-BRB under cyclic load. The initial elastic stiffness of the brace used in practice should contain overall portions of the brace instead of the yielding portion of the brace. Finally, all the tested CCA-BRBs exhibited a stable energy absorption performance and verified the specimens' construction was rational.

1. Introduction

As a kind of structure system with excellent ductility, the braced frame is often used in seismic structures. However, the general brace itself will suffer from comprehensive problems such as strength stiffness degradation and low-cycle fatigue fracture after buckling when under the action of cyclic load. A buckling-restrained brace (BRB) is an energy dissipation damper of metal yielding which has advantages of stable energy dissipation capacity, easy construction and fabrication with low cost, etc. [1]. A BRB can provide stable lateral stiffness and load-carrying capacity for a frame structure. As a result, BRBs have been used extensively in existing and new structures to enhance the earthquake resistance [2–6].

Diverse experiments show that BRBs have a substantial energy absorption capability under cyclic loading [7, 8]. In 1976, an early buckling-restrained attempt to propose a brace with dissipating energy yet does not buckle was reported in an experimental study [9]. The brace consisted of a single flat plate as the internal core and a square steel pipe filled with mortar as the external constraint member. Since then, various structural forms and experimental studies of traditional BRBs were proposed by investigators around the world [10–13]. However, there were a series of issues affecting the traditional BRBs, in which the core buckling restrained by steel tube filled with concrete or mortar, such as the need for higher precision control between the external concrete member and the core steel member, and the complex processes of wet concrete pouring, further

increasing the complexity of component fabrication and prolonging the production cycle. Based on the above reasons, scholars have put forward various forms of all-steel BRBs [14–21], which only require clamping the inner core with section steel or composite steel members to impose constraints, and the all-steel BRBs have the advantages of simple construction, convenient assembly, and lighter weight. Kuwahara et al. proposed the first representative all-steel buckling-restrained brace in 1993 of which circular steel tubes were used to support the inner core (the inner circular tube) and the outer constraint members (the outer circular tube) [14]. The all-steel BRBs had steel cores with rectangular cross sections and were studied through a uniaxial test program [15] or subassemblage testing [16, 17]. The all-steel BRBs with cruciform cross-section core are generally used to provide large lateral restraint force to frame structures, and several axial cycle tests have been conducted to study the hysteresis behaviour of the all-steel BRBs with cruciform cross-section core [18–21]. In addition, several shaking table tests have been conducted on concrete and steel frames equipped with BRBs [22, 23]. A novel type of BRB, called cold-bending channel-angle buckling-restrained brace (CCA-BRB), has been proposed and tested by the authors. This paper describes the characteristics, hysteresis behaviour, and energy dissipation capability of the new BRB.

2. Layouts of the CCA-BRB

Each CCA-BRB consists of an internal steel core, external constraint members, and an unbonded layer between them (Figure 1). The steel core is subjected to the axial load while constraint members provide lateral support to the steel core and prevent the core from buckling. The external constraint members of the CCA-BRB are composed of two restraining units, each of which consists of an equilateral cold-bending channel and two equilateral cold-bending angles via welding (Figure 2). The ratio of web height to flange plate width of the channel is 2 : 1. Each CCA-BRB has the steel core with cruciform cross section which consists of three portions: a yielding portion, a transition portion, and a connection portion (Figure 3). A gap must be present between the internal core and the external constraint members while the gap can be adjusted to form an unbonded layer. The thin layer of unbonded material along the internal steel core eliminates shear transfer during the elongation and contraction of the core and also accommodates its lateral expansion when in compression.

Figure 3 shows the cross-sectional schematic diagram of the CCA-BRB and the dimension parameters: h_c denotes the width and t_c the thickness of the steel core; h_{cc} denotes the web height, b_{cc} the flange width, and t_{cc} the thickness of the cold-bending channel steel; h_{ca} denotes the vertical limb height, b_{ca} the horizontal width and t_{ca} the thickness of the cold-bending angle steel.

3. Component Testing

3.1. Specimen Design. The geometric dimension parameters of the specimens are listed in Table 1, and the meaning of each parameter is shown in Figure 3, in which L_y represents the yielding portion length of the core, L_{tr} the transition portion length of the core, L_{con} the connection portion length of the core, L_{total} the total length of the core, and L_{em} the length of the external constraint members.

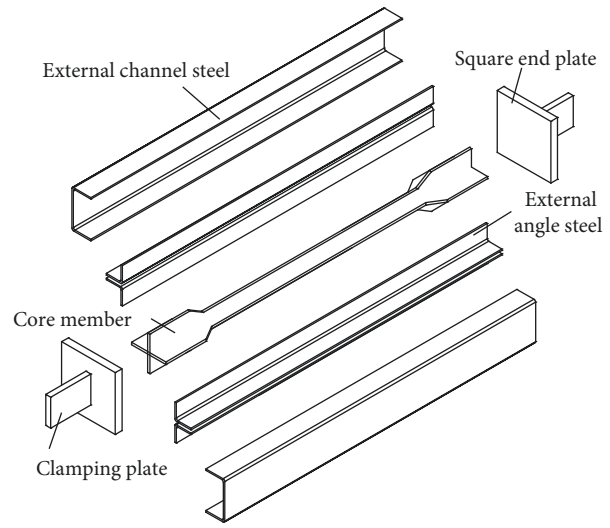

Figure 1: Exploded view of the CCA-BRB.

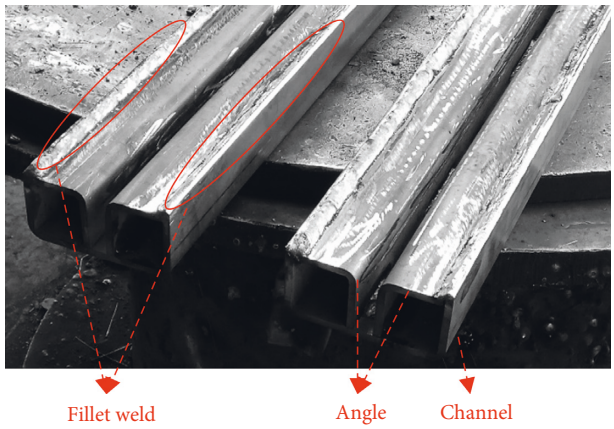

Figure 2: Diagram of the restraining units via welding.

A construction drawing of the BRB-1 specimen is shown in Figure 4. The internal steel core of CCA-BRB is composed of three flat plates via full-fillet welding by carbon dioxide arc welding. The core of CCA-BRB was a Q235 steel member with a variable cross section, in which the dimensions of the yielding portion section were 68 mm × 68 mm × 8 mm and connection portion section 128 mm × 128 mm × 8 mm. The yielding portion length L_y of the core was 800 mm, the transition portion length L_{tr} 100 mm (50 mm on each side), the connection portion length L_{con} 300 mm (150 mm on each side), and the total length of the core L_{total} 1200 mm. The external restraining members of CCA-BRB are composed of two cold-bending channels and four cold-bending angles in which all components were made of Q235 steel. The cross-section dimensions of the channel were 140 mm × 70 mm × 5 mm and the angle 60 mm × 60 mm × 5 mm. The

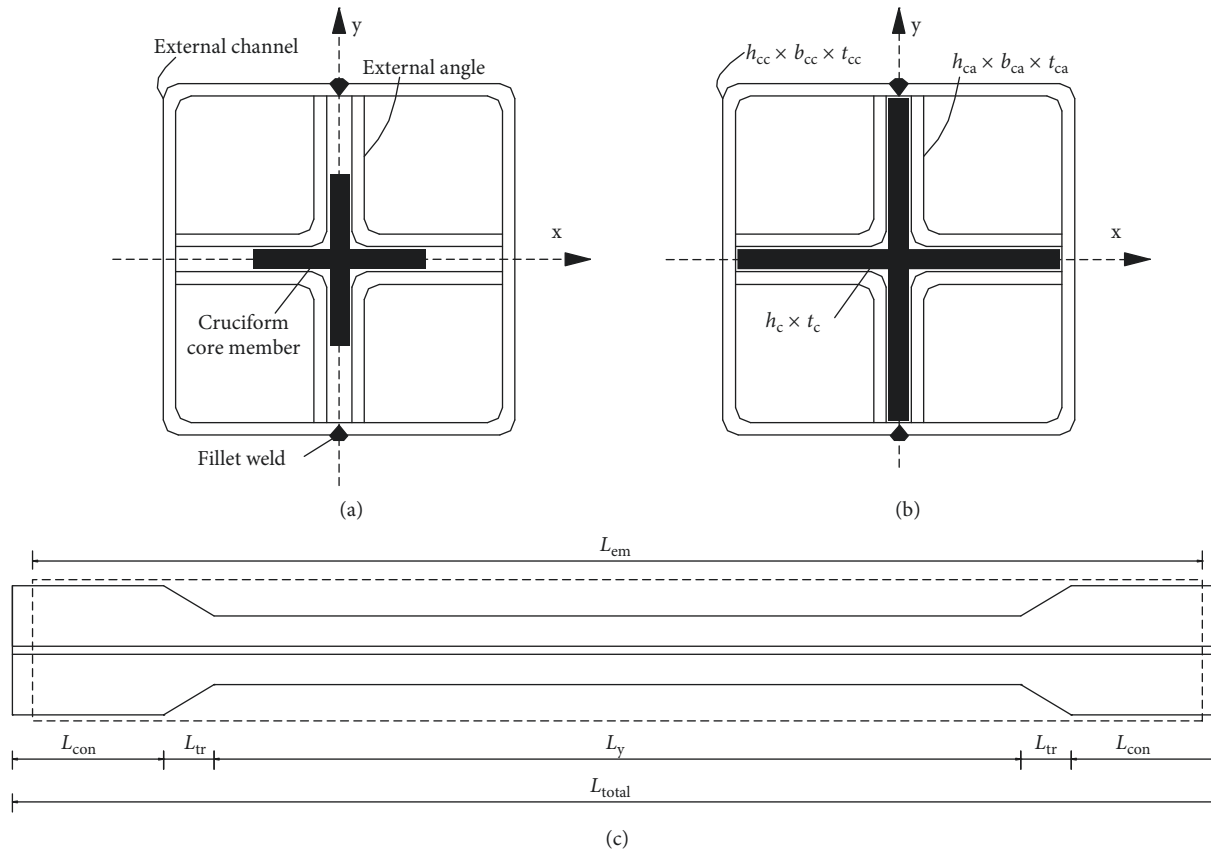

Figure 3: Schematic diagram of the CCA-BRB. (a) Midspan section; (b) end section; (c) dimensions of the CCA-BRB.

Table 1: Geometric dimension parameters and loading protocol of the specimens.

Specimen	$h_c \times t_c$ (mm)	$h_{cc} \times b_{cc} \times t_{cc}$ (mm)	$h_{ca} \times b_{ca} \times t_{ca}$ (mm)	L_y (mm)	L_{tr} (mm)	L_{con} (mm)	L_{total} (mm)	L_{em} (mm)	Loading protocol
BRB-1	68×8	$140 \times 70 \times 5$	$60 \times 60 \times 5$	800	50	150	1200	1160	Loading protocol 1
BRB-2	68×8	$140 \times 70 \times 5$	$60 \times 60 \times 5$	800	50	150	1200	1160	Loading protocol 2
BRB-3	68×8	$140 \times 70 \times 5$	$60 \times 60 \times 5$	800	50	150	1200	1160	Loading protocol 3

design length of all restraining components L_{em} was 1160 mm which is shorter than the core 40 mm; that is, each side is reserved the axial compression space of 20 mm to meet the 2% compressive strain (each end splits an average of 1% deformation) of the core and left a certain margin to consider the machining error. Each channel and two angles were bound via fillet welds.

Note that 1 mm gap was set between the internal core and the external constraint members of the specimens on each side with pasting 1-millimeter-thick silica gel plate along the yielding portion of the core to reduce the friction when in compression. A 25-millimeter-thick square plate was welded at the end of the core via full penetration weld, and the dimensions of the plate were 200 mm × 200 mm. Based on the realistic consideration of the test fixture, a 18-millimeter-thick holding plate (the dimensions of the holding plate were 150 mm × 100 mm) and the square end plate were bound via fillet weld to form a fixed joint to satisfy test loading.

3.2. Experimental Setup. Figure 5 indicates the experimental setup of the specimens. Both the ends of the specimens are connected to a PWS-500 electrohydraulic servo actuator at the Jiangsu Key Laboratory of Environmental Impact and Structural Safety in Engineering of China University of Mining and Technology by which an axial cyclic load was applied. The actuator had a cyclic load capacity of ±500 kN and a displacement capacity of ±200 mm. To observe the axial deformation, two displacement meters were set at the upper end of the specimens and two at the lower end.

3.3. Loading Protocol. The loading protocols adopted in this low-reversed cyclic loading test are shown in Figure 6. The parameter used to define the test program was the core axial strain, and three loading protocols were adopted corresponding to three specimens. Corresponding to the specimen BRB-1, two loading cycles were performed to an amplitude increment in the core axial strains of 0.5%, 1.0%,

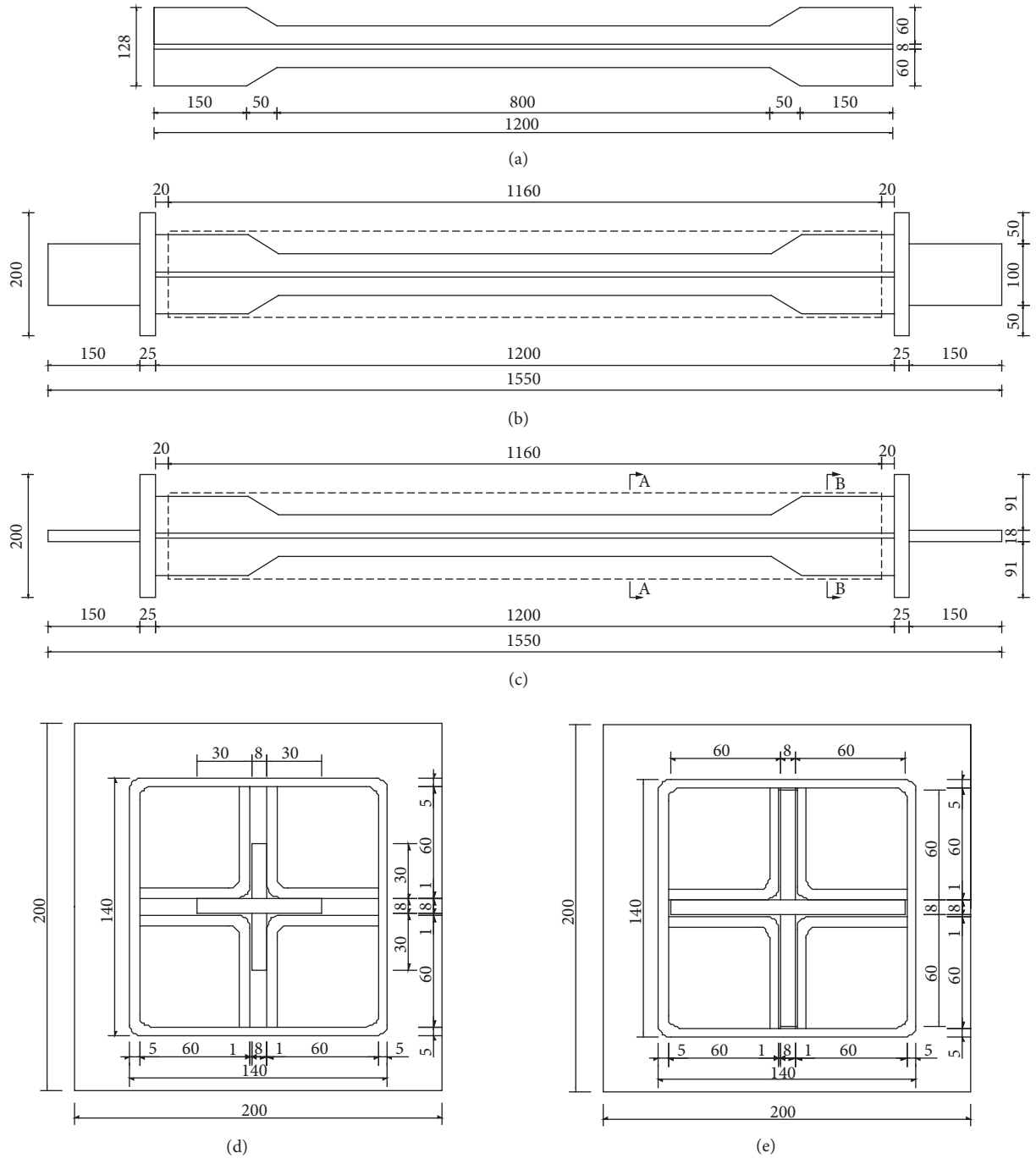

Figure 4: Construction drawing of the BRB-1. (a) Steel core; (b) top view; (c) front view; (d) A-A section; (e) B-B section.

and 1.5% followed by five loading cycles of 2% strain to complete the experiment (see the loading protocol 1). Corresponding to the specimen BRB-2, two loading cycles were performed with 0.5%, 1.0%, and 1.5% core axial strain followed by five loading cycles of 2% strain to complete the experiment (see the loading protocol 2). The difference of loading protocols between BRB-1 and BRB-2 was the loading type of BRB-1 traction after compression and BRB-2 compression after traction. According to the requirements of GB50011-2010 [24], the parameter corresponding to the specimen BRB-3 was defined at levels of 1/300, 1/200, 1/150, and 1/100 bracing length under tension-compression three times (see the loading protocol 3). On the basis of the loading protocols, when the specimens BRB-1 and BRB-2 completed five 2% axial strain loadings, the value of CPD, which is a normalized expression of the cumulative plastic deformation, was measured at 212 which satisfies the plastic deformation capability requirements on the BRB specified in ANSI/AISC 341-10 [25]. The core axial displacement loading protocol of each specimen is shown in Table 2. The core

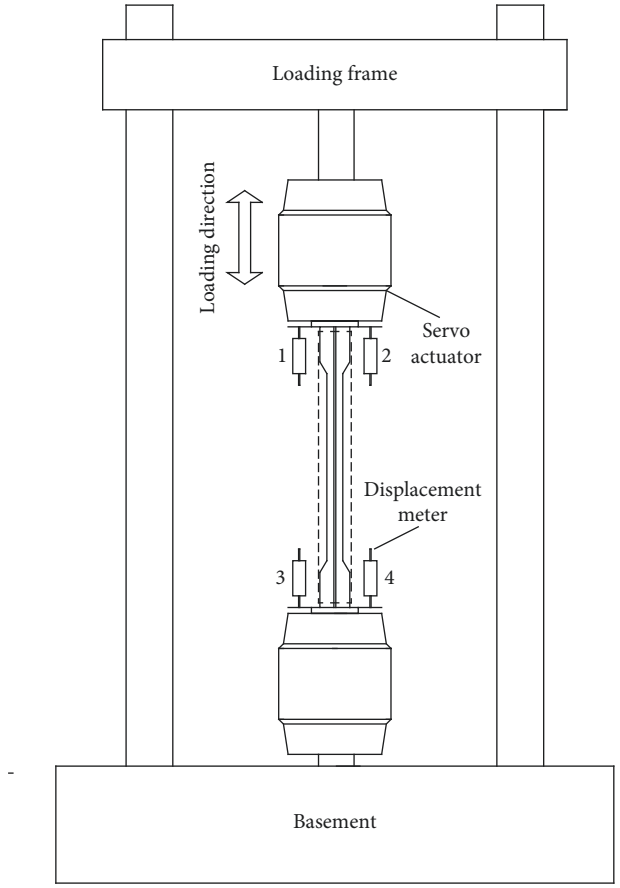

Figure 5: Experimental setup schematic diagram.

length was 1200 mm, and the core yielding portion length was 800 mm.

3.4. Material Properties. Based on the request of GB/T228.1-2010 [26], the material properties tests of the internal steel core and external constraint members of varying thicknesses were measured. The corresponding material property index is shown in Table 3, in which E denotes elastic Young's modulus, f_y the steel yield strength, f_u the steel tensile strength, and f_y/f_u the steel yield-tensile strength ratio.

4. Test Results and Performance Analysis

4.1. Hysteresis Curve. The hysteresis curves of the specimens are plotted with the recorded axial force in the brace as ordinate against the axial displacement measured across the entire brace including connections as abscissa (Figure 7). The vertical coordinate is the measured axial load of the specimens, and its sign convention is positive tension and negative compression. The horizontal coordinate is the measured axial deformation, and the sign convention is the same. It is noteworthy that the flexibility of the connections contributes only slightly to the overall displacement; further, the axial deformation measured by the displacement meter mainly reflects the axial deformation of the yielding segment of the brace.

The hysteresis loops resulting from the low-reversed cyclic loading test show that all the test braces exhibited stable hysteretic behaviour for all displacement amplitudes, with a plump hysteresis curve and substantial energy absorption capability. It can be seen that there was no significant stiffness or strength degradation when the test completed, and the loading and unloading stiffnesses were basically the same. In addition, the force-displacement loops showed a distinct cyclic hardening characteristic and an asymmetrical feature between tension and compression. It must be pointed out that the BRB with a rigid connection produce a moment on the loading setup which should be considered in the structural design of the frame.

4.2. Skeleton Curve. The skeleton curves of the specimens are shown in Figure 8, in which the curves are almost identical. It is seen that the skeleton curves of three specimens present distinct bilinear characteristics, and there is an obvious inflexion between the elastic stage and the plastic stage. The core of each specimen has a noticeable strengthened segment after entering the plastic stage.

In order to concise the variation law of the skeleton curve of the CCA-BRB, the Ramberg–Osgood model [27] is used to fit the skeleton curves of the specimens. The formula of the Ramberg–Osgood model is given by

$$\frac{\Delta\varepsilon}{2} = \frac{\Delta\varepsilon_e}{2} + \frac{\Delta\varepsilon_p}{2} = \frac{\Delta\sigma}{2E} + \left(\frac{\Delta\sigma}{2K'}\right)^{1/n}, \quad (1)$$

where $\Delta\varepsilon$ represents total strain amplitude; $\Delta\varepsilon_e$ and $\Delta\varepsilon_p$ represent, respectively, elastic strain amplitude and plastic strain amplitude; $\Delta\sigma$ represents stress amplitude; K' and n represent, respectively, cyclic hardening coefficient and cyclic hardening exponent. The fitting parameters of the Ramberg–Osgood model are shown in Table 4.

Figure 9 plots the fitting skeleton curves. It is seen that the fitting curve was little different from that of test points curve, indicating that the Ramberg–Osgood model can be used to simulate the skeleton curve of CCA-BRB under cyclic loading.

4.3. Compression Strength Adjustment Factor. Due to the Poisson effect, the lateral cross section of the internal core tended to increase under compression; thus, the internal core may contact the external constraint member. Further, a frictional force at the contact surface was generated to increase the axial force of the core under the compression stage. In addition, the bearing capacity under compression is greater than that under tension, affecting the asymmetry characteristic of tension and compression of a brace.

The asymmetry between tension and compression of a brace is generally expressed by the compression strength adjustment factor β [28], which is defined by

$$\beta_i = \frac{N_{Ci,\max}}{N_{Ti,\max}}, \quad (2)$$

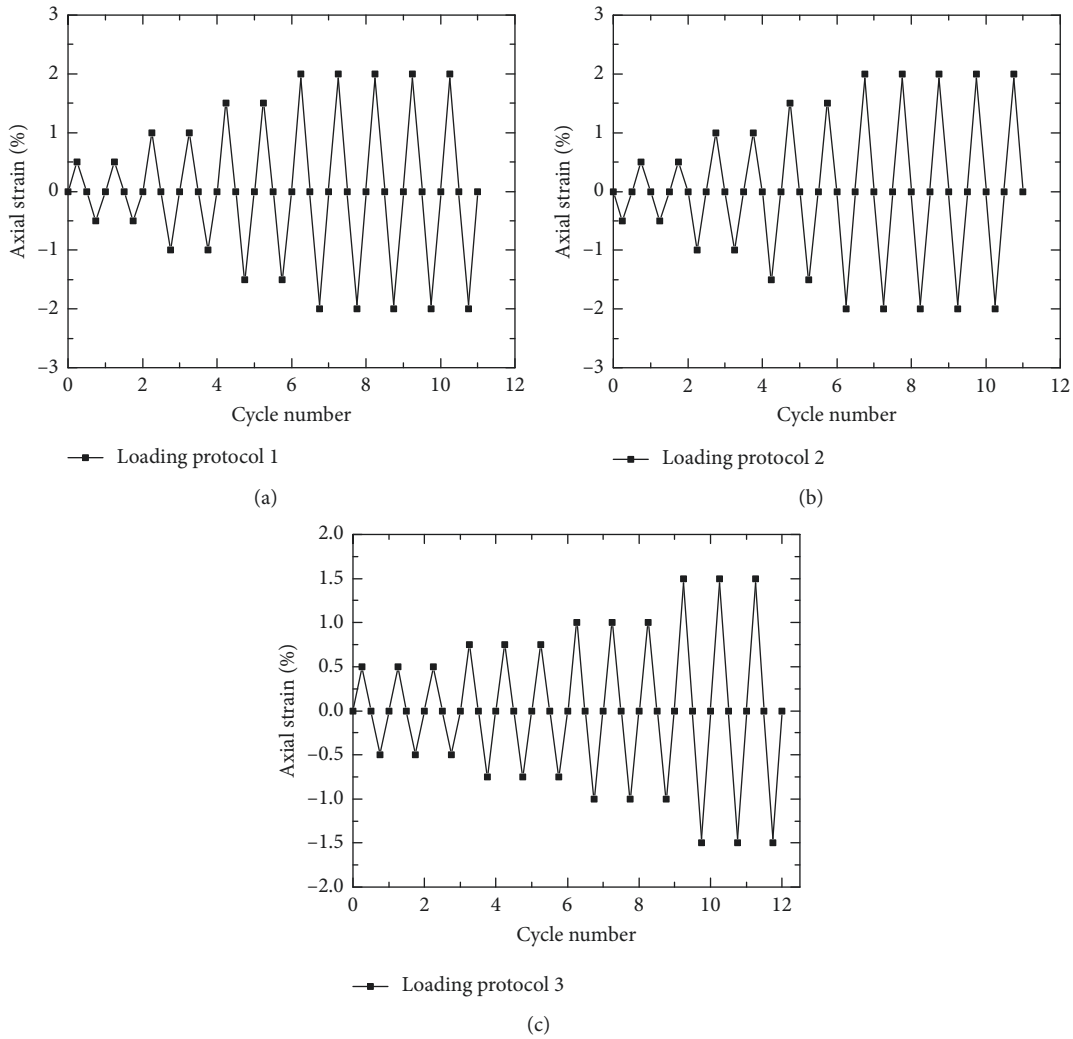

Figure 6: Loading protocols of the specimens.

Table 2: Axial displacement loading protocols of the specimens.

Specimen	Loading sequence	Axial strain (%)	Axial displacement (mm)	Bracing length ratio	Cycle number
BRB-1, BRB-2	1	±0.5	±4	1/300	2
	2	±1.0	±8	1/150	2
	3	±1.5	±12	1/100	2
	4	±2.0	±16	1/75	5
BRB-3	1	±0.5	±4	1/300	3
	2	±0.75	±6	1/200	3
	3	±1.0	±8	1/150	3
	4	±1.5	±12	1/100	3

Table 3: Material properties of steel.

Plate position	Steel type	Thickness (mm)	E (MPa)	f_y (MPa)	f_u (MPa)	f_y/f_u
Core member	Q235	8	2.01×10^5	265	425.6	0.62
External channel	Q235	5	2.03×10^5	270.7	430.4	0.63
External angle	Q235	5	2.03×10^5	270.1	433.8	0.62
Square end plate	Q235	25	2.05×10^5	256.8	415.2	0.62
Clamping plate	Q345	18	2.06×10^5	368.2	512.4	0.72

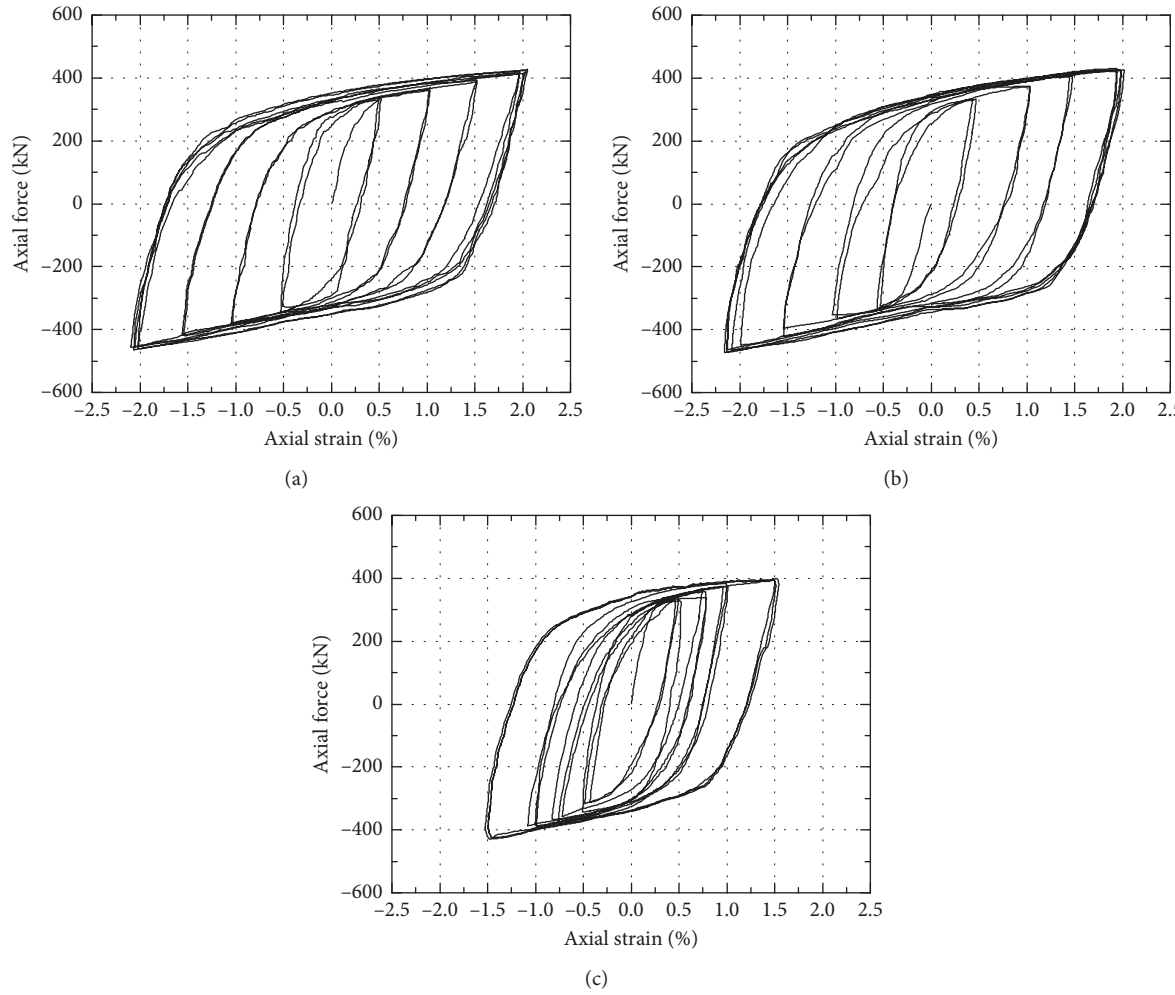

Figure 7: Hysteresis curves of the specimens. (a) BRB-1; (b) BRB-2; (c) BRB-3.

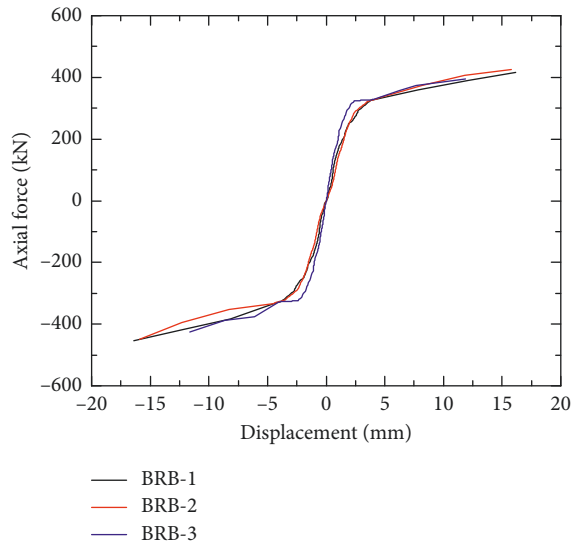

Figure 8: Skeleton curves of the specimens.

where $N_{Ci,max}$ and $N_{Ti,max}$ represent the maximum axial compression and the maximum axial tension, respectively, during the ith hysteresis loop.

Table 4: Fitting parameters.

Specimen	Fitting parameter	
	K' (MPa)	n
BRB-1	439.6	0.165
BRB-2	464.5	0.17
BRB-3	373.2	0.13

The values of compression strength adjustment factor during the distinct loading displacement amplitudes are shown in Table 5. Based on the requirements of ANSI/AISC 341-10, the compression strength adjustment factor of a BRB must not exceed 1.3. It can be seen that the increase factors of BRB-1 and BRB-2 were 1.092 and 1.118, respectively, which remained lower than the limit value 1.3 of the code under the loading amplitude of 2% core axial strain. The coefficient value of BRB-3 was 1.050 which is still below 1.3 when the core axial strain remained within 1.5%. The above-described indicated that the CCA-BRB still exhibited a stable and symmetrical hysteretic behaviour, with an adequate energy dissipation capacity even when the core axial strain reached 2%.

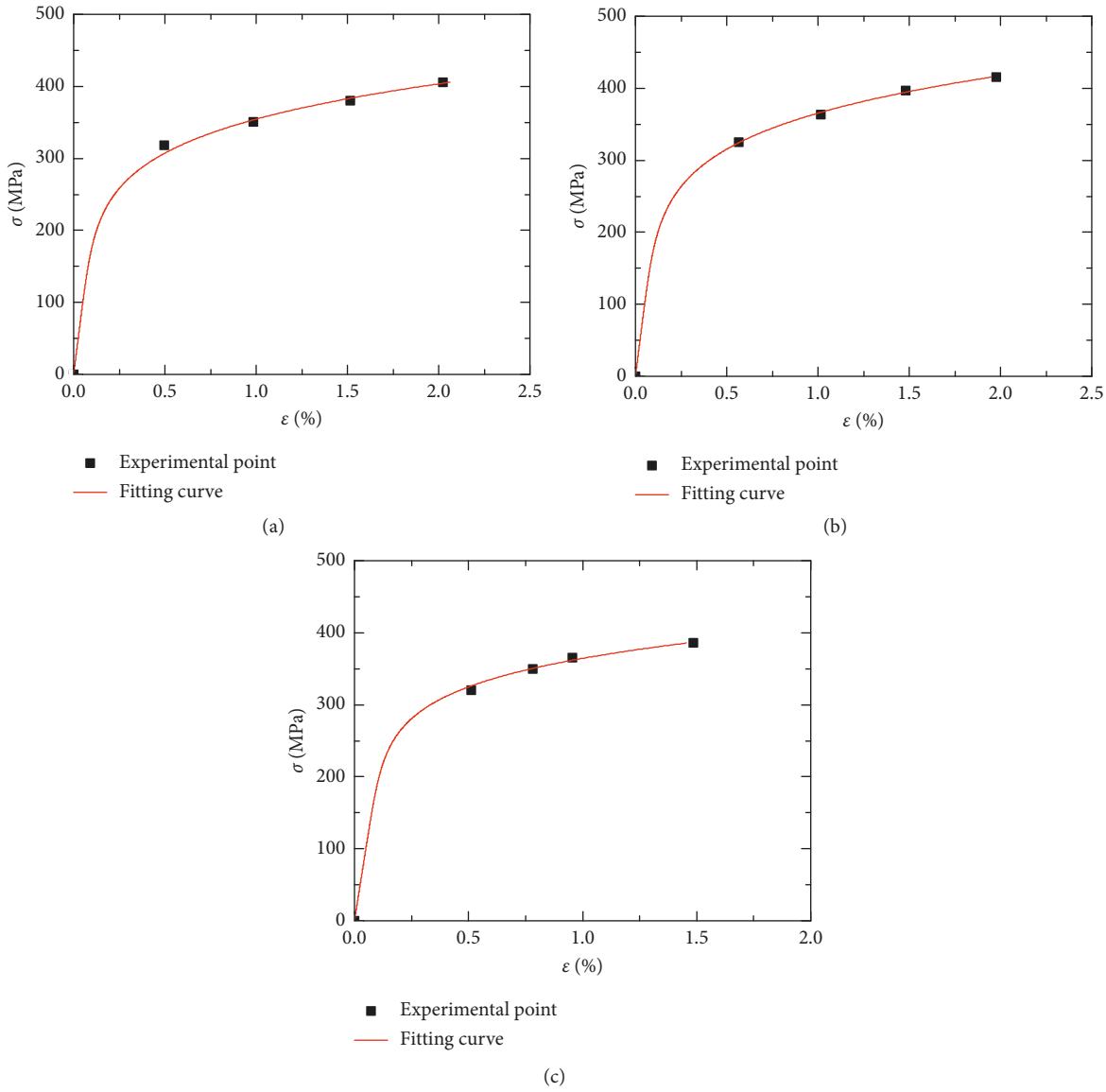

Figure 9: Fitting skeleton curves of the specimens. (a) BRB-1; (b) BRB-2; (c) BRB-3.

Table 5: Compression strength adjustment factor of the specimens.

Specimen	Compression strength adjustment factor under each core axial strain			
	0.5%	1%	1.5%	2%
BRB-1	1.024	1.043	1.079	1.092
BRB-2	1.012	0.979	1.038	1.118
BRB-3	0.5% 1.007	0.75% 1.037	1.0% 1.027	1.5% 1.050

4.4. Measured and Computed Stiffness Values. Based on the experimental data, the initial elastic stiffness and the secondary stiffness which are of interest in the mechanical characterization of the brace are identified in this section. As shown in Figure 3(c), the core of the brace with a cruciform cross section consists of a yielding portion, a transition portion, and a connection portion throughout, with the cross section of the yielding stage smaller than the cross sections of the transition portion and the connection portion. The total elastic stiffness of the brace is the summation in series of the individual stiffness of the segments described above. The formula for the total elastic stiffness of the core is given by

$$K^c_{\text{total}} = \frac{1}{\left(\left(1/K^c_{\text{y}}\right) + 2\left(1/K^c_{\text{tr}}\right) + 2\left(1/K^c_{\text{con}}\right)\right)}, \tag{3}$$

where K^c_{total} represents the total elastic stiffness, K^c_{y} represents the elastic stiffness of the yielding portion, K^c_{tr} represents the elastic stiffness of the transition portion, and K^c_{con} represents the elastic stiffness of the connection portion.

The values of computed elastic stiffness for the yielding portion, the transition portion, and the connection portion are, respectively,

$$K_{\mathrm{y}}^{c} = \frac{A_{\mathrm{y}}E}{L_{\mathrm{y}}} \approx \frac{1{,}024\,\mathrm{mm}^2 \times 201\,\mathrm{GPa}}{800\,\mathrm{mm}} = 275.3\,\mathrm{kN/mm}, \quad (4)$$

$$K_{\mathrm{tr}}^{c} = \frac{\left(A_{\mathrm{con}} - A_{\mathrm{y}}\right)E}{\left(\ln A_{\mathrm{con}} - \ln A_{\mathrm{y}}\right)L_{\mathrm{tr}}} \approx \frac{(1{,}984 - 1{,}024)\mathrm{mm}^2 \times 201\,\mathrm{GPa}}{(\ln 1{,}984 - \ln 1{,}024) \times 50\,\mathrm{mm}} = 5{,}829.6\,\mathrm{kN/mm}, \quad (5)$$

$$K_{\mathrm{con}}^{c} = \frac{A_{\mathrm{con}}E}{L_{\mathrm{con}}} \approx \frac{1{,}984\,\mathrm{mm}^2 \times 201\,\mathrm{GPa}}{150\,\mathrm{mm}} = 2{,}658.6\,\mathrm{kN/mm} \quad (6)$$

where A_{y} and A_{con} represent, respectively, the cross-sectional area of the yielding portion and the connection portion. Based on the above values given by equations (4)–(6), the total elastic stiffness K_{total}^{c}, given by equation (3), is 200.8 kN/mm.

Table 6 lists the computed stiffness, measured stiffness, and the difference between these values for each specimen. The computed elastic stiffness values given in columns 2, 3, 4, and 5 were obtained from equations (3)–(6), respectively. The measured stiffness values given in columns 6 and 7 were computed by fitting the tensile section of the skeleton curve (using a double broken line model) of each brace. Column 6, labelled K_{total}^{m}, corresponds to the slope of the axial force-displacement relationship measured for the elastic portion of the fitting skeleton curve, whereas, column 7, labelled K_2, corresponds to the slope measured for the plastic portion of the fitting skeleton curve.

As can be seen from Table 6, the computed total elastic stiffness value given by equation (3) is in close accordance with the value measured from the test data. In theory, the stiffness values used in the design should contain the entire portions of the brace. If the stiffness value for yielding portion be used in the design instead of the overall stiffness, then the stiffness value is overestimated by 37%. In addition, if assuming that the cross area over the entire length is equal to A_{y}, then the stiffness value is calculated to be 171.5 kN/mm and the stiffness value is still figured to be undervalued by 15%.

4.5. Secondary Stiffness. The secondary stiffness which usually can also be written as postyielding stiffness is of interest for the mechanical properties of the BRB and depends in general on the loading course. The measured values of secondary stiffness and postyielding ratio, $\alpha = K_2/K_{\mathrm{total}}^{m}$, of each specimen are given in columns 7 and 8 of Table 6, respectively. Column 8, labelled α, corresponds to the ratio of elastic stiffness to secondary stiffness.

4.6. Energy Dissipation Index. Energy dissipation capacity is an important index for evaluating the performance of CCA-BRB. In this section, the energy dissipation capacity of each specimen is evaluated via parameters which contain energy dissipation coefficient and equivalent viscous damping ratio. The parameters of the specimens were obtained from the hysteresis curves and are listed in Table 7. According to Section 4.5.6 of JGJ/T101-2015 [29], the values for the energy dissipation coefficient and the equivalent viscous damping ratio are calculated by, respectively,

$$\psi = \frac{S_{\mathrm{BEDFB}}}{\left(S_{\triangle\mathrm{OAB}} + S_{\triangle\mathrm{OCD}}\right)}, \qquad \zeta = \frac{S_{\mathrm{BEDFB}}}{2\pi\left(S_{\triangle\mathrm{OAB}} + S_{\triangle\mathrm{OCD}}\right)}, \quad (7)$$

where S_{BEDFB}, as shown in Figure 10, represents the hysteresis loop area of a brace enveloped by one displacement amplitude, $S_{\triangle\mathrm{OAB}}$ and $S_{\triangle\mathrm{OCD}}$ represent the area of triangle OAB and triangle OCD, respectively. It can be seen from Table 7 that the energy dissipation coefficient and the equivalent viscous damping ratio of each specimen show a trend of gradual increase with the increase of loading displacement amplitude. Further, the gradual increasing trend of energy dissipation indices indicates that the brace has a substantial and repeatable capability to absorb earthquake energy.

4.7. Ductility Coefficient. The deformation capacity which determines the maximum displacement of a brace is an important index for evaluating the seismic performance of CCA-BRB and is expressed via the ductility coefficient. The ductility coefficient of a brace refers to the ratio of the maximum displacement to the yield displacement of the brace before the obvious strength degradation of the hysteresis curve. The coefficients of each specimen are listed in Table 7. According to Section 4.5.4 of JGJ/T101-2015 [29], the formula is given by

$$\mu = \frac{d_{\mathrm{max}}}{d_{\mathrm{y}}}, \quad (8)$$

where d_{max} and d_{y} represent maximum displacement and yield displacement, respectively, of the brace. It can be seen from Table 7 that the ductility coefficient values of BRB-1 and BRB-2 appear to be 11.4 and 12.4, respectively, once the core axial strain reaches 2.0%, and the value of BRB-3 appears to be 7.4, once the core axial strain reaches 1.5%. In addition, the specimens have a large and substantial plastic deformation capability.

4.8. Cumulative Plastic Deformation Capability. An index used in practice to evaluate the plastic deformation capability of a brace is the cumulative plastic strain or, alternatively, the cumulative plastic deformation. The cumulative plastic deformation [30] of the brace can be defined by

$$\eta = \sum_{i=1}^{n}\left[\frac{2\left(\left|d_{\mathrm{max+}}\right|_i + \left|d_{\mathrm{max-}}\right|_i\right)}{d_{\mathrm{y}}} - 4\right], \quad (9)$$

where $|d_{\mathrm{max+}}|_i$ and $|d_{\mathrm{max-}}|_i$ represent the absolute values of the maximum tensile displacement and the maximum compressive displacement, respectively, during each visit i into the inelastic range. The last column of Table 7 lists the cumulative plastic deformation values of each specimen. It can be seen from Table 7 that the values of BRB-1 and BRB-2 appear to be 311 and 327, once the core loading

Table 6: Comparison of computed and measured stiffness values.

Specimen	Computed elastic stiffness (kN/mm)				Measured stiffness (kN/mm)			Difference
	K_y^c equation (4)	K_{tr}^c equation (5)	K_{con}^c equation (6)	K_{total}^c equation (3)	K_{total}^m	K_2	α	K_{total} (%)
BRB-1	275.3	5,829.6	2,658.6	200.8	199.86	8.15	0.041	−0.47
BRB-2	275.3	5,829.6	2,658.6	200.8	210.85	9.01	0.043	5
BRB-3	275.3	5,829.6	2,658.6	200.8	192.22	7.01	0.036	−4.27

Table 7: Ductility indices and energy dissipation indices of the specimens.

Specimen	Energy dissipation coefficient				Equivalent viscous damping ratio				Ductility coefficient	Cumulative plastic deformation
	0.5%	1.0%	1.5%	2.0%	0.5%	1.0%	1.5%	2.0%		
BRB-1	2.646	2.894	2.902	2.854	0.421	0.461	0.462	0.454	11.4	311.2
BRB-2	2.609	2.851	2.900	2.835	0.415	0.454	0.461	0.451	12.4	326.6
	0.5%	0.75%	1.0%	1.5%	0.5%	0.75%	1.0%	1.5%		
BRB-3	2.612	2.770	2.896	3.050	0.416	0.441	0.461	0.485	7.4	167.6

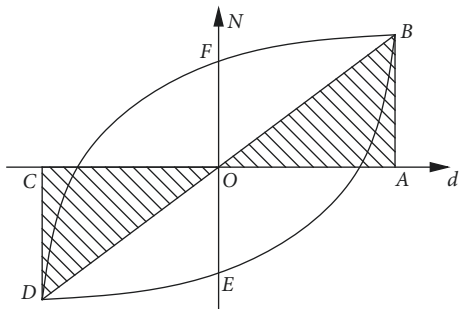

Figure 10: Calculation diagram of energy dissipation index.

displacement amplitude reaches the axial strain of 2.0%, and the value of BRB-3 appears to be 167.6, once the core loading displacement amplitude reaches the axial strain of 1.5%. Further, it is noted that the cumulative plastic deformation values of BRB-1 and BRB-2 during the testing protocol exceed the requirement of the minimum limit (200) set by the ANSI/AISC 341-10, indicating that the brace has an excellent plastic deformation capability.

5. Conclusions

In this study, low-reversed cyclic loading tests of three CCA-BRB specimens under three loading protocols were conducted to consider the seismic performance, hysteretic behaviour, and energy dissipation capability of CCA-BRBs. Based on the experimental results and several evaluation indices, the main conclusions drawn are the following:

(1) The observed hysteretic behaviour of the CCA-BRB with a rigid connection was excellent for all displacement amplitudes, indicating that the brace had a stable capability to absorb seismic energy.

(2) The skeleton curves of three CCA-BRB specimens present distinct bilinear characteristics. The Ramberg–Osgood model was adopted to approximate the skeleton curve of the brace, and two model parameters were found to fit the skeleton curves with little difference, indicating that the Ramberg–Osgood model can be used to simulate the skeleton curve of CCA-BRB under cyclic load.

(3) The computed initial elastic stiffness was in close agreement with the value measured from the test data, indicating that the stiffness used in the design should contain overall portions of the brace.

(4) All CCA-BRB specimens showed a stable energy absorption performance to enhance the resistance of existing and new structures during strong earthquake shaking.

Appendix

Derivation of Equation (5)

Schematic diagram of the derivation of equation (5) is shown in Figure 11. The elongation $d(\Delta l)$ of microsegment dx can be given by

$$d(\Delta l) = \frac{F\,dx}{EA(x)}, \tag{A.1}$$

where the cross-sectional area $A(x)$ can be given by

$$A(x) = A_{con} - \frac{A_{con} - A_y}{L_{tr}} x. \tag{A.2}$$

With integrating equation (A.1), the elongation of transition region can be obtained as

$$\begin{aligned} \Delta l &= \int_l \frac{F\,dx}{EA(x)} = \frac{F}{E}\int_l \frac{dx}{A_{con} - \left(A_{con} - A_y/L_{tr}\right)x} \\ &= \frac{F}{E} \times \frac{L_{tr}}{A_y - A_{con}} \ln\left(A_{con} - \frac{A_{con} - A_y}{L_{tr}} x\right)\Bigg|_0^{L_{tr}} \\ &= \frac{FL_{tr}}{E} \times \frac{\ln A_y - \ln A_{con}}{A_y - A_{con}}. \end{aligned} \tag{A.3}$$

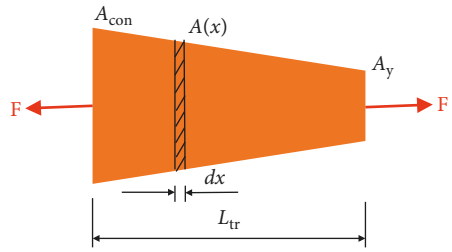

Figure 11: Schematic diagram of the derivation of equation (5).

With transforming equation (A.3), the stiffness of transition region can be given by

$$K_{tr}^{c} = \frac{F}{\Delta l} = \frac{\left(A_{con} - A_y\right)E}{\left(\ln A_{con} - \ln A_y\right)L_{tr}}. \quad (A.4)$$

Data Availability

All the data used to support the findings of this study are included within this article.

Conflicts of Interest

The authors declare that they have no conflicts of interest.

Acknowledgments

This work was supported by grants from the Fundamental Research Funds for the Central Universities (2018ZDPY04) and The Open Fund from Jiangsu Collaborative Innovation Center for Building Energy Saving and Construction Technology (SJXTQ1521).

References

[1] Y. Zhou, *Design and Application of Structures with Buckling-Restrained Brace*, China Building Industry Press, Beijing, China, 2007, in Chinese.

[2] C. J. Black, N. Makris, and I. D. Aiken, "Component testing, seismic evaluation and characterization of buckling-restrained braces," *Journal of Structural Engineering*, vol. 130, no. 6, pp. 880–894, 2004.

[3] Q. Xie, "State of the art of buckling-restrained braces in Asia," *Journal of Constructional Steel Research*, vol. 61, no. 6, pp. 727–748, 2005.

[4] R. Tremblay, P. Bolduc, R. Neville, and R. DeVall, "Seismic testing and performance of buckling-restrained bracing systems," *Canadian Journal of Civil Engineering*, vol. 33, no. 2, pp. 183–198, 2006.

[5] L. Di Sarno and G. Manfredi, "Experimental tests on full-scale RC unretrofitted frame and retrofitted with buckling-restrained braces," *Earthquake Engineering & Structural Dynamics*, vol. 41, no. 2, pp. 315–333, 2012.

[6] J. Zhang, B. Wu, Y. Mei, and P. B. Shing, "Experimental and analytical studies on a reinforced concrete frame retrofitted with buckling-restrained brace and steel caging," *Advances in Structural Engineering*, vol. 18, no. 2, pp. 155–171, 2015.

[7] S. Merrit, C.-M. Uang, and G. Benzoni, *Subassemblage Testing of Corebrace Buckling-Restrained Braces*, University of California, San Diego: La Jolla, CA, USA, 2003.

[8] C.-M. Uang and M. Nakashima, "Steel buckling-restrained braced frames," in *Earthquake Engineering from Engineering Seismology to Performance-Based Engineering*, Y. Bozorgina and V. V. Bertero, Eds., CRC Press, Boca Raton, FA, USA, 2004.

[9] K. Kimura, Y. Takeda, K. Yoshioka, N. Furuya, and Y. Takemoto, "An experimental study on braces encased in steel tube and mortar," in *Proceedings of the Annual Meeting of the Architectural Institute of Japan*, Tokyo, Japan, October 1976, in Japanese.

[10] A. Watanabe, Y. Hitomoi, E. Saeki, A. Wada, and M. Fujimoto, "Properties of braces encased in buckling-restraining concrete and steel tube," in *Proceedings of the 9th World Conference on Earthquake Engineering*, vol. 4, pp. 719–724, Tokyo-Kyoto, Japan, March 1988.

[11] C.-C. Chen, S.-Y. Chen, and J.-J. Liaw, "Application of low yield strength steel on controlled plastification ductile concentrically braced frames," *Canadian Journal of Civil Engineering*, vol. 28, no. 5, pp. 823–836, 2001.

[12] K. Inoue, S. Sawaizumi, and Y. Higashibata, "Stiffening requirements for unbonded braces encased in concrete panels," *Journal of Structural Engineering*, vol. 127, no. 6, pp. 712–719, 2001.

[13] M. Iwata and M. Murai, "Buckling-restrained brace using steel mortar planks; performance evaluation as a hysteretic damper," *Earthquake Engineering & Structural Dynamics*, vol. 35, no. 14, pp. 1807–1826, 2006.

[14] S. Kuwahara, M. Tada, T. Yoneyama et al., "A study on stiffening capacity of double-tube members," *Journal of Structural and Construction Engineering*, vol. 445, no. 3, pp. 151–158, 1993, in Japanese.

[15] M. E. Eryaşar and C. Topkaya, "An experimental study on steel-encased buckling-restrained brace hysteretic dampers," *Earthquake Engineering & Structural Dynamics*, vol. 39, no. 5, pp. 561–581, 2010.

[16] M. B. Bozkurt and C. Topkaya, "Development of welded overlap core steel encased buckling-restrained braces," *Journal of Constructional Steel Research*, vol. 127, pp. 151–164, 2016.

[17] M. Dehghani and R. Tremblay, "Design and full-scale experimental evaluation of a seismically endurant steel buckling-restrained brace system," *Earthquake Engineering & Structural Dynamics*, vol. 47, no. 1, pp. 105–129, 2018.

[18] K. Fukuda, T. Makino, and Y. Ichinohe, "Development of brace-type hysteretic dampers," Summaries of Technical Papers of Annual Meeting, Architectural Institute of Japan, vol. 8, pp. 867–868, 2004, in Japanese.

[19] H. Narihara, O. Tsujita, and Y. Koeteka, "The experimental study on buckling restrained braces (part 1 and part 2)," Summaries of Technical Papers of Annual Meeting, Architectural Institute of Japan, vol. 9, pp. 911–914, 2000, in Japanese.

[20] J. Zhao, B. Wu, and J. Ou, "A novel type of angle steel buckling-restrained brace: cyclic behavior and failure mechanism," *Earthquake Engineering & Structural Dynamics*, vol. 40, no. 10, pp. 1083–1102, 2011.

[21] J. Zhao, B. Wu, and J. Ou, "Effect of brace end rotation on the global buckling behavior of pin-connected buckling-restrained braces with end collars," *Engineering Structures*, vol. 40, no. 7, pp. 240–253, 2012.

[22] H. Guerrero, J. A. Escobar, and A. Teran-Gilmore, "Experimental damping on frame structures equipped with buckling-restrained braces (BRBs) working within their linear-elastic response," *Soil Dynamics and Earthquake Engineering*, vol. 106, pp. 196–203, 2018.

[23] H. Guerrero, T. Ji, J. A. Escobar, and A. Teran-Gilmore, "Effects of buckling-restrained braces on reinforced concrete precast models subjected to shaking table excitation," *Engineering Structures*, vol. 163, pp. 294–310, 2018.

[24] Standardization Administration of the People's Republic of China (SAC), "Code for seismic design of buildings," GB50011-2010, SAC, Beijing, China, 2010, in Chinese.

[25] American Institute of Steel Construction (AISC), "Seismic provisions of structural steel buildings," ANSI/AISC341-10, AISC, Chicago, IL, USA, 2010.

[26] Standardization Administration of the People's Republic of China (SAC), "Metallic materials—tensile testing—part 1: method of test at room temperature," GB/T228.1-2010, SAC, Beijing, China, 2010, in Chinese.

[27] W. Ramberg and W. R. Osgood, "Description of stress-strain curves by three parameters," Technical Notes No. 90E2, National Advisory Committee for Aeronautics, Washington, DC, USA, 1943.

[28] Z.-q. Jiang, Y.-l. Guo, A.-l. Zhang, C. Dou, and C.-x. Zhang, "Experimental study of the pinned double rectangular tube assembled buckling-restrained brace," *Journal of Zhejiang University-Science A*, vol. 18, no. 1, pp. 20–32, 2017.

[29] Standardization Administration of the People's Republic of China (SAC), "Specification for seismic tests of buildings," JGJ/T101-2015, SAC, Beijing, China, 2015, in Chinese.

[30] J. X. Zhao, *Seismic behavior and stability design methods of all-steel buckling-restrained braces*, Ph.D. thesis, Harbin Institute of Technology, Harbin, China, 2012.